Tidal Disruption of a Star By a Massive Black Hole Computed In Fermi Normal Coordinates

Roseanne M. Cheng

A dissertation submitted to the faculty of the University of North Carolina at Chapel Hill in partial fulfillment of the requirements for the degree of Doctor of Philosophy in the Department of Physics and Astronomy.

Chapel Hill
2012

Approved by:

Charles R. Evans

Y. Jack Ng

John Blondin

Jon Engel

Chris Clemens

Fabian Heitsch

Abstract

ROSEANNE M. CHENG: Tidal Disruption of a Star By a Massive Black Hole Computed In Fermi Normal Coordinates.
(Under the direction of Charles R. Evans.)

We present a new numerical code constructed to obtain accurate simulations of encounters between a star and a massive black hole. We assume Newtonian hydrodynamics and self-gravity for the star. The three-dimensional parallel code includes a PPMLR hydrodynamics module to treat the gas dynamics and a Fourier transform-based method to calculate the self-gravity. The formalism for calculating the relativistic tidal interaction in *Fermi normal coordinates* (FNC) allows the addition of an arbitrary number of terms in the tidal expansion. We present the relevant post-Newtonian terms for this code. Results are given for an $n = 1.5$ polytrope with comparisons between simulations and predictions from the linear theory of tidal encounters. It is shown that the inclusion of the $l = 3$ tidal term will cause the center of mass of the star to deviate from the origin of the FNC. We consider relativistic encounters for three different mass ratios, $\mu = 1.28 \times 10^{-3}, 4.21 \times 10^{-4}, 3.77 \times 10^{-5}$. We show a relativistic suppression in the amount of energy deposited onto the star. We find that the dimensionless function $T_2(\eta)$ (which characterizes the energy deposited into non-radial oscillations) must not only be a function of the dimensionless disruption parameter, η, but also of a dimensionless relativistic parameter Φ_p. We speculate on the source of the observed energy excess in the tidal encounter simulations from the linear theory. We find that the energy deposited into radial oscillations is negligible and that the shock heating in the outer layers of the post-encounter star contributes a significant amount. We estimate the new orbital parameters of the star after it passes by the black hole.

"Gin a body meet a body

Flyin' through the air.

Gin a body hit a body,

Will it fly? And where?

Ilka impact has its measure,

Ne'er a ane hae I,

Yet a' the lads they measure me,

Or, at least, they try.

Gin a body meet a body

Altogether free,

How they travel afterwards

We do not always see.

Ilka problem has its method

By analytics high;

For me, I ken na ane o' them,

But what the waur am I?"

–James Clerk Maxwell, "Rigid Body Sings"

Acknowledgments

This research was supported by the US Department of Education GAANN fellowship number P200A090135, NC Space Grant's Graduate Research Assistantship Program, and the UNC–Chapel Hill Graduate School Dissertation Completion Fellowship.

I would like to thank the members of the thesis committee for taking the time to review my work. I would like to thank Jack Ng for all of the encouragement during the postdoctoral application season. I would like to thank John Blondin for helping me figure out Virginia Hydrodynamics-1. I would especially like to thank Chuck Evans for this research problem and supporting my endeavor.

Table of Contents

List of Figures

List of Tables

List of Abbreviations and Symbols

$\alpha, \beta, \gamma, \ldots$	Schwarzschild coordinates indices running from 0 to 3
$i, j, k, \ldots$	Spatial coordinates indices running from 1 to 3
$(a), (b), (c), \ldots$	Schwarzschild standard tetrad coordinates
$a, b, c, \ldots$	Fermi normal coordinates
M_*	Mass of the star
R_*	Radius of the star
M	Mass of the black hole
R_p	Periastron distance from black hole
μ	Mass ratio M_*/M
η	Disruption parameter
ν	Radius of the star to periastron distance ratio R_*/R_p
$\eta_{\mu\nu}$	Minkowski metric
$g_{\mu'\nu'}$	Schwarzschild coordinate metric
g_{ab}	Fermi normal coordinate metric
$R_{\mu'\alpha'\nu'\beta'}$	Riemann tensor in Schwarzschild coordinates
$R_{(a)(b)(c)(d)}$	Riemann tensor in Schwarzschild standard tetrad
R_{abcd}	Riemann tensor in Fermi normal coordinates
$\Gamma^{\alpha'}{}_{\beta'\gamma'}$	Connection coefficients in Schwarzschild coordinates
∂_μ or $_{,\mu}$	Partial derivative

Chapter 1

Introduction

Lurking in most large galaxies are supermassive black holes. They reside in active and dormant galaxies and their presence is revealed only through the interaction with their surroundings. The best diagnostic for the presence of a black hole in a nonactive galaxy would be the tidal disruption of stars [1, 2]. There are many observable signatures associated with this process. When a star disrupts near a black hole, some of the debris is ejected from the system and the rest that is bound eventually accretes onto the black hole. The fate of the debris is dependent on the type of star and the mass and spin of the black hole. If the star is known, then a study of its tidal disruption will provide an independent means of measuring the mass of the black hole from the $M-\sigma$ relation, the empirical correlation between the stellar velocity dispersion σ of a galaxy bulge and the black hole mass M at the center. From dynamical models of main-sequence stars, it is predicted that tidal disruptions will occur once every 10^3-10^5 years for a non-spinning black hole of mass $M \lesssim 10^8 M_\odot$ [3, 4]. A more massive black hole would result in a capture orbit instead of tidal disruption. For maximally spinning black holes, the upper limit on the mass of the black hole may be increased [5]. This suggests that solar-type star tidal disruption rates are dependent on black hole spin for $M \geq 10^8 M_\odot$. In this thesis, we are concerned with the tidal disruption of white dwarfs through close encounters with a massive black hole.

By simulating the tidal disruption mechanism with a computer, we are able to provide theoretical models to match observation of tidal disruption candidates. A flare of optical, UV, and X-ray emission will occur promptly upon disruption and as captured gas streams back to the black hole after one final orbit [1]. X-ray observatories Chandra and XMM-Newton observed the first tidal disruption event candidates [2, 6]. Since then, obervations made in the optical, ultraviolet, and X-ray reveal many more available for study [7, 8, 9, 10, 11, 12]. Recently, the unusual detection of long duration γ-ray bursts for Swift J164449.3+573451 suggest that more tidal disruption candidates associated with jet production are possible [13, 14, 15]. It is also of interest to use simulations to explain other possible observational signatures such as the supernova-like remnant structures associated with the ejection of debris [16, 17], the electromagnetic signal coupled with a gravitational wave event [18], and the thermonuclear runaway from the shock heating associated with severe compression [19, 20, 21].

The importance of including relativistic tidal effects in a computer simulation may be highlighted by the recent unusual observations of Swift J1644+57. The Swift satellite detected a long duration γ-ray burst and intense X-ray flares for several days followed by flares with significant decay [14]. A precurser X-ray flare was also associated with these events. Typical GRBs reach similar luminosity, but generally fall-off more rapidly. The detected X-ray luminosity ranged from $10^{45} - 4 \times 10^{48}$ erg s^{-1}, which suggests the release of gravitational energy by accretion of matter onto a black hole. From the X-ray variability time-scale of the object, $\delta t_{obs} \sim 100$ s, Burrows et al. [14] set the limit on the black hole mass to be $10^6 - 2 \times 10^7 M_\odot$. The presence of a radio transient also suggests a jet hitting surrounding gas. The properties of this event are different from the standard tidal disruption events and AGN jets. Bloom et al. [13] note that the two peaks in the broadband spectral energy distribution represent synchrotron and inverse Compton processes, similar to what is expected for blazars [13]. They propose that Swift J1644+57 is a small-scale blazar fed by the disruption of a solar-type star by a $10^6 - 10^7 M_\odot$ black hole. Krolik and Piran propose a different scenerio –a white dwarf is disrupted by a $\lesssim 10^5 M_\odot$ intermediate mass black hole upon several successive encounters [22]. A white dwarf has a greater density than a solar-type star and its presence may account for the short timescales in the event. The series of flares are perhaps explained by the return of gas that is stripped off of the white dwarf as it makes several encounters before disruption. Krolik and Piran state that if this scenerio is correct then this event is the first indication of a black hole of mass $10^4 - 10^5 M_\odot$. In this thesis, we show that modeling the disruption between a star and a black hole with mass smaller than $10^6 M_\odot$ requires the inclusion of relativistic terms in the tidal interaction.

There are several interesting aspects of white dwarf – intermediate mass black hole encounters. For mass ratios $\sim 10^{-6}$ and smaller, the Roche tidal radius is smaller than the Schwarzschild radius and the white dwarf will be on a capture orbit. Therefore, in studying the tidal interaction, the lower limit in mass ratio is $\sim 10^{-6}$. For non-disruptive encounters, the normal modes of the white dwarf can be excited non-resonantly and several successive encounters may lead to additional mode excitation and heating. In the regime where gravitational radiation is the dominant mechanism for the evolution of the orbit, resonant passages may excite modes [23, 20]. Significant energy transfer may lead to an increase in temperature such that a thermonuclear runaway produces a Type Ia supernova.

Several theoretical treatments to the problem of uncovering the cause of extremely luminous sources at the centers of galaxies indicate that the debris from a tidally disrupted star is the culprit. In the absence of hydrodynamic forces, the amount of debris bound to the black hole depends on the change in the gravitational potential across the star [24, 1]. However, the nature of this problem suggests that a full three-dimensional hydrodynamic treatment is necessary to determine the fate of the disrupted star. Semi-analytic studies of the tidal interaction between close binaries provide important details on the energy transfer during this process [25, 26, 27, 28]. Several numerical methods have been used to model the disrupted star as it passes by the black hole on a parabolic orbit. Several studies have implemented the affine model and results indicate that for orbits with periastron much smaller the Roche tidal radius, the star will undergo severe compression and "pancake" upon disruption [29]. Such encounters are interesting because of the possibility of triggering a thermonuclear explosion. However, the main limitation of the affine model is that the star can only be approximated as an ellipsoid. Using smooth particle hydrodynamics for tidal disruption adds flexibility to solving the problem in that no approximations to the shape of the star are needed and the full process is treated in a gridless manner [30]. This method is particularly useful in modeling the fall-back of debris after a first encounter. Many works use Newtonian and relativistic versions of the method [31, 32, 33, 34, 18, 35, 21]. The results of SPH methods are questionable because of the production of spurious entropy in adding artificial viscosity to treat shock waves [36]. There are a few comparisons of the SPH pancake mechanism simulations with one-dimensional finite difference methods (focusing on the compression orthogonal to the orbital plane) [18, 37]. Studies using three-dimensional simulations with high-resolution shock-capturing techniques model the disruption in a coordinate system centered on the star. Newtonian hydrodynamics and self-gravity is assumed for the star and a Newtonian quadrupole tide is used [38, 39, 40, 41]. A few studies have implemented the effects of the black hole space-time [42, 43] and it is of interest to follow-up these studies with higher resolution and a higher-order relativistic treatment to the black hole tidal interaction. Recently, general relativistic hydrodynamic methods with adaptive mesh refinement [44] and additionally with magnetohydrodynamics [45] have been applied to the disruption problem. These methods are well-suited to modeling the accretion flare.

The purpose of this work is to study the disruption phase of the encounter, focusing on energy and angular momentum deposition. We would like to be able to use these results as initial conditions in subsequent computations of the fate of the post-disruption debris. In this thesis, we are interested in the tidal disruption of white dwarfs by intermediate mass Schwarzschild black holes. In Chapter 2, we begin by presenting the physics of tidal disruption in the Newtonian limit. We list the different phases the star undergoes as it makes a close passage by the black hole. We introduce the linear theory of tidal interactions. In Chapter 3, the relativistic treatment of the tidal interaction between the white dwarf and the black hole is presented. We introduce the coordinate system for our calculations, the Fermi normal coordinates (FNC). We use Newtonian hydrodynamics and self-gravity for the star and set a cut-off in the combined self-gravity and tidal gravity metric expansion at stellar 1-PN. This restricts the number of terms we may use for our calculation of the tidal acceleration. Using a post-Newtonian formalism, we justify our use of retained terms in the expansion. In Chapter 4, we present the numerical method for simulating tidal disruption. We use the piecewise parabolic method with Lagrangian remap (PPMLR) for the hydrodynamics solver. We use a pseudo-spectral method to solve Poisson's equation. We calculate the relativistic tidal acceleration using a routine to update the location of the FNC frame along the geodesic using the hydrodynamic time as the proper time. Finally, we give the results of our numerical method in Chapter 5. We consider encounters at the threshold of disruption and weaker. We choose intermediate mass black holes to be $M \sim 10^3 M_\odot, 10^4 M_\odot, 10^5 M_\odot$. We first present a validation of the numerical method using a stellar equilibrium model. For our simulations with the tidal interaction, we use the relativistic quadrupole and octupole terms. We note that the inclusion of the octupole term drives the center of mass of the star off of the origin of the FNC frame. We compare the results for non-disruptive encounters with the predictions from the linear theory. We give the amount of energy and spin-angular momentum deposited onto the star and note a difference in the energy between Newtonian and relativistic encounters. We summarize our work and present extensions in Chapter 6.

Chapter 2

Physics of Tidal Disruption From the Newtonian Viewpoint

In this chapter we consider the tidal disruption of a star by a black hole in the Newtonian limit. We begin by introducing general assumptions about the process and introduce the dimensionless disruption parameter η, which characterizes the types of encounters in terms of the mass of the star, the large central mass (black hole), the radius of the star, and the distance of closest approach. Then, we consider physical effects that may occur when a star passes too close to a massive black hole. For the most part the star is assumed to be a polytrope, which allows its envelope structure to be described by a single parameter n and serves as an approximation for a variety of objects (e.g., solar-type stars, white dwarfs, red giants, and neutron stars). In the second section, we discuss the assumption of a polytropic equation of state and review solutions of the resulting equations of stellar equilibrium. In the third section, we consider the consequences of a polytropic star in a Newtonian tidal field. We find that the octupole tidal field causes the center of mass of an extended object like a star to accelerate relative to the trajectory of a point mass. We discuss torques on the fluid configuration. In the fourth section, we consider weak encounters where the star does not disrupt, but may become (linearly) distorted. In this limit, we apply the linear theory of tidal interactions and consider the amount of predicted total energy and (spin) angular momentum deposited onto the star during the encounter. In the final section, we discuss disruptive encounters and the nature of the resulting debris.

2.1 Overview of the process of tidal disruption

In the following, we describe how a star disrupts during an encounter with a heavy point mass (black hole). In this chapter, we will refer to the central mass as a "black hole," even though we consider only Newtonian physics. We assume that far away from the black hole the star is in spherical hydrostatic equilibrium, such that only the pressure forces and self-gravity of the gas are in balance. If we consider encounters at the threshold of disruption, then roughly we can say that at periastron the differential tidal acceleration across the star is comparable to or larger than its self-gravity acceleration. It can also be said that tidal disruption occurs when the orbital timescale of the star is less than or equal to the stellar pulsational timescale. Given these assumptions, an encounter may be described by a dimensionless parameter η, the disruption parameter, such that

$$\eta = \left(\frac{R_p^3}{M} \frac{M_*}{R_*^3} \right)^{1/2}, \tag{2.1.1}$$

where M_*, R_*, M, and R_p are the mass of the star, radius of the star, mass of the black hole, and radius of periastron, respectively [26]. Tidal disruption occurs for $\eta \lesssim 1$. For $\eta > 1$, the star does not disrupt completely, though it may be partially stripped. We may define the tidal radius for $\eta = 1$ where $R_T = R_*(M/M_*)^{1/3}$. We may also characterize these encounters with a penetration factor $\beta = R_T/R_p = \eta^{-2/3}$ [19].

A fraction of gas from a star that has been disrupted or partially disrupted will return to periastron after a last orbit and then presumably settle into an accretion disk about the black hole. The nature of this gaseous debris depends on the stellar structure of the star and on the detailed hydrodynamic forces and residual self-gravity as the debris expands. After disruption, nearly Keplerian motion will cause the gas to spread within the orbital plane and compressional bounce and envelope shocks cause some gas to rise out of the orbital plane. Escaping gas cools and loses all significant self-gravity, effectively freezing into a distribution of Keplerian orbits. Eventually hydrodynamic forces become important again as inclined orbits intersect near apastron and as the stream returns to periastron. For very close encounters, gas from the star may accrete onto the black hole immediately. The tidal disruption process may described in phases: disruption (with possible prompt accretion), sheared motion of debris, accretion upon return to pericenter, and possible repetitions of debris orbits and accretion. The focus of this thesis is on the disruption phase, although the results of the analysis are important for modeling the rest of the process.

2.2 Polytropes

In this section, we discuss the assumption that the star can be modeled effectively as a polytrope. Using thermodynamic considerations, we derive expressions to quantify the thermodynamic description of the star. This is important later for the computational diagnostics of the simulations. We show how to obtain density and pressure profiles of a star in terms of its polytropic index n using the Lane-Emden equation [46].

2.2.1 Thermodynamic considerations

Consider a system in terms of pressure p, volume V, internal energy U, heat flux Q, entropy S, and temperature $\mathcal{T}$. Assume that it is hydrostatic, in equilibrium, and undergoes processes that are reversible and adiabatic. Then, the heat flux is quasi-static and the entropy is constant [46, 47]. The first and second laws of thermodynamics are given by

$$dU = đQ - pdV, \qquad đQ = \mathcal{T}dS = 0. \tag{2.2.1}$$

For a perfect (ideal) gas, the equation of state is given by

$$pV = R\mathcal{T}, \qquad U = U(\mathcal{T}), \tag{2.2.2}$$

with gas constant $R = 8.314 \times 10^7$ erg/deg mol and one assumes that the internal energy is a function of temperature only. The heat capacity at constant volume is $C_v = (\partial U/\partial \mathcal{T})_v = dU/d\mathcal{T}$ and at constant pressure is $C_p = (đQ/d\mathcal{T})_p = C_v + R$. Define the ratio of specific heats to be $\gamma = C_p/C_v = 1 + R/C_v$. For monoatomic gases, $\gamma = 5/3$, and for diatomic gases, $\gamma = 7/5$. The internal energy may be written as $U = C_v\mathcal{T} = R\mathcal{T}/(\gamma - 1)$. Then, we can rewrite the equation of state for an ideal gas as

$$pV = R\mathcal{T} = (\gamma - 1)U, \qquad p = (\gamma - 1)\rho\varepsilon, \tag{2.2.3}$$

in terms of the internal energy U or the specific internal energy $\varepsilon = U/M$, where M is the molar mass and ρ is the density.

Substituting the ideal gas equation of state into the combination of the first and second laws in terms of specific quantities (heat per molar mass $q = Q/M$, specific volume $\tau = V/M$, specific entropy $s = S/M$), we obtain

$$đq = 0 = d\varepsilon + pd\tau = \tau dP + \gamma\frac{p}{\rho^2}d\rho \qquad \text{or} \qquad dp = \gamma\frac{p}{\rho}d\rho \tag{2.2.4}$$

and find that

$$\left(\frac{\partial p}{\partial \rho}\right)_s = \gamma\frac{p}{\rho}. \tag{2.2.5}$$

An expression for the speed of sound in a perfect gas is given by the following [48]. If we assume small changes in the density and pressure and flow velocities smaller than the sound speed, then we may derive an acoustic equation describing the propagation of sound waves using the conservation of mass and momentum equation. Consider the small changes in the density and pressure to be written as $\rho = \rho_0 + \Delta\rho$ and $p = p_0 + \Delta p$. Then, the linearized conservation of mass equation may be written as

$$\frac{\partial \rho}{\partial t} = -\rho\frac{\partial v}{\partial x} \longrightarrow \frac{\partial}{\partial t}(\Delta\rho) = -\rho_0\frac{\partial v}{\partial x}. \tag{2.2.6}$$

The linearized conservation of momentum equation may be written as

$$\rho\frac{\partial v}{\partial t} = -\frac{\partial p}{\partial x} = -\left(\frac{\partial p}{\partial \rho}\right)_s\left(\frac{\partial \rho}{\partial x}\right) \longrightarrow \rho_0\frac{\partial v}{\partial t} = -\left(\frac{\partial p}{\partial \rho}\right)_s\frac{\partial}{\partial x}(\Delta\rho) = -c^2\frac{\partial}{\partial x}(\Delta\rho), \tag{2.2.7}$$

where we assume isentropic particle motion in the sound wave, $\Delta p = (\partial p/\partial\rho)_s\Delta\rho$, and $c^2 = (\partial p/\partial\rho)_s$. Taking the partial time derivative of (2.2.6),

$$\frac{\partial^2}{\partial t^2}(\Delta\rho) = -\rho_0\frac{\partial^2 v}{\partial t\partial x}, \tag{2.2.8}$$

taking the partial time derivative of (2.2.7),

$$\rho_0\frac{\partial^2}{\partial x\partial t}v = -c^2\frac{\partial^2\rho}{\partial x^2}, \tag{2.2.9}$$

and combining the two results we obtain a wave equation,

$$\left(\frac{\partial^2}{\partial t^2} - c^2\frac{\partial^2}{\partial x^2}\right)\Delta\rho = 0. \tag{2.2.10}$$

The solutions are

$$\Delta\rho = \Delta\rho(x \pm ct), \tag{2.2.11}$$

where the disturbance propagates in the $\pm x$ direction with speed c of sound,

$$c^2 = \left(\frac{\partial p}{\partial \rho}\right)_s = \frac{\gamma p}{\rho} = \gamma R\mathcal{T}. \tag{2.2.12}$$

Re-writing $dp = (\gamma p/\rho)d\rho$ as $[\partial(\ln p)/\partial(\ln\rho)]_s = \gamma$ and integrating, and taking γ and s constant, we obtain the polytropic equation of state,

$$p = \kappa(s)\rho^\gamma, \tag{2.2.13}$$

for some κ that is a function of the specific entropy, s, which must be at least constant (adiabatic) along stream lines in the fluid. For an isentropic gas ($s =$ constant everywhere), we have $p = \kappa\rho^{\gamma}$, with a universal constant κ.

2.2.2 Completely degenerate, ideal Fermi gas equation of state

In this thesis we will be primarily interested in examining tidal encounters of white dwarfs. For an isolated white dwarf at $\mathcal{T} = 0$, it is degeneracy pressure that supports the star against gravitational collapse. Assume the pressure is just due to electrons which may be described by a cold, degenerate equation of state [47]. We define the Fermi momentum of the electron in terms of its Fermi energy E_F, the speed of light c, and the mass of the electron m_e as $E_F = (p_F^2 c^2 + m_e^2 c^4)^{1/2}$. We further define a dimensionless Fermi momentum as $x = p_f/(m_e c)$. The pressure of the gas is given by [47]

$$\begin{aligned} p_e &= \frac{m_e c^2}{\lambda_e^3}\phi(x) = 1.42180 \times 10^{25}\phi(x) \text{ dyne cm}^{-2}, \\ \phi(x) &= \tfrac{1}{8\pi^2}\left\{x(1+x^2)^{1/2}(2x^2/3-1) + \ln\left[x + (1+x^2)^{1/2}\right]\right\}, \end{aligned} \tag{2.2.14}$$

and the total energy density is given by

$$\begin{aligned} \varepsilon_e &= \frac{m_e c^2}{\lambda_e^3}\chi(x), \\ \chi(x) &= \tfrac{1}{8\pi}\left\{x(1+x^2)^{1/2}(1+2x^2) - \ln\left[x + \left(1+x^2\right)^{1/2}\right]\right\}, \end{aligned} \tag{2.2.15}$$

where $\lambda_e = \hbar/(m_e c)$ is the Compton wavelength of the electron. Consider the non-relativistic and relativistic limits of the equation of state in terms of the dimensionless Fermi momentum. For non-relativistic electrons, $x \ll 1$, we have that

$$\begin{aligned} \phi(x) &\rightarrow \tfrac{1}{15\pi^2}\left(x^5 - \tfrac{5}{14}x^7 + \tfrac{5}{24}x^9 \cdots\right), \\ \chi(x) &\rightarrow \tfrac{1}{3\pi^2}\left(x^3 + \tfrac{3}{10}x^5 - \tfrac{3}{56}x^7 \cdots\right). \end{aligned} \tag{2.2.16}$$

For relativistic electrons, $x \gg 1$, we have that

$$\begin{aligned} \phi(x) &\rightarrow \tfrac{1}{12\pi^2}\left(x^4 - x^2 + \tfrac{3}{2}\ln 2x \cdots\right), \\ \chi(x) &\rightarrow \tfrac{1}{4\pi^2}\left(x^4 + x^2 - \tfrac{1}{2}\ln 2x \cdots\right). \end{aligned} \tag{2.2.17}$$

For the two limiting cases, the equation of state has a polytropic form, $p = \kappa\rho^\gamma$, with (1) non-relativistic electrons: $\rho \ll 10^6$g cm^{-3}, $x \ll 1$, $\phi(x) \to x^5/15\pi^2$,

$$\kappa = \frac{3^{2/3}\pi^{4/3}}{5}\frac{\hbar^2}{m_e m_u^{5/3}\mu_e^{5/3}} = \frac{1.0036\times 10^{13}}{\mu_e^{5/3}}, \qquad \gamma = \tfrac{5}{3}, \tag{2.2.18}$$

and (2) extremely relativistic electrons: $\rho \gg 10^6$g cm^{-3}, $x \gg 1$, $\phi(x) \to x^4/12\pi^2$,

$$\kappa = \frac{3^{1/3}\pi^{2/3}}{4}\frac{\hbar c}{m_u^{4/3}\mu_e^{4/3}} = \frac{1.2435\times 10^{15}}{\mu_e^{4/3}}, \qquad \gamma = \tfrac{4}{3}, \tag{2.2.19}$$

where the numerical values are in cgs units and for atomic mass unit $m_u = 1.66057\times 10^{-24}$g and mean molecular weight per electron μ_e. Thus, in the limit of extreme non-relativistic and ultra-relativistic electrons, the ideal Fermi gas equation of state reduces to a polytropic form.

2.2.3 Stellar equilibrium

Consider the equations of hydrostatic equilibrium for a spherically symmetric, non-relativistic star [47, 46] of mass M_* and radius R_*. The mass interior to a radius r is given by

$$m(r) = \int_0^r \rho\, 4\pi r^2 dr, \qquad \frac{dm(r)}{dr} = 4\pi r^2\rho. \tag{2.2.20}$$

Consider a fluid element between r and $r+dr$ with an area dA perpendicular to the radial direction. The gravitational force exerted on the element dm due to the mass interior to r is equal to the net outward pressure force on dm. Then, the equilibrium condition is

$$\frac{dp}{dr} = -\frac{Gm(r)\rho}{r^2}. \tag{2.2.21}$$

Consider the following quantities to obtain a virial theorem for the star. The gravitational potential energy is given by

$$\Omega = -\int_0^M \frac{Gm(r)dm(r)}{r} = \int_0^R \frac{dp}{dr}4\pi r^3 dr = -3\int_0^R p4\pi r^2 dr, \tag{2.2.22}$$

where the pressure p at the surface of the star is zero. The internal energy is $U = \int_0^R \rho\epsilon 4\pi r^2 dr = \int_0^R [p/(\gamma-1)]4\pi r^2 dr$, using the ideal gas equation of state. It follows that the relationship between the gravitational potential energy and the internal energy for a spherically symmetric ideal gas in hydrostatic equilibrium is given by

$$\Omega = -3(\gamma - 1)U. \tag{2.2.23}$$

Consider the thermal kinetic energy of this gaseous configuration. For a fluid element, there are dN number of molecules and the kinetic energy for each molecule is $3k\mathcal{T}/2$. The total contribution for the fluid element is then $dE_{\mathcal{T}} = 3k\mathcal{T}dN/2 = 3(\gamma-1)c_V\mathcal{T}dm/2$, in terms of specific heat c_v. The internal energy of the fluid element is given by $dU = c_V\mathcal{T}dm$. Then, for the whole configuration, the thermal kinetic energy is given by $E_{\mathcal{T}} = \frac{3}{2}(\gamma-1)U$. In accordance with the virial theorem, it follows that $E_{\mathcal{T}} = -\frac{1}{2}\Omega$.

Equilibrium configurations characterized by a polytropic equation of state are referred to as polytropes. Substituting the adiabatic (polytropic) equation of state into the expression for Ω (2.2.22),

$$\Omega = -\frac{3(\gamma-1)}{5\gamma-6}\frac{GM_*^2}{R_*}. \tag{2.2.24}$$

The total energy of the polytrope is then

$$E_{\text{tot}} = U + \Omega = -\left(\frac{3\gamma-4}{5\gamma-6}\right)\frac{GM_*^2}{R_*}. \tag{2.2.25}$$

We next show how to obtain the dimensionless envelope structure of the polytrope, characterized by the polytropic index n, using the Lane-Emden equation [46]. By combining the hydrostatic equilibrium conditions, (2.2.20) and (2.2.21), we obtain the fundamental equation

$$\frac{1}{r^2}\frac{d}{dr}\left(\frac{r^2}{\rho}\frac{dP}{dr}\right) = -4\pi G\rho. \tag{2.2.26}$$

Define the polytropic index n by $\gamma \equiv 1 + 1/n$. Consider the dimensionless Lane-Emden variables ξ and $\theta(\xi)$ such that the radius of the star is

$$r = a\xi, \qquad a = \left[\frac{(n+1)\kappa}{4\pi G}\rho_c^{1/n-1}\right]^{1/2}, \tag{2.2.27}$$

where constant κ is defined by the equation of state $p = \kappa\rho^{\gamma}$. Consider another dimensionless Lane-Emden variable, $\theta(\xi)$. The density and pressure radial profiles may be written in terms of this variable and are given by

$$\rho(\xi) = \rho_c \theta(\xi)^n, \qquad\qquad p(\xi) = p_c \theta(\xi)^{n+1}, \tag{2.2.28}$$

where ρ_c and p_c are the central values. We re-cast the fundamental equation (2.2.26) in terms of ξ and θ and obtain the Lane-Emden equation of index n,

$$\frac{1}{\xi^2}\frac{d}{d\xi}\left(\xi^2 \frac{d\theta}{d\xi}\right) = -\theta^n. \tag{2.2.29}$$

The boundary conditions at the origin are

$$\theta\Big|_{\xi=0} = 1, \qquad\qquad \frac{d\theta}{d\xi}\Big|_{\xi=0} = 0. \tag{2.2.30}$$

To get the density and pressure profiles, we must solve the Lane-Emden equation. Except for a few special n, this is done numerically. For $n < 5$, the solution decreases monotonically with the first zero $\theta(\xi_1) = 0$ corresponding to the surface of the star,

$$R_* = a\xi_1 = \left[\frac{(n+1)\kappa}{4\pi G}\rho_c^{1/n-1}\right]\xi_1. \tag{2.2.31}$$

The central density and pressure are

$$\rho_c = -\left[\frac{\xi}{3}\frac{1}{d\theta_n/d\xi}\right]_{\xi=\xi_1}\bar{\rho}, \qquad\qquad p_c = W_n \frac{GM_*^2}{R_*^4}, \tag{2.2.32}$$

where $\bar{\rho} = M_*/(4\pi R_*^3/3)$ and $W_n = [4\pi(n+1)[(d\theta_n/d\xi)_{\xi=\xi_1}]^2]^{-1}$. The total mass at a distance ξ is $M_*(\xi) = -4\pi a^3 \rho_c \xi^2 d\theta/d\xi$ and for the entire star,

$$M_* = -4\pi\left[\frac{(n+1)\kappa}{4\pi G}\right]^{3/2}\rho_c^{(3-n)/2n}\left(\xi^2\frac{d\theta_n}{d\xi}\right)_{\xi=\xi_1}. \tag{2.2.33}$$

We eliminate ρ_c from this equation using (2.2.31) to obtain the *mass-radius relation* for a polytrope,

$$GM_*^{(n-1)/n}R_*^{(3-n)/n} = \frac{(n+1)\kappa}{(4\pi)^{1/n}}\left[-\xi^{(n+1)/(n-1)}\frac{d\theta_n}{d\xi}\right]_{\xi=\xi_1}^{(n-1)/n}. \tag{2.2.34}$$

Rewriting, the constant κ in terms of M_* and R_* is given by

$$\kappa = N_n G M_*^{(n-1)/n} R_*^{(3-n)/n}, \qquad N_n = \frac{1}{n+1}\left(\frac{4\pi}{{}_0\omega_n^{n-1}}\right)^{1/n}, \tag{2.2.35}$$

where ${}_0\omega_n = -\xi_1^{(n+1)/(n-1)}(d\theta_n/d\xi)_{\xi=\xi_1}$.

Re-writing the fundamental equation (2.2.26) in terms of the self-gravitational potential Φ where $dp/dr = \rho(d\Phi/dr)$, we have Poisson's equation,

$$\frac{1}{r^2}\frac{d}{dr}\left(r^2\frac{d\Phi}{dr}\right) = \nabla^2\Phi = 4\pi G\rho. \tag{2.2.36}$$

We may write the solution for inside and outside the star as

$$\Phi(\xi) = \begin{cases} -4\pi G a^2 \rho_c \theta(\xi) - \frac{GM_*}{R_*}, & r < R_*, \\ -\frac{GM_*}{r}, & r \geq R_*. \end{cases} \tag{2.2.37}$$

In Table 2.1, the first zero of the Lane-Emden equation and the relevant quantities for calculating the central density and pressure are given for n=1.5, 2, and 3 polytropes [46, 49, 50].

n	ξ_1	$(d\theta_n/d\xi)_{\xi=\xi_1}$	$-\left[\frac{\xi}{3}\frac{1}{d\theta_n/d\xi}\right]_{\xi=\xi_1}$	Remark
1.5	3.6537534	2.033013E-1	5.990705	(non-relativistic white dwarf)
2.0	4.35287460	1.272487E-1	1.140254E1	
3.0	6.89684862	4.242976E-2	5.148248E1	(extreme relativistic white dwarf)

Table 2.1: Properties given for different polytropes. We give the first zero of the Lane-Emden equation, ξ_1, and $d\theta_n/d\xi$ and $\xi(d\theta_n/d\xi)^{-1}/3$ evaluated at ξ_1.

2.3 Newtonian star in a Newtonian tidal field

In the following, the tidal interaction between the black hole and a polytropic star is presented within the Newtonian formulation. The mass moments and other integrals characterizing the fluid star are introduced [51, 29]. We show the effects of tidal heating and tidal spin-up of the star. We derive the deviation between the equation of motion for the center of mass of the star and the origin of a coordinate system on a point-particle trajectory.

2.3.1 Momentum equation in a coordinate system following the star

Assume that the star is a Newtonian fluid. Consider an inertial coordinate system (X_k, T) with origin fixed on the black hole (assuming the black hole is so massive its motion can be neglected). The velocity of the material moving in the gravitational field of the black hole will be taken to be $V_k(T)$. The density and pressure are $\rho(X_k, T)$ and $p(X_k, T)$. The convective derivative taken along streamlines (Stokes time derivative) is given by

$$\frac{d}{dT} = \frac{\partial}{\partial T} + V_k \frac{\partial}{\partial X_k}. \tag{2.3.1}$$

The continuity equation for the fluid in the black hole frame is written as

$$\frac{d\rho}{dT} + \rho \frac{\partial V_k}{\partial X_k} = \frac{\partial \rho}{\partial T} + \frac{\partial}{\partial X_k}(\rho V_k) = 0 \tag{2.3.2}$$

and the momentum equation is written as

$$\rho \frac{dV_k}{dT} = \rho \frac{\partial V_k}{\partial T} + \rho V_l \frac{\partial V_k}{\partial X_l} = -\frac{\partial p}{\partial X_k} - \rho \frac{\partial \Phi^*}{\partial X_k} + \rho g_k^t, \tag{2.3.3}$$

where Φ^* is the star's self-gravitational potential and g_k^t is the external black hole tidal acceleration field.

Let $X_k^{(0)}(T)$ and $V_k^{(0)}(T) = dX_k^{(0)}/dT$ denote the position and velocity of the origin of a coordinate system following the star (in a way to be described precisely below). Define

$$x_k = X_k - X_k^{(0)}(T) \qquad\qquad v_k = V_k - V_k^{(0)}(T), \tag{2.3.4}$$

as positions and velocities relative to the origin of the moving system. We rewrite the continuity and momentum equations in this frame (x_k, t) by considering the following change of variables. Let $f = \{x_k, t\}$ and $g = \{X_k, T\}$. The Jacobian matrix is

$$J = \begin{pmatrix} \frac{\partial f_1}{\partial g_1} & \frac{\partial f_2}{\partial g_1} \\ \frac{\partial f_1}{\partial g_2} & \frac{\partial f_2}{\partial g_2} \end{pmatrix} = \begin{pmatrix} \frac{\partial x_k}{\partial X_k} & \frac{\partial t}{\partial X_k} \\ \frac{\partial x_k}{\partial T} & \frac{\partial t}{\partial T} \end{pmatrix} = \begin{pmatrix} 1 & 0 \\ -V_k^{(0)} & 1 \end{pmatrix}. \tag{2.3.5}$$

Then, the change of variables is the following,

$$\frac{\partial}{\partial X_k} = \frac{\partial}{\partial x_k}, \qquad\qquad \frac{\partial}{\partial T} = \frac{\partial}{\partial t} - V_l^{(0)} \frac{\partial}{\partial x_l}. \tag{2.3.6}$$

The continuity equation in a coordinate frame following the star is then

$$\frac{\partial \rho}{\partial t} - V_k^{(0)}\frac{\partial \rho}{\partial x_k} + \frac{\partial}{\partial x_k}\left[\rho(V_k^{(0)} + v_k)\right] = \frac{\partial \rho}{\partial t} + \frac{\partial}{\partial x_k}(\rho v_k) = 0, \tag{2.3.7}$$

where $\partial V_k^{(0)}/\partial x_k = 0$. This has the same form as the equation in the black hole frame. Similarly, we apply the transformation to the momentum equation and get

$$\rho\frac{\partial v_k}{\partial t} + \rho v_l \frac{\partial v_k}{\partial x_l} = \rho\frac{dv_k}{dt} = -\frac{\partial p}{\partial x_k} - \rho\frac{\partial \Phi^*}{\partial x_k} + \rho g_k^t - \rho\frac{dV_k^{(0)}}{dt}, \tag{2.3.8}$$

where $-\rho dV_k^{(0)}/dt$ is the coordinate acceleration term.

2.3.2 Relevant moments and tensors defined

Consider the following theorem, for any quantity $Q(x_k, t)$,

$$\frac{d}{dt}\int \rho\, Q d^3x = \int \rho\frac{dQ}{dt}d^3x. \tag{2.3.9}$$

This may be proved by introducing Lagrangian coordinates, ξ_k, fixed to the fluid elements, where

$$x_k = x_k(\xi_l, t), \qquad dx_k = \frac{\partial x_k}{\partial \xi_l}d\xi_l + \frac{\partial x_k}{\partial t}dt, \qquad v_k = \frac{\partial x_k}{\partial \xi_l}\dot{\xi}_l + \frac{\partial x_k}{\partial t}. \tag{2.3.10}$$

The transformation between different volume elements, connected by Jacobian J is $d^3x = |\partial x_k/\partial \xi_l| \equiv Jd^3\xi$. Then,

$$\frac{d}{dt}\left(\frac{\partial x_k}{\partial \xi_l}\right) = \frac{\partial x_k}{\partial \xi_m \partial \xi_l}\dot{\xi}_m + \frac{\partial x_k}{\partial t \partial \xi_l} = \frac{\partial}{\partial \xi_l}\left(\frac{\partial x_k}{\partial \xi_m}\dot{\xi}_m + \frac{\partial x_k}{\partial t}\right) = \frac{\partial v_k}{\partial \xi_l}, \tag{2.3.11}$$

where in the new coordinate system ξ_m and $\dot{\xi}_m$ are independent, so that $\partial \dot{\xi}_m/\partial \xi_k = 0$. We write

$$\begin{aligned}\frac{d}{dt}\int \rho\, Qd^3x &= \frac{d}{dt}\int \rho\, QJd^3\xi = \int Q\frac{d}{dt}(\rho J)d^3\xi + \int \frac{dQ}{dt}\rho J d^3\xi \\ &= \int Q\left(\frac{d\rho}{dt}J + \rho\frac{dJ}{dt}\right)d^3\xi + \int \frac{dQ}{dt}\rho J d^3\xi \\ &= \int Q\left(\frac{d\rho}{dt} + \rho\frac{d}{dt}\ln J\right)Jd^3\xi + \int \frac{dQ}{dt}\rho J d^3\xi = \int \frac{dQ}{dt}\rho J d^3\xi,\end{aligned} \tag{2.3.12}$$

where we have that

$$\frac{d\rho}{dt} = -\rho\frac{\partial v_k}{\partial x_k}, \qquad \text{and} \qquad \frac{d}{dt}\ln J = \frac{\partial \xi_l}{\partial x_k}\frac{d}{dt}\left(\frac{\partial x_k}{\partial \xi_l}\right) = \frac{\partial \xi_l}{\partial x_k}\frac{\partial v_k}{\partial \xi_l} = \frac{\partial v_k}{\partial x_k}. \tag{2.3.13}$$

The *zeroth moment* ($Q = 1$) is defined as

$$M_* \equiv \int_{\mathcal{V}} \rho d^3x, \tag{2.3.14}$$

over a volume $\mathcal{V}$. Define the *first mass moment* and derivatives as

$$D_k \equiv \int_{\mathcal{V}} \rho x_k d^3x, \qquad \dot{D}_k = \int_{\mathcal{V}} \rho v_k d^3x, \qquad \ddot{D}_k = \int_{\mathcal{V}} \rho \frac{dv_x}{dt} d^3x. \tag{2.3.15}$$

The *moment of inertia tensor*, or second mass moment, and its derivative are defined as

$$I_{ij} \equiv \int_{\mathcal{V}} \rho x_i x_j d^3x, \qquad \dot{I}_{ij} = \int_{\mathcal{V}} \rho(x_i v_j + v_i x_j) d^3x. \tag{2.3.16}$$

The *moment of inertia* I follows from taking the trace,

$$I \equiv I_{ii} = \int_{\mathcal{V}} \rho r^2 d^3x. \tag{2.3.17}$$

Likewise we can define a third moment, or *octupole moment tensor*, as

$$I_{ijk} = \int \rho x_i x_j x_k d^3x. \tag{2.3.18}$$

The fluid configuration may have angular momentum, which is described by the tensor,

$$J_{ij} \equiv \tfrac{1}{2} \int_{\mathcal{V}} \rho(x_i v_j - v_i x_j) d^3x. \tag{2.3.19}$$

We see that

$$\int_{\mathcal{V}} \rho x_i v_j d^3x = \tfrac{1}{2}\dot{I}_{ij} + J_{ij}, \qquad \int_{\mathcal{V}} \rho v_i x_j d^3x = \tfrac{1}{2}\dot{I}_{ij} - J_{ij}, \tag{2.3.20}$$

where $I_{ij} = I_{ji}$ and $J_{ij} = -J_{ji}$ [51, 29]. The *kinetic energy tensor* and *kinetic energy* are defined as

$$T_{ij} \equiv \tfrac{1}{2} \int_{\mathcal{V}} \rho v_i v_j d^3x, \qquad T \equiv T_{ii} = \tfrac{1}{2} \int_{\mathcal{V}} \rho v^2 d^3x. \tag{2.3.21}$$

With all of this in hand, it is possible to make the following connection,

$$\int_{\mathcal{V}} \rho x_i \ddot{x}_j d^3x = \tfrac{1}{2}\ddot{I}_{ij} + \dot{J}_{ij} - 2T_{ij}. \tag{2.3.22}$$

Next, we consider the gravitational effects. Define the *self-gravitational potential* as

$$\Phi^*(x) \equiv -G \int_{\mathcal{V}} \frac{\rho(x')d^3x'}{|x-x'|} \tag{2.3.23}$$

and the *self-gravitational potential energy* as

$$\Omega \equiv \tfrac{1}{2} \int_{\mathcal{V}} \Phi^* \rho d^3x \equiv -\tfrac{1}{2} G \int_{\mathcal{V}} \int_{\mathcal{V}} \frac{\rho(x)\rho(x')d^3x d^3x'}{|x-x'|}. \tag{2.3.24}$$

This scalar quantity is a part of a more general *self-gravitational energy tensor*, given by

$$\Omega_{ij} \equiv -\tfrac{1}{2} G \int \int \frac{(x_i - x_i')(x_j - x_j')}{|x-x'|^3} \rho(x)\rho(x')d^3x d^3x'. \tag{2.3.25}$$

Then, we see that $\Omega = \Omega_{ii}$. Consider the spatial derivative of Φ^*,

$$\partial_i \Phi^* = -G \int_{\mathcal{V}} \frac{x_i - x_i'}{|x-x'|^3} \rho(x')d^3x'. \tag{2.3.26}$$

Then, due to symmetry it is fairly easy to show that

$$\begin{aligned} -\int x_i(\partial_j \Phi^*)\rho d^3x &= -G \int \int \frac{x_i(x_j - x_j')}{|x-x'|} \rho(x)\rho(x')d^3x d^3x' \\ &= -\tfrac{1}{2} G \int \int \frac{(x_i - x_i')(x_j - x_j')}{|x-x'|} \rho(x)\rho(x')d^3x d^3x' \\ &= \Omega_{ij}. \end{aligned} \tag{2.3.27}$$

From the symmetry of Ω_{ij} it follows that

$$\int x_i(\partial_j \Phi^*)\rho d^3x = \int x_j(\partial_i \Phi^*)\rho d^3x. \tag{2.3.28}$$

Note that the *gravitational self-force* vanishes,

$$\int (\partial_i \Phi^*)\rho d^3x = G \int \frac{x_i - x_i'}{|x-x'|^3} \rho(x)\rho(x')d^3x d^3x' = 0, \tag{2.3.29}$$

as can be seen by the interchange of $x_k \leftrightarrow x_k'$. Then we have an important alternative expression for the gravitational energy,

$$\Omega = \tfrac{1}{2} \int \Phi^* \rho d^3x = -\int x_i(\partial_i \Phi^*)\rho d^3x. \tag{2.3.30}$$

The *gravitational self-potential tensor* is defined as

$$\Phi^*_{ij} \equiv -G \int \frac{(x_i - x'_i)(x_j - x'_j)}{|x - x'|^3} \rho(x') d^3x', \tag{2.3.31}$$

where

$$\Omega_{ij} = \tfrac{1}{2} \int \Phi^*_{ij} \rho d^3x. \tag{2.3.32}$$

With some work, we can show that the *rate of change of gravitational energy* is

$$\dot{\Omega} = \int v_i \partial_i \Phi^* \rho d^3x. \tag{2.3.33}$$

We now consider the various fluid energies. The *pressure moments* are given by

$$\Pi = \int_{\mathcal{V}} p d^3x, \qquad \Pi_i = \int_{\mathcal{V}} p x_i d^3x, \qquad \Pi_{ij} = \int_{\mathcal{V}} p x_i x_j d^3x. \tag{2.3.34}$$

We can show that the *change in total internal energy* is

$$\dot{U} = \int v_k \partial_k p d^3x. \tag{2.3.35}$$

Consider the effects of an external gravitational field. Let the *external force density* be $f^t_i = \rho g^t_i = -\rho \partial_i \Phi^t$. Then, we have the *net force on the fluid* and the *moment of force tensor*,

$$F^t_i = \int f^t_i d^3x = \int \rho g^t_i d^3x, \qquad F^t_{ij} = \int x_i f^t_j d^3x = \int x_i g^t_j \rho d^3x. \tag{2.3.36}$$

The *rate at which work is done by the external force* is

$$\dot{W}^t = \int v_i f^t_i d^3x = \int v_i g^t_i \rho d^3x. \tag{2.3.37}$$

We have obtained the gravitational potentials and energies and energies associated with the fluid. We will use these quantities in the following to calculate the rate of change of energy of the star and will later include the work done by the external gravitational field and the acceleration of the reference frame.

2.3.3 Equation of motion for the origin of the coordinate system following the star

Consider the momentum equation (2.3.8) in the moving frame. We can integrate the momentum equation over a comoving volume,

$$\int_{\mathcal{V}} \rho \frac{dv_k}{dt} d^3x = -\cancelto{0}{\int_{\mathcal{V}} \frac{\partial p}{\partial x^k} d^3x} - \cancelto{0}{\int_{\mathcal{V}} \rho \frac{\partial \Phi^*}{\partial x^k} d^3x} + F_k^t - M_* \dot{V}_k^{(0)}. \tag{2.3.38}$$

Two of the terms vanish (as shown) because (1) the pressure at the surface of the fluid configuration is assumed to vanish and (2) the gravitational self-force is zero, as we previously showed. Writing in terms of the first moment, we find

$$\int_{\mathcal{V}} \rho \frac{dv_k}{dt} d^3x = \frac{d}{dt} \int \rho v_k d^3x = \frac{d^2}{dt^2} \int \rho x_k d^3x = \frac{d^2}{dt^2} D_k, \tag{2.3.39}$$

Thus we have a relationship between the acceleration of the coordinate system, $\dot{V}_k^{(0)}$, the net external force, F_k^t, and the motion of the fluid configuration,

$$\ddot{D}_k = F_k^t - M_* \dot{V}_k^{(0)}. \tag{2.3.40}$$

We are free to choose $\dot{V}_k^{(0)}$. We may enforce the initial condition $D_k = 0$ and $\dot{D}_k = 0$. If we take the acceleration of the frame $\dot{V}_k^{(0)}$ to be equal to the external acceleration F_k^t/M_*, then the center of mass does not accelerate in the coordinate frame $\{x_k\}$ and the frame following the star $\{x_k\}$ is the center-of-mass (CM) frame. Alternatively, we might take $\dot{V}_k^{(0)}$ to be that of a point mass (original center of mass) moving in the external potential. The forces applied to the extended body can drive apparent acceleration of the CM. In our calculations we choose this latter case in considering the relativistic tidal field in Chapter 3.

2.3.4 Tensor virial theorem

Consider the first moment of the momentum equation in a frame following the star, (2.3.8),

$$\int_{\mathcal{V}} x_i \rho \frac{dv_k}{dt} d^3x = -\int_{\mathcal{V}} x_i \frac{\partial p}{\partial x^k} d^3x - \int_{\mathcal{V}} x_i \rho \frac{\partial \Phi^*}{\partial x^k} d^3x + \int_{\mathcal{V}} x_i g_k^t \rho d^3x - \int_{\mathcal{V}} \rho x_i \dot{V}_k^{(0)} d^3x. \tag{2.3.41}$$

Then, from previous definitions of moments and tensors, Subsection 2.3.2,

$$\tfrac{1}{2}\ddot{I}_{ik} + \dot{J}_{ik} - 2T_{ik} = \Pi \delta_{ik} + \Omega_{ik} + F_{ik}^t - D_i \dot{V}_k^{(0)}. \tag{2.3.42}$$

We may split this into antisymmetric and symmetric parts,

$$
\begin{aligned}
\dot{J}_{ik} &= \tfrac{1}{2}(F^t_{ik} - F^t_{ki}) - \tfrac{1}{2}\left(D_i \dot{V}^{(0)}_k - D_k \dot{V}^{(0)}_i\right) \\
\tfrac{1}{2}\ddot{I}_{ik} &= 2T_{ik} + \Pi\delta_{ik} + \Omega_{ik} + \tfrac{1}{2}(F_{ik} + F_{ki}) - \tfrac{1}{2}(D_i \dot{V}^{(0)}_k + D_k \dot{V}^{(0)}_i).
\end{aligned}
\tag{2.3.43}
$$

In the center-of-mass frame ($D_i = 0$) and without an external force ($F_{ik} = 0$), the spin angular momentum of the star is conserved ($\dot{J}_{ik} = 0$) and we have the following *tensor virial theorem*,

$$
\tfrac{1}{2}\ddot{I}_{ik} = 2T_{ik} + \Pi\delta_{ik} + \Omega_{ik}. \tag{2.3.44}
$$

2.3.5 Rate of change of energy of the star

We may contract the momentum equation in the frame following the star (2.3.8) with v_k and integrate

$$
\begin{aligned}
\int \rho v_k \dot{v}_k d^3x &= -\int v_k \partial_k p d^3x - \int v_k(\partial_k \Phi^*)\rho d^3x + \int v_k g^t_k \rho d^3x - \int v_k \dot{V}^{(0)}_k \rho d^3x \\
\tfrac{1}{2}\frac{d}{dt}\int \rho v_k v_k d^3x &= -\frac{dU}{dt} - \frac{d\Omega}{dt} + \dot{W}^t - \dot{D}_k \dot{V}^{(0)}_k \\
\dot{T} + \dot{U} + \dot{\Omega} &= \dot{W}^t - \dot{D}_k \dot{V}^{(0)}_k,
\end{aligned}
\tag{2.3.45}
$$

and obtain the rate of change of energy of the fluid. The left hand side is the rate of change of total energy of the fluid in the accelerated frame without external forces. The right hand side is the rate at which work is done by the external gravitational field and a correction term if the accelerated frame is not the center of mass frame. We obtain an expression for the work done by the tidal field, $\dot{W}^t$, in the following. Let $\Phi^t(X_k, t)$ be the external potential from which g^t_k is derived,

$$
g^t_k = -\frac{\partial}{\partial X_k}\Phi^t = -\frac{\partial}{\partial x_k}\Phi^t = -\partial_k \Phi^t. \tag{2.3.46}
$$

Then,

$$
\begin{aligned}
\dot{W}^t &= \int \rho v_k g^t_k d^3x = -\int v_k(\partial_k \Phi^t)\rho d^3x = -\int \left(\frac{d\Phi^t}{dt} - \frac{\partial \Phi^t}{\partial t}\right)\rho d^3x \\
&= -\frac{d}{dt}\int \Phi^t \rho d^3x + \int \frac{\partial \Phi^t}{\partial t}\rho d^3x.
\end{aligned}
\tag{2.3.47}
$$

The external gravitational energy of the star is given by $\Theta = \int \Phi^t \rho d^3x$. Then, using the transformation of the partial derivative of the inertial frame time,

$$\begin{aligned} \dot{W}^t &= -\dot{\Theta} + \int \left[\left(\frac{\partial}{\partial T} + V_k^{(0)} \partial_k \right) \Phi^t \right] \rho d^3x \\ &= -\dot{\Theta} + F_k^t V_k^{(0)} + \int \left(\frac{\partial \Phi^t}{\partial T} \right) \rho d^3x. \end{aligned} \tag{2.3.48}$$

With the equation of motion of the center of mass, (2.3.40), we have an expression for the work done by the tidal field,

$$\dot{W}^t = -\dot{\Theta} - \tfrac{1}{2} M_* \frac{d}{dt} \left(V_k^{(0)} V_k^{(0)} \right) - \ddot{D}_k V_k^{(0)} + \int \left(\frac{\partial \Phi^t}{\partial T} \right) \rho d^3x. \tag{2.3.49}$$

Define the bulk *kinetic energy of a star as seen in the inertial frame* to be

$$T_{(0)} = \tfrac{1}{2} M_* V_k^{(0)} V_k^{(0)}. \tag{2.3.50}$$

The time dependence of the total energy is then

$$\frac{d}{dt}(T + U + \Omega) + \frac{d}{dt}\Theta + \frac{d}{dt} T_{(0)} = -\frac{d}{dt}\left(\dot{D}_k v_k^{(0)} \right) + \int \left(\frac{\partial \Phi^t}{\partial T} \right) \rho d^3x. \tag{2.3.51}$$

If we choose the center-of-mass frame, then $D_k = 0$. If we further assume there is no intrinsic variations in the external potential, e.g. $\partial \Phi^t / \partial T = 0$, then the total energy is conserved.

2.3.6 Tidal potential and tidal field

In the following, we will specify the form of the external force. In this section, we will assume it derives from the potential of a heavy point mass and is time dependent. Expanding the tidal potential Φ^t about some trajectory $X_k^{(0)}(t)$,

$$\begin{aligned} \Phi^t &= \Phi_t^{(0)} - g_i^{(0)} x_i + \tfrac{1}{2} C_{ij}^{(0)} x_i x_j + \tfrac{1}{6} C_{ijk}^{(0)} x_i x_j x_k + \tfrac{1}{24} C_{ijkl}^{(0)} x_i x_j x_k x_l + \cdots, \\ g_k^t &= -\partial_k \Phi^t = g_k^{(0)} - C_{ki}^{(0)} x_i - \tfrac{1}{2} C_{kij}^{(0)} x_i x_j - \tfrac{1}{6} C_{kijl}^{(0)} x_i x_j x_l + \cdots, \end{aligned} \tag{2.3.52}$$

where $[R_{(0)}^2(t) = X_k^{(0)} X_k^{(0)}]$,

$$
\begin{aligned}
\Phi_t^{(0)} &= -\frac{GM_*}{R_{(0)}}, \qquad g_k^{(0)} = -\frac{GM_* X_k^{(0)}}{R_{(0)}^3}, \\
C_{ij}^{(0)} &= \partial_i \partial_j \Phi^t \Big|_{(0)} = \frac{GM_*}{R_{(0)}^5} \left(\delta_{ij} R_{(0)}^2 - 3 X_i^{(0)} X_j^{(0)} \right), \\
C_{ijk}^{(0)} &= \partial_i \partial_j \partial_k \Phi^t \Big|_{(0)} = \frac{GM_*}{R_{(0)}^7} \left(15 X_i^{(0)} X_j^{(0)} X_k^{(0)} - 3R_{(0)}^2 X_j^{(0)} \delta_{ik} - 3R_{(0)}^2 X_k^{(0)} \delta_{ij} - 3R_{(0)}^2 X_i^{(0)} \delta_{jk} \right),
\end{aligned}
$$

etc. The *net force* is then

$$
F_k^{(0)} = \int \rho g_k^t d^3x = M_* g_k^{(0)} - C_{ki}^{(0)} D_i - \tfrac{1}{2} C_{kij}^{(0)} I_{ij} - \tfrac{1}{6} C_{kijl}^{(0)} I_{ijl} + \cdots . \tag{2.3.53}
$$

The *first moment of the force density* is

$$
F_{ij} = \int x_i g_j^t \rho d^3x = D_i g_j^{(0)} - C_{jk}^{(0)} I_{ik} - \tfrac{1}{2} C_{jkl}^{(0)} I_{ikl} + \cdots . \tag{2.3.54}
$$

The rate of work done by the tidal field becomes

$$
\dot{W}^t = \int \rho v_k g_k^t d^3x = \dot{D}_k g_k^{(0)} - C_{ki}^{(0)} \int \rho v_k x_i d^3x - \tfrac{1}{2} C_{kij}^{(0)} \int \rho v_k x_i x_j d^3x + \cdots . \tag{2.3.55}
$$

Note that

$$
\int \rho v_k x_i d^3x = \tfrac{1}{2} \dot{I}_{ik} + J_{ik}, \tag{2.3.56}
$$

from above, and that the product $C_{ki}^{(0)} J_{ik}$ vanishes since C_{ki} is symmetric and J_{ik} is antisymmetric. Define $M_{ijk} \equiv \int \rho v_i x_j x_k d^3x$, where $M_{ijk} = M_{ikj}$. We see that

$$
\dot{I}_{ijk} = \int \rho (v_i x_j x_k + v_j x_i x_k + v_k x_i x_j) d^3x = M_{ijk} + M_{jik} + M_{kij}. \tag{2.3.57}
$$

and

$$
C_{kij}^{(0)} M_{kij} = \tfrac{1}{3} \left(C_{kij}^{(0)} + C_{ijk}^{(0)} + C_{jik}^{(0)} \right) M_{kij} = \tfrac{1}{3} C_{kij}^{(0)} \dot{I}_{ijk}. \tag{2.3.58}
$$

Then, the tidal gravitational work has the expansion,

$$
\dot{W}^t = \dot{D}_k g_k^{(0)} - \tfrac{1}{2} C_{ki}^{(0)} \dot{I}_{ik} - \tfrac{1}{6} C_{kij}^{(0)} \dot{I}_{ijk} + \cdots . \tag{2.3.59}
$$

We can also obtain an expansion for the external gravitational energy of the star,

$$\Theta = M_* \Phi_t^{(0)} - D_i g_i^{(0)} + \tfrac{1}{2} C_{ij}^{(0)} I_{ij} + \tfrac{1}{6} C_{ijk}^{(0)} I_{ijk} + \cdots . \tag{2.3.60}$$

2.3.7 Center of mass frame vs. point-particle frame

We may rewrite the equation of motion for the origin of a coordinate system following the star (2.3.40) and substitute the net force (2.3.53) to get

$$M_* \ddot{X}_k + \ddot{D}_k = g_k - C_{ki}(X) D_i - \tfrac{1}{2} C_{kij}(X) I_{ij} - \tfrac{1}{6} C_{kijl}(X) I_{ijl} + \cdots . \tag{2.3.61}$$

For center of mass coordinates, we set D_k and its derivatives to be zero. Then,

$$M_* \ddot{X}_k^{(0)} = -GM_* \frac{X_k^{(0)}}{R^3} - \tfrac{1}{2} C_{kij}(X^{(0)}) I_{ij} - \tfrac{1}{6} C_{kijl}(X^{(0)}) I_{ijl} + \cdots , \qquad \ddot{D}_k = 0. \tag{2.3.62}$$

If we would like to use CM coordinates, then equation (2.3.62) must be integrated in time. Furthermore, the motion of the origin is affected not only by the external point potential but also by the octupole and higher-order tides.

If the coordinate system follows a point particle trajectory, then the origin is not guaranteed to be coincident with the center of mass. Then the equation of motion for the origin is

$$M_* \ddot{X}_k^{(p)} = -GM_* \frac{X_k^{(p)}}{R_p^3}, \tag{2.3.63}$$

and the mass moment evolves according to,

$$\ddot{D}_k = -C_{ki}(X^{(p)}) D_i - \tfrac{1}{2} C_{kij}(X^{(p)}) I_{ij} - \tfrac{1}{6} C_{kijl}(X^{(p)}) I_{ijl} + \cdots . \tag{2.3.64}$$

We see that the center of mass will follow a trajectory that accelerates away from the point-particle trajectory, $g_k(X) = GM_* X_k / R^3$, because of the octupole tide and higher order corrections. Let ζ_k be the difference in position of the center of mass and the point particle trajectory, $\zeta_k \equiv X_k - X_k^{(p)}$. Then, the deflection of the center of mass from the origin of the coordinate system following the star is given by the following,

$$\ddot{\zeta}_k = -\tfrac{1}{2} C_{kij}(X) \frac{1}{M_*} I_{ij}(t) - \tfrac{1}{6} C_{kijl}(X) \frac{1}{M_*} I_{ijk}(t). \tag{2.3.65}$$

2.3.8 Change in orbital angular momentum due to the spin-up of star and acceleration of center of mass

We write the total angular momentum of the star in the black hole frame as

$$\mathcal{J}_{kl} = \int d^3X \rho(X,t)(X_k V_l - X_l V_k). \tag{2.3.66}$$

We substitute $X_k = x_k + X_k^{(0)}(t)$ and $V_k = v_k + V_k^{(0)}(t)$ to obtain an expression accounting for the spin angular momentum and the position and velocity of the center of mass with respect to the origin of the point-particle frame. We have that

$$\begin{aligned}
\mathcal{J}_{kl} &= \int d^3x\rho \left[(x+X^{(0)})_k(v+V^{(0)})_l - (x+X^{(0)})_k(v+V^{(0)})_l\right] \\
&= \int d^3x\rho(x_iv_j - v_ix_j) + \int d^3x\rho(x_kV_l^{(0)} - x_lV_k^{(0)}) \\
&\quad - \int d^3x\rho(v_kX_l^{(0)} - v_lX_k^{(0)}) + \int d^3x\rho(X_k^{(0)}V_l^{(0)} - X_l^{(0)}V_k^{(0)}) \\
&= J_{kl} + D_kV_l^{(0)} - D_lV_k^{(0)} - \dot{D}_kX_l^{(0)} + \dot{D}_lX_k^{(0)} + M_*(X_k^{(0)}V_l^{(0)} - X_l^{(0)}V_k^{(0)}),
\end{aligned}$$

where J_{kl} is the spin angular momentum in the point-particle frame (2.3.19) and D_l is the first mass moment defined by (2.3.15). The time rate of change of the last term vanishes if we choose a point-particle trajectory for the reference frame that does not change. The time rate of change of total angular momentum is

$$\dot{\mathcal{J}}_{kl} = \dot{J}_{kl} + \frac{d}{dt}\left(D_kV_l^{(0)} - D_lV_k^{(0)} - \dot{D}_kX_l^{(0)} + \dot{D}_lX_k^{(0)}\right), \tag{2.3.67}$$

where the first term corresponds to the change in spin angular momentum of the star and the rest corresponds to the change in orbital angular momentum.

2.4 Non-disruptive encounters

2.4.1 Regime of weak tidal interactions

Consider encounters of a star with a black hole characterized by $\eta > 1$. The tidal interaction is weak and the star does not disrupt upon passing the black hole, but becomes distorted or and excited into a set of pulsational modes. Gas may be tidally stripped off of the star. For non-disruptive encounters, one may apply the linear, adiabatic theory of tidal interactions to compute the excitation of the non-radial oscillations of the perturbed star [26, 52, 27, 38].

Under this formalism, we assume that the star is initially spherically symmetric, static, and in hydrostatic equilibrium. The tidal interaction induces a slight perturbation from the initial state. We write the perturbed variable f' in terms of the initial state f and the pertubation δf as $f' = f + \delta f$ and obtain linearized versions of the equations of hydrodynamics and heat flow by neglecting all powers above the first and products of the variations. We may express the perturbation variables in terms of spherical harmonics and associate with each l, m a set of normal modes of oscillation, representing a fundamental mode and overtones. Stars will pulsate in both pressure modes (p-modes) and gravity modes (g-modes).

2.4.2 Energy and angular momentum deposited on the star

The amount of orbital energy deposited into oscillatory modes during a close periastron passage depends upon two dimensionless parameters: the dimensionless envelope structure of the star, the polytropic index n, and the dimensionless parameter characterizing the encounter, the disruption parameter η [26]. We calculate the amount of energy removed from the orbit and deposited onto the star as follows.

Consider a coordinate system centered on the star in the orbital plane. Let ρ be the density of the star, $\vec{v}$ be the fluid velocity, and U be defined as $U(\vec{r}, t) = -\Phi^t = GM/|\vec{r} - \vec{R}(t)|$, where $\vec{R}(t)$ is the relative orbit of the point mass, M. The rate at which energy is deposited onto the star is given by

$$\frac{dE}{dt} = \dot{W}^t = \int d^3x \rho \vec{v} \cdot \vec{\nabla} U = < \vec{v} | \vec{\nabla} U > . \tag{2.4.1}$$

Consider a linearized perturbation analysis on the effect of $\vec{\nabla} U$ on the equilibrium star. Let ρ be the unperturbed stellar density. Express the fluid velocity in terms of a Lagrangian displacement ξ of the fluid element from its unperturbed position as $\vec{v} = \partial \xi / \partial t$, where the Fourier transform of ξ may be analyzed into normal modes. These normal modes satisfy a linear, self-adjoint eigenvalue equation and may be written in terms of spherical harmonics. The amplitude of the tidal perturbation is of the form $U_{lm} \sim GMr^l / R(t)^{l+1}$, in terms of spherical harmonic indices l and m. The time dependence of the perturbation in U_{lm} is fixed by Keplerian motion and the disruption parameter η (2.1.1), which relates the duration of periastron passage to the hydrodynamic timescale of the star. Thus, for a given encounter, η, the amplitude of tidally induced oscillations scales as U_{lm}. The energy deposited into oscillations of spherical harmonic index l is then

$$\Delta E_l = \frac{GM_*^2}{R_*}\left(\frac{M}{M_*}\right)^2\left(\frac{R_*}{R_p}\right)^{2l+2} T_l(\eta), \tag{2.4.2}$$

where $T_l(\eta)$ is a dimensionless function and may be explicitly calculated using the normal modes for a given polytrope of index n. The total energy is given by $\Delta E = \sum_{l=2,3,...}\Delta E_l$. The dimensionless function $T_l(\eta)$ is calculated for $n = 3$ polytropes in Press and Teukolsky [26] and for $n = 1.5, 2, 3$ in Lee and Ostriker (1986) [27]. It is shown that the $l = 2$ f-mode dominate the tidal energy transfer. A quick method for obtaining the results from the latter was given by Portegies Zwart and Meinen (1993) [53]. We obtain T_l from the following polynomial,

$$\log T_l(\eta) = \mathcal{A} + \mathcal{B}x + \mathcal{C}x^2 + \mathcal{D}x^3 + \mathcal{E}x^4 + \mathcal{F}x^5, \tag{2.4.3}$$

where $x = \log\eta$. Table 2.2 gives the polynomial coefficients for the $l = 2$ and $l = 3$ contribution to (2.4.3) for a polytrope of index $n = 1.5$.

n=1.5	l=2	l=3
$\mathcal{A}$	-0.397	-0.909
$\mathcal{B}$	1.678	1.574
$\mathcal{C}$	1.277	12.37
$\mathcal{D}$	-12.42	-57.40
$\mathcal{E}$	9.446	80.10
$\mathcal{F}$	-5.550	-46.43

Table 2.2: Polynomial coefficients for fit of dimensionless function $T_l(\eta)$ for $l = 2, 3$. These are given for an $n = 1.5$ polytrope.

Along with energy, the black hole deposits angular momentum onto the star. A star that is initally at rest will "spin-up" as it passes by the black hole. From studies in comparing the affine model with the linear theory, it is found that although energy is transferred into the $l = 2$, $m = -2$ f-mode, which should possess angular momentum and vorticity, the star bulk rotates just enough to cancel out the vorticity [28]. It is shown that the star may be modeled as an irrotational ellipsoid. Thus, for weak encounters, we may assume that the energy, ΔE, and angular momentum, ΔL, deposited onto the star are related by

$$\Delta E \simeq \frac{|\Omega|}{\sqrt{15}}\frac{\Delta L}{\sqrt{I_*|\Omega|}}, \tag{2.4.4}$$

where $I_* = \frac{1}{3}\int r^2 dM$ is the moment-of-inertia coefficient and Ω is the self-gravitational potential energy of the star [28]. Despite the relativistic treatment of the tidal field in our calculations (Chapter 3), the special coordinate system that we use allows us to apply the Newtonian linear perturbation theory in the limit of weak encounters.

2.5 Disruptive encounters

In this section, we describe the situation where the star disrupts and make some estimates for the debris that is released during this type of encounter. We will see in this analysis a dependence on various dimensionless parameters.

2.5.1 Spread of energies

Consider the following quantities associated with the Newtonian parabolic orbit of the star. The velocity at periastron is $v_p = (2GM/R_p)^{1/2}$. The angular momentum is $l_p = M_*(2GMr_p)^{1/2}$. The specific kinetic energy at periastron is $\epsilon_p = GM/R_p$. The gravitational potential of the black hole at periastron is $|\Phi_p| = GM/R_p$. As discussed in Rees (1988) [1] and Evans and Kochanek (1989) [32], the tides will raise on the star and as the bulge attempts to stay aligned with the direction of the black hole the star will be torqued. The maximal surface velocity is $v_* = (2GM_*/R_*)^{1/2}$. The maximal spin angular momentum is $l_* = M_*(2GM_*R_*)^{1/2}$. The specific binding energy of the star is $\epsilon_* = GM_*/R_*$. The self-gravitational potential of the star at the stellar radius is $|\Phi_*| = GM_*/R_*$. We compare the quantities associated with the star and the orbit in terms of the mass ratio $\mu = M_*/M$, which we regard as small ($\mu \ll 1$), and the disruption parameter η as

$$\frac{v_*}{v_p} = \mu^{1/3}\eta^{-1/3}, \qquad \frac{l_*}{l_p} = \mu^{2/3}\eta^{1/3}, \qquad \frac{\epsilon_*}{\epsilon_p} = \mu^{2/3}\eta^{-2/3}, \qquad \frac{\Phi_*}{\Phi_p} = (\mu\eta)^{2/3}. \tag{2.5.1}$$

The disruption of the star reduces the specific orbital energy, ϵ_p, by the specific binding energy, ϵ_*. The variation in the specific energy of the released gas, $\Delta\epsilon$, depends on the change in the black hole potential across the diameter of the star [1, 32, 54]. For a star at periastron, the gravitational potential at $R_p + R_*$ and $R_p - R_*$ may be written as

$$\epsilon_\pm = -\frac{GM}{R_p \pm R_*} = -\frac{GM}{R_p}\left(1 \pm \frac{R_*}{R_p}\right)^{-1} = -\frac{GM}{R_p}\left(1 \mp \frac{R_*}{R_p}\right). \tag{2.5.2}$$

The spread of energies of the gas is then

$$\Delta\epsilon = \frac{GM}{R_p}\frac{R_*}{R_p} = \epsilon_p \mu^{1/3} = \epsilon_* \mu^{-1/3}\eta^{2/3}. \tag{2.5.3}$$

Note that $\epsilon_p \gg \Delta\epsilon \gg \epsilon_*$.

Since the variation in the specific energy of the released gas is much larger than the specific binding energy, in the absence of hydrodynamic forces, we estimate that roughly 50% of the star (located from $r = R_p$ to $r = R_p + R_*$) will become unbound during disruption while the other half, from $r = R_p - R_*$ to $r = R_p$, will return to periastron after following a set of highly eccentric orbits. The maximum velocity at infinity of the ejected debris may be given as $v_{\rm esc} = (2\Delta\epsilon)^{1/2}$.

2.5.2 Accretion rate

Once disruption occurs, the kinetic energy of the expanding debris is much larger than the adiabatically decreasing internal energy and diminishing self-gravitional energy. Thus, we can describe the debris as locked into Keplerian trajectories and estimate a spread of energy of $\simeq 2\Delta\epsilon$ with a mass distribution of $dM/d\epsilon \simeq M_*/2\Delta\epsilon$ [32]. The total energy of the most tightly bound gas can be related to a semi-major axis a_m by $\Delta\epsilon = -GM/(2a_m)$. Then,

$$a_m = -\frac{GM}{2\Delta\epsilon} = GM\frac{R_p}{2GM}\left(\frac{R_p}{R_*}\right) = \frac{R_p^2}{2R_*}. \tag{2.5.4}$$

The minimum (Keplerian) period before return to the hole is then

$$\tau_m = \frac{2\pi a_m^{3/2}}{\sqrt{GM}} = \frac{\pi}{\sqrt{2GM}}\left(\frac{R_p^2}{R_*}\right)^{3/2}. \tag{2.5.5}$$

We may write

$$\frac{d\epsilon}{d\tau} = \frac{d\epsilon}{da}\frac{da}{d\tau} = \tfrac{1}{3}\left(2\pi GM\right)^{2/3}\tau^{-5/3}. \tag{2.5.6}$$

The estimated rate at which mass returns to the black hole after one post-disruption orbit is

$$\frac{dM_*}{d\tau} = \frac{dM_*}{d\epsilon}\frac{d\epsilon}{d\tau} = \frac{M_*}{2}\left(\frac{R_*}{R_p}\frac{GM}{R_p}\right)\tfrac{1}{3}\left(2\pi GM\right)^{2/3}\tau^{-5/3} = \tfrac{1}{3}\frac{M_*}{\tau_m}\left(\frac{\tau}{\tau_m}\right)^{-5/3}. \tag{2.5.7}$$

Newtonian simulations of debris motion after disruption appear to confirm this expected $\tau^{-5/3}$ dependence [32, 34, 35].

In this chapter, we have presented the mechanism of tidal disruption in the Newtonian limit.

We have shown our assumptions for the fate of the Newtonian star, modeled as a polytrope, which undergoes tidal accelerations from a large central (point) mass. We show a difference in the equation of motion for the center of mass of the star and the origin of a coordinate system on a point-particle trajectory. In Chapter 3, we introduce a coordinate system on a point-particle trajectory for our calculations of tidal disruption. We will show in Chapter 5 that the center of mass of the star does indeed accelerate off of the origin of our coordinate system. As we have shown here, it is not a relativistic effect, but due to the Newtonian octupole and higher-order terms in the expansion of the tidal potential.

Chapter 3

The Relativistic Tidal Field: Fermi Normal Coordinates

If we assume Newtonian gravity and hydrodynamics are adequate to describe the star and it moves non-relativistically in a Newtonian tidal field, then the formalism of the previous chapter is adequate. The latter requirement holds as long as the minimum distance in the orbit is large enough that relativistic effects or corrections can be ignored. In this thesis, we are concerned with *relativistic tidal interactions* between a massive black hole and a white dwarf star. However, despite the need to consider relativistic orbital and tidal effects, we will also show that it is possible to simultaneously use Newtonian calculations for the star's self-gravity and hydrodynamics. In principle, we could also treat the self-gravity and hydrodynamics of the white dwarf with general relativity. However, this is a small correction [$\mathcal{O}(10^{-4})$] which we choose to ignore. Despite the fact that the first stellar post-Newtonian correction is $\mathcal{O}(10^{-4})$, the tidal field involves a set of relativistic, orbital post-Newtonian corrections that fall off less abruptly depending upon the depth of the encounter and the mass ratio of the system.

In this chapter, we explain in detail the treatment of the relativistic tidal field. First, the coordinate system for our calculations, Fermi normal coordinates, is introduced. We then show the expansion of the metric in this coordinate system for a general spacetime. Second, the form of the metric is specified to be the Schwarzschild black hole spacetime and the components of the Riemann tensor in this spacetime are given. Third, we introduce geodesic motion on Schwarzschild and show the relevant equations of motion of a point mass on a parabolic orbit (a marginally bound orbit with zero kinetic energy at infinity). The parameterization and integration scheme, known as the Darwin method, is presented. Next, we construct the Fermi normal frame along a parabolic geodesic and show the form of the metric expansion up through quartic order in the distance from the geodesic. We justify the usage of terms in this tidal potential with a post-Newtonian formalism. In the fourth and fifth section of this chapter, we present simultaneous expansions of the metric in terms of the self-gravity of the star and the tidal gravity. Finally, we show the fluid equations of motion of the white dwarf in the relativistic tidal field and justify the retention of certain terms in the tidal expansion.

3.1 Form of the metric in Fermi normal coordinates

In this section, we introduce the Fermi normal coordinates, which are used to calculate the tidal encounter. We begin by presenting the metric expansion at an event using the local flatness theorem. This notion of local flatness is then extended to events all along a timelike geodesic through the adoption of Fermi normal coordinates. We show the form of the expansion of the metric in this coordinate system for a general spacetime.

3.1.1 Metric expansion at an event

In curved spacetime, let $\mathcal{P}_0$ be an event and at that point define a coordinate system x^a with indices $a = 0, 1, 2, 3$ and coordinate basis vectors $\boldsymbol{\lambda}_a = \partial/\partial x^a$. The metric defines an inner product and, when acting on the basis vectors, its components are given as $g_{ab} \equiv \boldsymbol{\lambda}_a \cdot \boldsymbol{\lambda}_b$. The local-flatness theorem [55] states that in a local Lorentz frame at an event $\mathcal{P}_0$, the metric can be taken as Minkowskian, η_{ab},

$$g_{ab}\Big|_{\mathcal{P}} = \eta_{ab} = \mathrm{diag}(-1, 1, 1, 1). \tag{3.1.1}$$

Furthermore, at $\mathcal{P}_0$, it is also possible to require that the derivatives of the metric vanish, $g_{ab,c}\Big|_{\mathcal{P}_0} = 0$. From the definition of the connection coefficients in a coordinate basis [56],

$$\Gamma^a{}_{bc} = \tfrac{1}{2} g^{ad}(g_{db,c} + g_{dc,b} - g_{bc,d}), \tag{3.1.2}$$

the vanishing of the first derivatives of the metric at $\mathcal{P}_0$ implies that all of the connection coefficients also vanish, $\Gamma^a{}_{bc} = 0$. However, in curved spacetime the derivatives of the connection will not be zero in general. Thus, the metric at $\mathcal{P}_0$ is locally flat such that it appears Minkowskian up to terms that are quadratic in the distance from $\mathcal{P}_0$,

$$g_{ab} = \eta_{ab} + \mathcal{O}(x^2). \tag{3.1.3}$$

The quadratic terms cannot all be made to vanish by a choice of coordinates and they represent the tidal contributions of the gravitational field.

3.1.2 Metric expansion along a timelike geodesic

The view of local flatness at an event may be generalized to include the extended motion of a freely-falling observer. Consider an arbitrary spacetime with coordinates $x^{\mu'}$. Consider further a timelike geodesic $\mathcal{G}$ in this spacetime described by $x^{\mu'} = x^{\mu'}(\tau)$ and parameterized by proper time τ. Let Greek indices, including a prime (e.g., μ'), denote these arbitrary coordinates in this spacetime. Let $\mathcal{G}$ have the tangent vector $\mathbf{u} = \partial/\partial\tau$. The local-flatness theorem is extended by defining a second coordinate system x^a, the origin of which moves along the trajectory $\mathcal{G}$ [57, 55], with the following Fermi conditions being enforced, at all times,

$$g_{ab}\Big|_{\mathcal{G}} = \eta_{ab}, \qquad\qquad \Gamma^a{}_{bc}\Big|_{\mathcal{G}} = 0. \tag{3.1.4}$$

Here Latin indices $(a, b, c, ...)$ denote the four new coordinates, which span $(0, 1, 2, 3)$, and subsequently we will take any index beginning with i (e.g., $i, j, k...$) to denote one of the three new spatial coordinates $(1, 2, 3)$. Let $\mathcal{P}_0$ be a single event on the geodesic $\mathcal{G}$ at $\tau = 0$. Construct an orthonormal tetrad $\boldsymbol{\lambda}_a = (\boldsymbol{\lambda}_0, \boldsymbol{\lambda}_1, \boldsymbol{\lambda}_2, \boldsymbol{\lambda}_3)$ at this point. Choose $\boldsymbol{\lambda}_0 = \mathbf{u}$ such that the tangent vector of the geodesic is itself one of the basis vectors (and obviously timelike). Construct a basis all along $\mathcal{G}$ by insisting that the tetrad $\boldsymbol{\lambda}_a$ is parallel-transported along $\mathcal{G}$. This is already satisfied for $\boldsymbol{\lambda}_0$, since $\nabla_{\mathbf{u}}\boldsymbol{\lambda}_0 = \nabla_{\mathbf{u}}\mathbf{u} = 0$, but the conditions must also be imposed on the spacelike vectors $\boldsymbol{\lambda}_i$, such that $\nabla_{\mathbf{u}}\boldsymbol{\lambda}_i = 0$. Having defined the moving tetrad, each $\boldsymbol{\lambda}_i$ is used, at any constant time τ, to launch spacelike geodesics from $\mathcal{P}(\tau)$. The proper distance along the curve launched by $\boldsymbol{\lambda}_i$ becomes the spatial coordinate x^i. The proper time along $\mathcal{G}$, τ, becomes the time coordinate $x^0 = \tau$. See Figure 3.1. This coordinate system $x^a = (x^0, x^i)$ is known as the Fermi normal coordinate (FNC) system. In this coordinate system we have not only $\Gamma^a{}_{bc}\Big|_{\mathcal{G}} = 0$ and $g_{ab,c}\Big|_{\mathcal{G}}$ (3.1.4), but also that all of the time derivatives of the connection vanish, $\Gamma^a{}_{bc,0} = \Gamma^a{}_{bc,00} = 0$ and $g_{ab,c0} = g_{ab,c00} = 0$. Hence, it can be shown [57, 55, 58] that the metric may be expanded in a power series in spatial distance of the form

$$g_{ab} = \eta_{ab} + \tfrac{1}{2} g_{ab,ij}(\tau) x^i x^j + \tfrac{1}{6} g_{ab,ijk}(\tau) x^i x^j x^k + \tfrac{1}{24} g_{ab,ijkl}(\tau) x^i x^j x^k x^l + \mathcal{O}(x^5), \tag{3.1.5}$$

where only spatial derivatives of the metric appear and the derivatives of the metric are functions of the FNC time coordinate τ only.

Furthermore, these coefficients may be obtained from the Riemann curvature of the spacetime evaluated along $\mathcal{G}$. The series expansion has been derived to quadratic order by Manasse and Misner (1963) [57] and up to quartic order by Ishii, Shibata, and Mino (2005) [58]. Using the results obtained

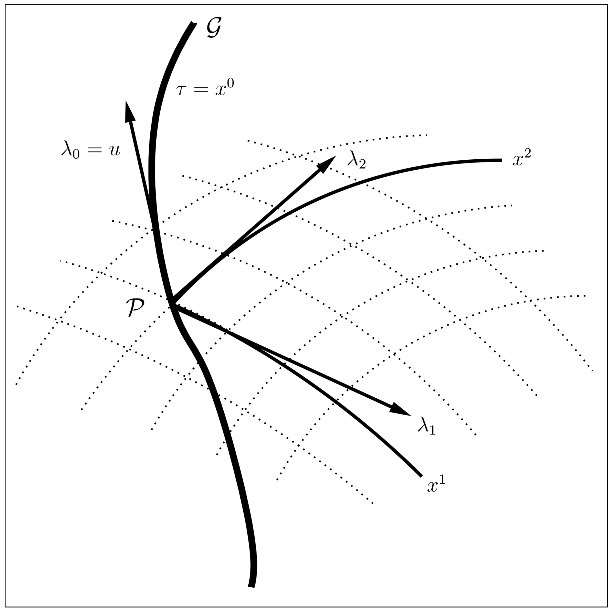

Figure 3.1: The Fermi normal coordinate system constructed along a geodesic $\mathcal{G}$. The diagram above displays only three dimensions $(0, 1, 2)$ of the FNC system, $x^a = (x^0, x^1, x^2, x^3)$. The orthonormal tetrad $\boldsymbol{\lambda}_a = (\boldsymbol{\lambda}_0, \boldsymbol{\lambda}_1, \boldsymbol{\lambda}_2, \boldsymbol{\lambda}_3)$ constructed at a point $\mathcal{P}$ is parallel transported along the timelike geodesic $\mathcal{G}$. Note that $\boldsymbol{\lambda}_0$ is the tangent vector of the geodesic itself. The spatial basis vectors $\boldsymbol{\lambda}_1$ and $\boldsymbol{\lambda}_2$ are orthogonal to each other and to $\boldsymbol{\lambda}_0$ all along $\mathcal{G}$. Parallel transport of each $\boldsymbol{\lambda}_i$ along itself defines spacelike geodesics and thus the spatial coordinates away from $\mathcal{G}$.

by Ishii et al., the components may be written explicitly as

$$\begin{aligned}
g_{00} &= -1 - R_{0i0j}x^i x^j - \tfrac{1}{3}R_{0(i|0|j;k)}x^i x^j x^k \\
&\quad -\tfrac{1}{12}\left(R_{0(i|0|j;kl)} - 4R^{\mu}_{(kl|0|}R_{|\mu|ij)0}\right)x^i x^j x^k x^l + \cdots\,, \\
g_{0m} &= \tfrac{1}{3}(R_{0ijm} + R_{0jim})x^i x^j + \tfrac{1}{4}R_{m(ij|0|;k)}x^i x^j x^k \\
&\quad +\tfrac{1}{135}\left(9R_{m(ij|0|;kl)} - 6R_{m(ij}{}^{0}R_{|0|kl)0} - 2R_{m(ij}{}^{n}R_{|n|kl)0}\right)x^i x^j x^k x^l \cdots\,, \\
g_{mn} &= \delta_{mn} + \tfrac{1}{6}\left(R_{imnj} + R_{inmj}\right)x^i x^j \\
&\quad -\tfrac{1}{36}\left(R_{injm;k} + R_{inkm;j} + R_{jnim;k} + R_{knim;j} + R_{knjm;i} + R_{jnkm;i}\right)x^i x^j x^k \\
&\quad +\tfrac{1}{180}\left(9R_{m(ij|n|;kl)} - 6R_{m(ij}{}^{0}R_{|n|kl)0} - 2R_{m(ij}{}^{p}R_{|n|kl)p}\right)x^i x^j x^k x^l + \cdots\,,
\end{aligned} \tag{3.1.6}$$

where, as mentioned, the components of the Riemann tensor and its derivatives are evaluated along

$\mathcal{G}$ and are only functions of time, $x^0 = \tau$. In the above, parentheses around indices indicate symmetrization of a tensor, defined by, for example,

$$A_{(ij)} = \tfrac{1}{2}(A_{ij} + A_{ji}), \tag{3.1.7}$$

$$A_{(ijk)} = \tfrac{1}{6}\left(A_{ijk} + A_{jik} + A_{jki} + A_{kji} + A_{kij} + A_{ikj}\right), \tag{3.1.8}$$

and, more generally, by

$$A_{(\alpha_1 \cdots \alpha_l)} = \tfrac{1}{l!} \sum_l A_{\alpha_{f(1)} \cdots \alpha_{f(l)}}, \tag{3.1.9}$$

where the sum ranges over all permutations of the indices $\alpha_1 \cdots \alpha_l$. Vertical strokes, e.g., $|n|$, indicate that that index is excluded from the symmetrization.

Thus, it is possible to express the expansion of the metric in the FNC *if* the Riemann tensor and its derivatives in the FNC are known. This reverses the usual prescription that the Riemann tensor be obtained by differentiation once the metric is known. Fortunately, what is only needed is the Riemann tensor computed in *some* coordinate system (e.g., $R_{\mu'\alpha'\nu'\beta'}$), which is then transformed from this coordinate system to the FNC. The components of the FNC tetrad vectors in the original coordinates are the elements of the Jacobian transformation matrix along $\mathcal{G}$, $\lambda_a{}^{\mu'} = \partial x^{\mu'}/\partial x^a \Big|_{\mathcal{G}}$. The Riemann tensor and its covariant derivatives in the FNC frame may be obtained by projecting the Riemann tensor and its covariant derivative in the original spacetime coordinates into the FNC frame,

$$R_{abcd} = R_{\mu'\alpha'\nu'\beta'}\, \lambda_a{}^{\mu'}\, \lambda_b{}^{\alpha'}\, \lambda_c{}^{\nu'}\, \lambda_d{}^{\beta'}, \tag{3.1.10}$$

$$R_{abcd;e} = R_{\mu'\alpha'\nu'\beta';\rho'}\, \lambda_a{}^{\mu'}\, \lambda_b{}^{\alpha'}\, \lambda_c{}^{\nu'}\, \lambda_d{}^{\beta'}\, \lambda_e{}^{\rho'}, \tag{3.1.11}$$

$$R_{abcd;ef} = R_{\mu'\alpha'\nu'\beta';\rho'\sigma'}\, \lambda_a{}^{\mu'}\, \lambda_b{}^{\alpha'}\, \lambda_c{}^{\nu'}\, \lambda_d{}^{\beta'}\, \lambda_e{}^{\rho'}\, \lambda_f{}^{\sigma'}. \tag{3.1.12}$$

3.2 The Schwarzschild black hole and components of the Riemann tensor

Up to this point in the discussion, a completely arbitrary background spacetime and set of coordinates $x^{\mu'}$ have been assumed. It was shown that the existence of the FNC is independent of the details of the spacetime. Since tidal encounters of stars passing by a black hole are of interest, in this section we work out necessary details of the Schwarzschild black hole. The more general case of a Kerr black hole may be considered at a later time. The coordinates are specified as standard

Schwarzschild coordinates, $x^{\mu'} = \{t, r, \theta, \phi\}$. The Schwarzschild metric is given by

$$ds^2 = -f dt^2 + f^{-1} dr^2 + r^2 \left(d\theta^2 + \sin^2\theta d\phi^2 \right), \tag{3.2.1}$$

where $f(r) = 1 - 2M/r$. Using (3.1.2), the Christoffel symbols are given by

$$\begin{aligned}
&\Gamma^{t'}{}_{t'r'} = \frac{M}{r^2 f}, && \Gamma^{r'}{}_{t't'} = \frac{Mf}{r^2}, && \Gamma^{r'}{}_{r'r'} = -\frac{M}{r^2 f}, \\
&\Gamma^{\theta'}{}_{r'\theta'} = \frac{1}{r}, && \Gamma^{\phi'}{}_{r'\phi'} = \frac{1}{r}, && \Gamma^{r'}{}_{\theta'\theta'} = -rf, \\
&\Gamma^{\phi'}{}_{\theta'\phi'} = \cot\theta, && \Gamma^{r'}{}_{\phi'\phi'} = -rf\sin^2\theta, && \Gamma^{\theta'}{}_{\phi'\phi'} = -\sin\theta\cos\theta.
\end{aligned} \tag{3.2.2}$$

Note that the primes on the coordinates themselves have been dropped for brevity, but the primes are retained on component labels to clearly distinguish them from the FNC frame components. The components of the Riemann tensor [56] in a coordinate basis are given by

$$R^{\alpha}{}_{\beta\gamma\delta} = \Gamma^{\alpha}{}_{\beta\delta,\gamma} - \Gamma^{\alpha}{}_{\beta\gamma,\delta} + \Gamma^{\alpha}{}_{\mu\gamma}\Gamma^{\mu}{}_{\beta\delta} - \Gamma^{\alpha}{}_{\mu\delta}\Gamma^{\mu}{}_{\beta\gamma}. \tag{3.2.3}$$

Then, in the Schwarzschild spacetime,

$$\begin{aligned}
&R_{t'r't'r'} = -\frac{2M}{r^3}, && R_{t'\theta't'\theta'} = \frac{Mf}{r}, && R_{t'\phi't'\phi'} = \frac{Mf\sin^2\theta}{r}, \\
&R_{r'\theta'r'\theta'} = -\frac{M}{rf}, && R_{r'\phi'r'\phi'} = -\frac{M}{rf}\sin^2\theta, && R_{\theta'\phi'\theta'\phi'} = 2Mr\sin^2\theta.
\end{aligned} \tag{3.2.4}$$

Other nonzero components follow from the symmetries $R_{\mu'\alpha'\nu'\beta'} = -R_{\mu'\alpha'\beta'\nu'} = -R_{\alpha'\mu'\nu'\beta'} = +R_{\nu'\beta'\mu'\alpha'}$. All other elements vanish.

Consider instead of the Schwarzschild coordinate basis the use of an orthonormal frame. The standard tetrad, $e_{(a)}{}^{\mu'}$, are a set of vectors such that [59]

$$\mathbf{e}_{(a)} \cdot \mathbf{e}_{(b)} = e_{(a)}{}^{\mu'} e_{(b)}{}^{\nu'} g_{\mu'\nu'} = \eta_{(a)(b)}. \tag{3.2.5}$$

Here (a) labels the different tetrad vectors and μ' denotes their Schwarzschild coordinate basis components. From this, the dual elements $e^{(a)}{}_{\mu'}$ can be defined such that

$$\delta_{(a)}{}^{(b)} = e_{(a)}{}^{\mu'} e^{(b)}{}_{\mu'}, \qquad \delta^{\mu'}{}_{\nu'} = e_{(a)}{}^{\mu'} e^{(a)}{}_{\nu'}. \tag{3.2.6}$$

Summing over the dual elements, the components of the metric in the coordinate basis may be obtained by

$$g_{\mu'\nu'} = e_{(a)\mu'}e^{(a)}{}_{\nu'} = \eta_{(a)(b)}\ e^{(a)}{}_{\mu'}e^{(b)}{}_{\nu'}. \tag{3.2.7}$$

Here the tetrad index (a) is lowered/raised with the Minkowski metric $\eta_{(a)(b)}$ and the coordinate index μ' is raised/lowered with the metric tensor $g_{\mu'\nu'}$; i.e.,

$$e_{(a)}{}^{\mu'} = \eta_{(a)(b)}\ g^{\mu'\nu'}e^{(b)}{}_{\nu'}. \tag{3.2.8}$$

The standard tetrad in Schwarzschild then is given by

$$\begin{aligned} e_{(0)}{}^{\mu'} &= \left(f^{-1/2}, 0, 0, 0\right), \qquad & e_{(1)}{}^{\mu'} &= \left(0, f^{1/2}, 0, 0\right), \\ e_{(2)}{}^{\mu'} &= \left(0, 0, \frac{1}{r}, 0\right), & e_{(3)}{}^{\mu'} &= \left(0, 0, 0, \frac{1}{r\sin\theta}\right). \end{aligned} \tag{3.2.9}$$

Then lowering the coordinate index gives

$$\begin{aligned} e_{(0)\mu'} &= \left(-f^{1/2}, 0, 0, 0\right), \qquad & e_{(1)\mu'} &= \left(0, f^{-1/2}, 0, 0\right), \\ e_{(2)\mu'} &= (0, 0, r, 0), & e_{(3)\mu'} &= (0, 0, 0, r\sin\theta). \end{aligned} \tag{3.2.10}$$

Raising the tetrad index of the standard tetrad gives

$$\begin{aligned} e^{(0)\mu'} &= \left(-f^{-1/2}, 0, 0, 0\right), \qquad & e^{(1)\mu'} &= \left(0, f^{1/2}, 0, 0\right), \\ e^{(2)\mu'} &= \left(0, 0, \frac{1}{r}, 0\right), & e^{(3)\mu'} &= \left(0, 0, 0, \frac{1}{r\sin\theta}\right). \end{aligned} \tag{3.2.11}$$

Raising the tetrad index of the standard tetrad and lowering the coordinate index gives the dual basis elements

$$\begin{aligned} e^{(0)}{}_{\mu'} &= \left(f^{1/2}, 0, 0, 0\right), \qquad & e^{(1)}{}_{\mu'} &= \left(0, f^{-1/2}, 0, 0\right), \\ e^{(2)}{}_{\mu'} &= (0, 0, r, 0), & e^{(3)}{}_{\mu'} &= (0, 0, 0, r\sin\theta). \end{aligned} \tag{3.2.12}$$

Using the tetrad and its components, the Riemann tensor in the Schwarzschild coordinate basis can be transformed to the standard tetrad basis by

$$R_{(a)(b)(c)(d)} = R_{\alpha'\beta'\mu'\nu'}\ e_{(a)}{}^{\alpha'}\ e_{(b)}{}^{\beta'}\ e_{(c)}{}^{\mu'}\ e_{(d)}{}^{\nu'}, \tag{3.2.13}$$

The non-zero components of the Riemann tensor in the standard tetrad are then found to be

$$R_{(0)(1)(0)(1)} = -\frac{2M}{r^3}, \qquad R_{(0)(2)(0)(2)} = \frac{M}{r^3}, \qquad R_{(0)(3)(0)(3)} = \frac{M}{r^3}, \tag{3.2.14}$$
$$R_{(1)(2)(1)(2)} = -\frac{M}{r^3}, \qquad R_{(1)(3)(1)(3)} = -\frac{M}{r^3}, \qquad R_{(2)(3)(2)(3)} = \frac{2M}{r^3}, \tag{3.2.15}$$

where again symmetries of the Riemann tensor (e.g., $R_{(0)(1)(0)(1)} = R_{(1)(0)(1)(0)} = -R_{(0)(1)(1)(0)}$) yield the remaining nonzero elements. We will also have need of the projections of the first and second covariant derivatives of $R_{\mu'\alpha'\nu'\beta'}$ [58]:

$$\begin{aligned} Q_{(a)(b)(c)(d)(e)} &= R_{\mu'\alpha'\nu'\beta';\sigma'} e_{(a)}{}^{\sigma'} e_{(b)}{}^{\mu'} e_{(c)}{}^{\alpha'} e_{(d)}{}^{\nu'} e_{(e)}{}^{\beta'}, \\ P_{(a)(b)(c)(d)(e)(f)} &= R_{\mu'\alpha'\nu'\beta';\sigma'\lambda'} e_{(a)}{}^{\sigma'} e_{(b)}{}^{\lambda'} e_{(c)}{}^{\mu'} e_{(d)}{}^{\alpha'} e_{(e)}{}^{\nu'} e_{(f)}{}^{\beta'}. \end{aligned} \tag{3.2.16}$$

These frame components have been computed with Mathematica and are a lengthy list. They are not listed here for brevity.

3.3 Geodesic motion on Schwarzschild and the construction of the Fermi normal coordinate frame

In this section, we present the equations of motion for a test body on a parabolic orbit in Schwarzschild spacetime. We introduce the Darwin method which is used to integrate the equations of motion and provides a parameterization of the geodesic in terms of a specific set of orbital parameters and constants of motion. Next, we show how to obtain the Fermi normal coordinate frame vectors using the formalism first developed by Manasse and Misner (1963) [57] and further developed by Marck (1983) [60].

3.3.1 Darwin method for integrating the geodesic equations

The timelike geodesic equations may be obtained from the Lagrangian $\mathcal{L}$ defined by the line element, $2\mathcal{L} = g_{\mu'\nu'} dx^{\mu'} dx^{\nu'}$ [56]. In the Schwarzschild spacetime, the coordinates t and ϕ are cyclic variables and we define the following constants of motion in terms of the 1-form $u_{\mu'} = g_{\mu'\nu'} u^{\nu'}$, where $u^{\mu'} = dx^{\mu'}/d\tau$, as

$$-E = u_{t'}, \qquad L = u_{\phi'}. \tag{3.3.1}$$

Here E is the specific orbital energy and L is the specific angular momentum. If we consider geodesics confined to the equatorial plane, $\theta = \pi/2$, then there are only three first-order equations of motion given by

$$\frac{dt}{d\tau} = u^t = \frac{E}{f(r)}, \qquad \frac{d\phi}{d\tau} = u^\phi = \frac{L}{r^2}, \qquad \left(\frac{dr}{d\tau}\right)^2 = (u^r)^2 = E^2 - V, \tag{3.3.2}$$

where $V \equiv f(1+L^2/r^2)$ is the effective potential for radial motion. For parabolic orbits, the specific orbital energy is $E = 1$, which is the limit of motion bound to the black hole.

We obtain the equations for a general geodesic using the Darwin method, which parameterizes an orbit in terms of the semi-latus rectum, p, and eccentricity, e [61, 62, 63]. This allows us to consider bound orbits, though we can also specialize to $e = 1$, $E = 1$ (parabolic) motion. Let r_1 represent periastron and r_2 be apastron. Define p and e as

$$r_1 = \frac{pM}{1+e}, \qquad r_2 = \frac{pM}{1-e}. \tag{3.3.3}$$

The specific energy and angular momentum may written in terms of these parameters by

$$E^2 = \frac{(p-2-2e)(p-2+2e)}{p(p-3-e^2)}, \qquad L^2 = \frac{p^2M^2}{p-3-e^2}. \tag{3.3.4}$$

Darwin defines a radial phase χ such that the orbital radius R is given by

$$R(\chi) = \frac{pM}{1+e\cos\chi}, \tag{3.3.5}$$

where $R(\chi = 0) = r_1$ and $R(\chi = \pi) = r_2$. The proper time is obtained in terms of the new phase angle by integrating

$$\frac{d\tau}{d\chi} = \frac{p^{3/2}M}{(1+e\cos\chi)^2}\left(\frac{p-3-e^2}{p-6-2e\cos\chi}\right)^{1/2} \tag{3.3.6}$$

and the azimuthal coordinate is related to χ by integrating

$$\frac{d\phi}{d\chi} = p^{1/2}\left(p-6-2e\cos\chi\right)^{-1/2}. \tag{3.3.7}$$

Thus with the Darwin scheme, we obtain a complete reparameterization of the orbit, i.e., $\tau = \tau(\chi)$,

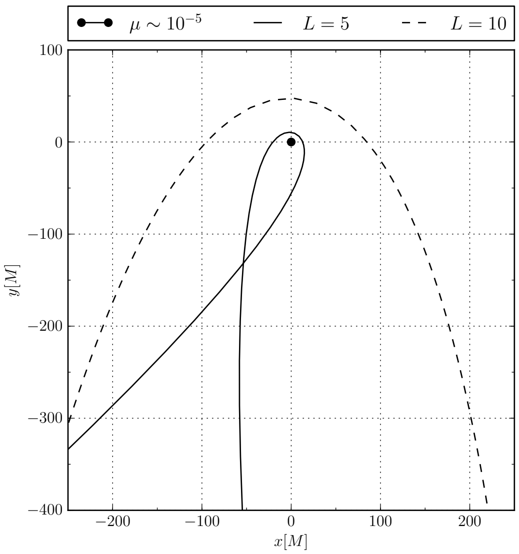

Figure 3.2: Parabolic orbits with different orbital angular momentum. The plot above gives two parabolic orbits ($E = 1$) with large (dotted line) and small (solid line) specific orbital angular momentum L. Note that the precession of the orbit is much more noticeable with smaller L.

$r = r(\chi)$, and $\phi = \phi(\chi)$.

For parabolic orbits, define $r_1 = R_p$ and take $r_2 = \infty$. R_p is the periastron distance. Then,

$$pM = 2R_p, \qquad e = 1, \qquad E = 1, \qquad L^2 = \frac{p^2M^2}{p-4}. \tag{3.3.8}$$

In Figure 3.2, parabolic orbits with different specific orbital angular momentum L are shown.

3.3.2 FNC frame vectors

In the following we shall first construct the Fermi normal frame vectors and express them in terms of Schwarzschild coordinate components. We enforce the condition $\nabla_{\mathbf{u}}\boldsymbol{\lambda}_a = 0$ where the four-velocity is given by

$$u^{\mu'} = \left(\frac{E}{f}, u^r, 0, \frac{L}{r^2}\right). \tag{3.3.9}$$

The parallel transport condition may be written as

$$u^{\nu'}\nabla_{\nu'}\lambda_a{}^{\mu'} = 0 = u^{\nu'}\partial_{\nu'}\lambda_a{}^{\mu'} + \Gamma^{\mu'}{}_{\alpha'\beta'}u^{\alpha'}\lambda_a{}^{\beta'}. \tag{3.3.10}$$

We choose ${\lambda_0}^{\mu'} = u^{\mu'}$ to automatically provide one of the tetrad vectors. To find the spatial vectors, we exploit the orthonormality condition ${\lambda_a}^{\mu'} {\lambda_b}^{\nu'} g_{\mu'\nu'} = \eta_{ab}$ (3.2.5). Assuming that the spatial vector pointing out of the orbital plane is of the form ${\lambda_2}^{\mu'} = (0, 0, b_2, 0)$, we obtain the component b_2 by computing ${\lambda_2}^{\mu'} {\lambda_2}^{\mu'} g_{\mu'\nu'} = b_2^2 \; g_{\theta'\theta'} = 1$. It follows that $b_2 = 1/r$ and ${\lambda_2}^{\mu'}$ is orthogonal to ${\lambda_0}^{\mu'}$ and ${\lambda_2}^{\mu'}$ can be shown to satisfy the parallel transport condition. We next construct two vectors, ${\tilde{\lambda}_1}{}^{\mu'}$ and ${\tilde{\lambda}_3}{}^{\mu'}$ that make an orthonormal set with ${\lambda_0}^{\mu'}$ and ${\lambda_2}^{\mu'}$. Define ${\tilde{\lambda}_1}{}^{\mu'} = (c_0, c_1, 0, 0)$ and using the orthonormality conditions we find that $c_0 = u^r r/(f\sqrt{r^2+L^2})$ and $c_1 = rE/\sqrt{r^2+L^2}$. Similarly, we form ${\tilde{\lambda}_3}{}^{\mu'} = (d_0, d_1, 0, d_2)$ and find that $d_0 = \pm EL/(f\sqrt{r^2+L^2})$, $d_1 = \pm u^r L/\sqrt{r^2+L^2}$, $d_3 = \pm\sqrt{(r^2+L^2)}/r^2$. We choose the plus sign and arrive at the following orthonormal set,

$$
\begin{aligned}
{\lambda_0}^{\mu'} &= \left(\frac{E}{f}, u^r, 0, \frac{L}{r^2}\right), & {\tilde{\lambda}_1}{}^{\mu'} &= \left(\frac{u^r r}{f\sqrt{r^2+L^2}}, \frac{rE}{\sqrt{r^2+L^2}}, 0, 0\right), \\
{\lambda_2}^{\mu'} &= \left(0, 0, \frac{1}{r}, 0\right), & {\tilde{\lambda}_3}{}^{\mu'} &= \left(\frac{EL}{f\sqrt{r^2+L^2}}, \frac{u^r L}{\sqrt{r^2+L^2}}, 0, \frac{\sqrt{r^2+L^2}}{r^2}\right).
\end{aligned} \tag{3.3.11}
$$

While these vectors are orthonormal, it may be shown that ${\tilde{\lambda}_1}{}^{\mu'}$ and ${\tilde{\lambda}_3}{}^{\mu'}$ do not satisfy the parallel transport conditions for orbits on Schwarzschild. However, we can form two new vectors ${\lambda_1}^{\mu'}$ and ${\lambda_3}^{\mu'}$ through a purely spatial rotation,

$$
{\lambda_1}^{\mu'} = {\tilde{\lambda}_1}{}^{\mu'} \cos\Psi - {\tilde{\lambda}_3}{}^{\mu'} \sin\Psi, \qquad {\lambda_3}^{\mu'} = {\tilde{\lambda}_1}{}^{\mu'} \sin\Psi + {\tilde{\lambda}_3}{}^{\mu'} \cos\Psi, \tag{3.3.12}
$$

and seek to enforce the parallel transport conditions through an appropriate rate of frame precession given by some $\Psi(\tau)$. Consider the expression for ${\lambda_1}^{\mu'}$,

$$
{\lambda_1}^{\mu'} = \left(\frac{u^r r\cos\Psi - EL\sin\Psi}{f\sqrt{r^2+L^2}}, \frac{rE\cos\Psi - u^r L\sin\Psi}{\sqrt{r^2+L^2}}, 0, -\frac{\sqrt{r^2+L^2}}{r^2}\sin\Psi\right). \tag{3.3.13}
$$

We obtain an expression for Ψ by substituting ${\lambda_1}^{\mu'}$ into the parallel transport equation (3.3.10). By considering the ϕ'-component of the equation, the rotation angle is found, in a straightforward manner, to satisfy the differential equation,

$$
\frac{d\Psi}{d\tau} = \frac{EL}{r^2+L^2}. \tag{3.3.14}
$$

Thus, $\boldsymbol{\lambda}_a = (\boldsymbol{\lambda}_0, \boldsymbol{\lambda}_1, \boldsymbol{\lambda}_2, \boldsymbol{\lambda}_3)$ are an orthonormal set of vectors that are parallel transported along a parabolic geodesic in the Schwarzschild spacetime.

3.4 Construction of the Riemann tensor in FNC system and tidal tensor definitions

In this section, we give the components of the Riemann tensor relevant to calculating the tidal field in the FNC system. We use the formalism of Marck (1983) and Ishii et al. (2005) [60, 58].

3.4.1 Riemann tensor in the FNC system

Using the Fermi normal frame derived in the previous section, we may project the Riemann tensor and its covariant derivatives, as given in Schwarzschild coordinates, to the form given in Fermi normal coordinates,

$$R_{abcd} = R_{\mu'\alpha'\nu'\beta'}\, \lambda_a{}^{\mu'}\, \lambda_b{}^{\alpha'}\, \lambda_c{}^{\nu'}\, \lambda_d{}^{\beta'}, \tag{3.4.1}$$

$$R_{abcd;e} = R_{\mu'\alpha'\nu'\beta';\rho'}\, \lambda_a{}^{\mu'}\, \lambda_b{}^{\alpha'}\, \lambda_c{}^{\nu'}\, \lambda_d{}^{\beta'}\, \lambda_e{}^{\rho'}, \tag{3.4.2}$$

$$R_{abcd;ef} = R_{\mu'\alpha'\nu'\beta';\rho'\sigma'}\, \lambda_a{}^{\mu'}\, \lambda_b{}^{\alpha'}\, \lambda_c{}^{\nu'}\, \lambda_d{}^{\beta'}\, \lambda_e{}^{\rho'}\, \lambda_f{}^{\sigma'}. \tag{3.4.3}$$

In the formalism of Marck (1983) and Ishii et al. (2005), the Riemann tensor is first transformed into the standard tetrad by (3.2.13) and then transformed to the FNC frame by

$$R_{abcd} = R_{(a)(b)(c)(d)}\Lambda_a{}^{(a)}\Lambda_b{}^{(b)}\Lambda_c{}^{(c)}\Lambda_d{}^{(d)}. \tag{3.4.4}$$

The transformation matrix $\Lambda_a{}^{(a)}$ that accomplishes this second step is related to the standard tetrad and the FNC tetrad $\boldsymbol{\lambda}_a$ by [58]

$$\lambda_a{}^{\mu'} = \Lambda_a{}^{(a)} e_{(a)}{}^{\mu'}, \qquad \Lambda_a{}^{(a)} = \lambda_a{}^{\mu'} e^{(a)}{}_{\mu'} \tag{3.4.5}$$

and its components are given by [60, 58]

$$
\begin{aligned}
&{\Lambda_0}^{(0)} = f^{-1/2}, && {\Lambda_0}^{(1)} = f^{-1/2}\dot{r}, \\
&{\Lambda_0}^{(2)} = 0 && {\Lambda_0}^{(3)} = \frac{L}{r}, \\
&{\Lambda_1}^{(0)} = \frac{r\dot{r}\cos\Psi - L\sin\Psi}{[f(r^2+L^2)]^{1/2}}, && {\Lambda_1}^{(1)} = \frac{r\cos\Psi - L\dot{r}\sin\Psi}{[f(r^2+L^2)]^{1/2}}, \\
&{\Lambda_1}^{(2)} = 0, && {\Lambda_1}^{(3)} = -(r^2+L^2)^{1/2}\sin\Psi/r, \\
&{\Lambda_2}^{(0)} = 0, && {\Lambda_2}^{(1)} = 0, \\
&{\Lambda_2}^{(2)} = 1, && {\Lambda_2}^{(3)} = 0, \\
&{\Lambda_3}^{(0)} = \frac{L\cos\Psi + r\dot{r}\sin\Psi}{[f(r^2+L^2)]^{1/2}}, && {\Lambda_3}^{(1)} = \frac{L\dot{r}\cos\Psi + r\sin\Psi}{[f(r^2+L^2)]^{1/2}}, \\
&{\Lambda_3}^{(2)} = 0, && {\Lambda_3}^{(3)} = \sqrt{(r^2+L^2)}\cos\Psi/r,
\end{aligned} \tag{3.4.6}
$$

with time-dependent rotation angle given previously (3.3.14). Calculating the components in the Fermi normal coordinate frame in this manner is equivalent to performing only one transformation using ${\lambda_a}^{\mu'}$ and we have verified these results.

We define the following tidal tensors using the standard notation of [58]

$$C_{ij} = R_{0i0j}, \quad C_{ijk} = R_{0(i|0|j;k)}, \quad C_{ijkl} = R_{0(i|0|j;kl)}, \quad B_{ijk} = R_{k(ij)0}, \quad A_k = \frac{2}{3}B_{ijk}x^i x^j, \tag{3.4.7}$$

where A_k is the gravitomagnetic potential and x^i are the coordinates in the FNC frame. The metric can be re-expressed in terms of these tidal tensors, as in (3.1.6), as

$$
\begin{aligned}
g_{00} &= -1 - C_{ij}x^i x^j - \frac{1}{3}C_{ijk}x^i x^j x^k - \frac{1}{12}\left(C_{ijkl} + 4C_{(ij}C_{kl)} - 4B_{(kl|n|}B_{ij)n}\right)x^i x^j x^k x^l + \cdots \\
g_{0m} &= \frac{2}{3}B_{ijm}x^i x^j + \frac{1}{4}R_{m(ij|0|;k)}x^i x^j x^k \\
&\quad + \frac{1}{135}\left(9R_{m(ij|0|;kl)} - 6{R_{m(ij}}^{0}R_{|0|kl)0} - 2{R_{m(ij}}^{n}R_{|n|kl)0}\right)x^i x^j x^k x^l \cdots \\
g_{mn} &= \delta_{mn} + \frac{1}{6}\left(R_{imnj} + R_{inmj}\right)x^i x^j \\
&\quad - \frac{1}{36}\left(R_{injm;k} + R_{inkm;j} + R_{jnim;k} + R_{knim;j} + R_{knjm;i} + R_{jnkm;i}\right)x^i x^j x^k \\
&\quad + \frac{1}{180}\left(9R_{m(ij|n|;kl)} - 6{R_{m(ij}}^{0}R_{|n|kl)0} - 2{R_{m(ij}}^{p}R_{|n|kl)p}\right)x^i x^j x^k x^l.
\end{aligned} \tag{3.4.8}
$$

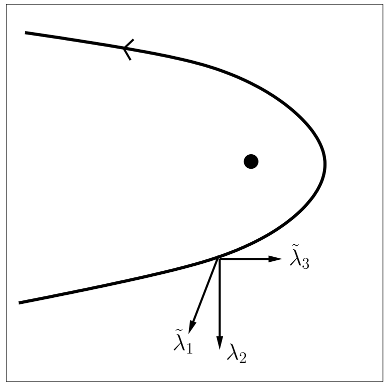

Figure 3.3: The spatial vectors of the rotated Fermi normal coordinate frame. The set $\{\tilde{\lambda}_1{}^{\mu'}, \lambda_2{}^{\mu'}, \tilde{\lambda}_3{}^{\mu'}\}$ is not parallel-propagated along the geodesic. To construct the Fermi normal frame, an inverse rotation Ψ of $\tilde{\lambda}_1{}^{\mu'}$ and $\tilde{\lambda}_3{}^{\mu'}$ must be performed in the orbital plane to obtain the parallel-propagated vectors $\lambda_1{}^{\mu'}$ and $\lambda_3{}^{\mu'}$.

3.4.2 Explicit components of the tidal tensors

The Riemann tensor and its covariant derivatives can be expressed as components either in the FNC frame $\{\boldsymbol{\lambda}_0, \boldsymbol{\lambda_1}, \boldsymbol{\lambda}_2, \boldsymbol{\lambda_3}\}$ or in the tilde frame $\{\boldsymbol{\lambda}_0, \tilde{\boldsymbol{\lambda}}_{\boldsymbol{1}}, \boldsymbol{\lambda}_2, \tilde{\boldsymbol{\lambda}}_{\boldsymbol{3}}\}$. The same statement holds for the tidal tensors, which can be denoted by C_{ij}, C_{ijk}, C_{ijkl}, and B_{ijk} in the FNC frame and as $\tilde{C}_{ij}$, $\tilde{C}_{ijk}$, $\tilde{C}_{ijkl}$, and $\tilde{B}_{ijk}$ in the tilde frame. While the tilde frame is not parallel-propagated, it does provide a simpler form for the tidal tensor components. Figure 3.3 shows the direction of the vectors of the tilde frame along a parabolic trajectory. The coordinates in the tilde frame may be written in terms of the FNC coordinates by

$$\tilde{x}_1 = x_1 \cos\Psi + x_3 \sin\Psi, \qquad \tilde{x}_2 = x_2, \qquad \tilde{x}_3 = -x_1 \sin\Psi + x_3 \cos\Psi. \tag{3.4.9}$$

The coordinates in the FNC frame may be associated with alternative Cartesian coordinates by the transformation: $x_1 = x, x_3 = y, x_2 = -z$. The quadrupole and octupole tidal tensors for a parabolic geodesic are as follows. The non-zero components of the quadrupole tidal tensor in the tilde frame are

$$\tilde{C}_{ij} = \mathrm{diag}(\tilde{C}_{11}, \tilde{C}_{22}, \tilde{C}_{33}) = \mathrm{diag}\left[-\frac{M\left(3L^2+2r^2\right)}{r^5}, \frac{M\left(3L^2+r^2\right)}{r^5}, \frac{M}{r^3}\right]. \tag{3.4.10}$$

In contrast, the non-zero components of the quadrupole tidal tensor in the FNC frame are

$$\begin{pmatrix} \frac{M}{r^3}\left[1-\frac{3(L^2+r^2)}{r^2}\cos^2\Psi\right] & 0 & -\frac{M}{r^3}\frac{3(L^2+r^2)}{r^2}\sin\Psi\cos\Psi \\ 0 & \frac{M}{r^3}\left(1+\frac{3L^2}{r^2}\right) & 0 \\ -\frac{M}{r^3}\frac{3(L^2+r^2)}{r^2}\sin\Psi\cos\Psi & 0 & \frac{M}{r^3}\left[1-\frac{3(L^2+r^2)}{r^2}\sin^2\Psi\right] \end{pmatrix} \tag{3.4.11}$$

Likewise, the non-zero components of the octupole tidal tensor are simpler in the tilde frame,

$$\begin{aligned}
\tilde{C}_{111} &= \frac{6M}{r^4}\left(1+\frac{3L^2}{2r^2}\right)V_2^{-1} \\
\tilde{C}_{131} &= \tilde{C}_{311} = \tilde{C}_{113} = \frac{4M}{r^4}\frac{L}{r}u^r\left(1+\frac{5L^2}{4r^2}\right)V_2^{-1} \\
\tilde{C}_{122} &= \tilde{C}_{212} = \tilde{C}_{221} = -\frac{3M}{r^4}\left(1+\frac{7L^2}{3r^2}\right)V_2^{-1} \\
\tilde{C}_{133} &= \tilde{C}_{313} = \tilde{C}_{331} = -\frac{3M}{r^4}\left(1+\frac{2L^2}{3r^2}\right)V_2^{-1} \\
\tilde{C}_{322} &= \tilde{C}_{232} = \tilde{C}_{223} = -\frac{M}{r^4}\frac{L}{r}u^r\left(1+\frac{5L^2}{r^2}\right)V_2^{-1} \\
\tilde{C}_{333} &= -\frac{3M}{r^4}\frac{L}{r}u^r V_2^{-1}
\end{aligned} \tag{3.4.12}$$

where $V_2 = \sqrt{1 + L^2/r^2}$. Again, the non-zero components of the octupole tidal tensor in the FNC frame are more complicated and found to be,

$$
\begin{aligned}
C_{111} &= \frac{3M}{4r^4}\Big[3\left(1 + \frac{7L^2}{3r^2}\right)\cos\Psi + 5\left(1 + \frac{L^2}{r^2}\right)\cos(3\Psi) \\
&- 6\frac{L}{r}u^r\left(1 + \frac{5L^2}{3r^2}\right)\sin\Psi - 10\frac{L}{r}u^r\left(1 + \frac{L^2}{r^2}\right)\cos(2\Psi)\sin\Psi\Big]V_2^{-1} \\
C_{131} &= C_{311} = C_{113} = \frac{M}{4r^4}\Big[\frac{L}{r}u^r\left(1 + \frac{5L^2}{r^2}\right)\cos\Psi + 15\frac{L}{r}u^r\left(1 + \frac{L^2}{r^2}\right)\cos(3\Psi) \\
&+ 18\left(1 + \frac{11L^2}{9r^2}\right)\sin\Psi + 30\left(1 + \frac{L^2}{r^2}\right)\cos(2\Psi)\sin\Psi\Big]V_2^{-1} \\
C_{122} &= \frac{M}{r^4}\Big[-3\left(1 + \frac{7L^2}{3r^2}\right)\cos\Psi + \frac{L}{r}u^r\left(1 + \frac{5L^2}{r^2}\right)\sin\Psi\Big]V_2^{-1} \\
C_{133} &= \frac{M}{4r^4}\Big[3\left(1 + \frac{7L^2}{3r^2}\right)\cos\Psi - 15\left(1 + \frac{L^2}{r^2}\right)\cos(3\Psi) \\
&+ 14\frac{L}{r}u^r\left(1 + \frac{5L^2}{7r^2}\right)\sin\Psi + 30\frac{L}{r}u^r\left(1 + \frac{L^2}{r^2}\right)\cos(2\Psi)\sin\Psi\Big]V_2^{-1} \\
C_{322} &= C_{232} = C_{223} = -\frac{M}{r^4}\Big[\frac{L}{r}u^r\left(1 + \frac{5L^2}{r^2}\right)\cos\Psi + 3\left(1 + \frac{7L^2}{3r^2}\right)\sin\Psi\Big]V_2^{-1} \\
C_{333} &= \frac{3M}{4r^4}\Big[\frac{L}{r}u^r\left(1 + \frac{5L^2}{r^2}\right)\cos\Psi - 5\frac{L}{r}u^r\left(1 + \frac{L^2}{r^2}\right)\cos(3\Psi) \\
&- 12\left(1 + \frac{2L^2}{3r^2}\right)\sin\Psi + 20\left(1 + \frac{L^2}{r^2}\right)\sin^3\Psi\Big]V_2^{-1}.
\end{aligned}
\tag{3.4.13}
$$

We have obtained the lengthy expressions for $\tilde{C}_{ijkl}$ and C_{ijkl} in Mathematica and have omitted reproducing them here for brevity. The non-zero components of B_{ijk} in the rotated frame are given by

$$
\tilde{B}_{131} = \tilde{B}_{311} = -\tilde{B}_{232} = -\tilde{B}_{322} = -\frac{1}{2}\tilde{B}_{113} = \frac{1}{2}\tilde{B}_{223} = -\frac{3LM\sqrt{L^2 + r^2}}{2r^5}. \tag{3.4.14}
$$

In the Fermi normal coordinate frame, they are

$$
\begin{aligned}
B_{113} &= -\frac{1}{2}B_{131} = -B_{223} = \frac{1}{2}B_{232} = -\frac{1}{2}B_{311} = \frac{1}{2}B_{322} = \frac{3LM\sqrt{L^2 + r^2}}{r^5}\cos\Psi \quad , \\
B_{122} &= -B_{133} = B_{212} = -2B_{221} = -B_{313} = 2B_{331} = -\frac{3LM\sqrt{L^2 + r^2}}{2r^5}\sin\Psi.
\end{aligned}
\tag{3.4.15}
$$

Finally, the gravitomagnetic potential is given as components in the FNC frame by

$$
\begin{aligned}
A_1 &= -\frac{2LM}{r^5}\sqrt{L^2 + r^2}\left\{x^1x^3\cos\Psi + \sin\Psi\left[(x^3)^2 - (x^2)^2\right]\right\} \\
A_2 &= \frac{2LM}{r^5}x^2\sqrt{L^2 + r^2}(x^3\cos\Psi - x^1\sin\Psi) \\
A_3 &= \frac{2LM}{r^5}\sqrt{L^2 + r^2}\left\{\cos\Psi\left[(x^1)^2 - (x^2)^2\right] + x^1x^3\sin\Psi\right\}.
\end{aligned}
\tag{3.4.16}
$$

3.5 Combined gravity of the star and the external tidal field

In this section we consider how the star's self-gravity and the black hole tidal field can be combined, using a post-Newtonian expansion to reach a common level of approximation. The tidal field is derived from the metric in FNC, which is suited to following test-body motion relative to the chosen central geodesic in a small neighborhood. If the mass of a fluid is negligible, then fluid motion in this small neighborhood may be computed also by simply using the tidal field. The equations for the fluid are derived by using the FNC metric expansion in the conservation law

$$T^{ab}{}_{;b} = 0 = T^{ab}{}_{,b} + \Gamma^{a}{}_{cb}T^{cb} + \Gamma^{b}{}_{cb}T^{ac}. \tag{3.5.1}$$

However, the star's mass is, in general, not negligible and we must account for its self-gravity. The form of the metric in (3.1.6) must be modified to account for both the gravity of the star and the black hole tidal field. However, since it is the case that simultaneously (1) the self-gravity of the star is weak and (2) the star never approaches too close to the horizon of the black hole (so that the tidal field is also sufficiently weak), then to first approximation the combined gravitational field can be taken as the linear superposition of the two fields. Note that since the Einstein field equations are nonlinear, this superposition will not yield a consistent solution. Instead, this field will represent a first-order solution in a perturbation calculation and at next order in iterating the Einstein field equations an interaction, or correction term, must emerge. These issues are discussed in more detail in this section where we consider how the self-gravity can be incorporated in the FNC approach and what represents an adequate approximation for the gravitational field.

3.5.1 Physical scales associated with tidal encounters and dimensionless parameters

Consider a parabolic encounter with a pericentric radius R_p. Let the mass of the black hole be M. In the weak-field and slow motion limit, the $C_{ij} = R_{0i0j}$ term in g_{00} of (3.1.6) is dynamically the most significant. We may write the typical magnitude of this term as

$$|R_{0i0j}x^i x^j| \sim \mathcal{O}\left(\frac{M}{R_p^3}\mathcal{L}^2\right), \tag{3.5.2}$$

where $\mathcal{L}$ is the characteristic size of a region of interest following motion on the world line $\mathcal{G}$. The weakness of the black hole tidal field may be characterized by

$$\frac{M}{R(t)} \lesssim \frac{M}{R_p} \equiv \delta^2 \ll 1, \tag{3.5.3}$$

which will hold for distant encounters. Furthermore, we will also assume that the domain for our calculations (and hence the star) is small compared to the distance to the black hole so that

$$\nu \equiv \frac{\mathcal{L}}{R_p} \ll 1. \tag{3.5.4}$$

This requirement will be discussed further below. We see that the dominant tidal term is a leading term in a simultaneous expansion in the small parameters δ and ν. At the same time, a star of mass M_* and radius R_* can be assumed to have a weak gravitational field in its interior and near environment such that

$$|h_{00}| = |g_{00} + 1| \lesssim \epsilon^2 \equiv \frac{M_*}{R_*}. \tag{3.5.5}$$

If we assume that the tidal field and self-gravitational field can be added linearly, then these two contributions will be of comparable strength (if we take $\mathcal{L} \simeq R_*$) when a star is on the threshold of tidal disruption. (In what follows we will restrict our attention to computational domains of size $\mathcal{L}$ that are at most a few times R_*, and henceforth simply define $\mathcal{L} = R_*$.) The balance of these terms occurs when the previously defined tidal disruption parameter

$$\eta \equiv \left(\frac{R_p^3}{M} \frac{M_*}{R_*} \right)^{1/2}, \tag{3.5.6}$$

is $\eta \simeq 1$. In this thesis, we will consider tidal encounters that are at the threshold of disruption ($\eta = 1$) or weaker ($\eta \sim 2 - 6$). In both cases, we will consider η to be of order unity for the sake of this discussion.

We use $\epsilon^2 \ll 1$ as the post-Newtonian expansion parameter for the weak field and slow motion in the star's near zone. Simultaneously, we use $\delta^2 \ll 1$ as the orbital post-Newtonian expansion parameter for the maximum strength of the encounter (before disruption), which is also weak. In general, these two parameters may not be of the same order of magnitude. They are related by the binary mass ratio, $\mu \equiv M_*/M$. In this study, we consider this mass ratio to be small, $\mu \ll 1$, and confine our interest to the range $\mu = 10^{-5} - 10^{-3}$. This corresponds to black holes with masses in the range $M = 10^3 - 10^5 M_\odot$. In terms of the encounter strength η, the stellar and orbital post-Newtonian parameters are related by

$$\delta^2 = \epsilon^2 \mu^{-2/3} \eta^{-2/3}. \tag{3.5.7}$$

We see that for small mass ratios, the orbital velocity in the black hole frame, $\sim \delta$, may be much larger than the sound speed within the star, $\sim \epsilon$. This difference in the strengths of the black hole field and the internal field of the star is related to the difference between the size of the star, R_*, and the inhomogeneity scale, $R(t) \gtrsim R_p$. We have that

$$\frac{R_*}{R_p} = \nu = \mu^{1/3} \eta^{-2/3}, \tag{3.5.8}$$

and see that we will also have $\nu \ll 1$.

3.5.2 Superposition of the fields and an approximation for white dwarfs

The metric for the tidal field (3.4.8) is a simultaneous power series expansion in the size of the region, $\nu = R_*/R_p$, and the black hole field strength at periastron, $\delta^2 = M/R_p$. Schematically, the expansion can be written as a double sum,

$$\begin{aligned}
g_{00} &= -1 + \sum_{m=2}^{\infty} \sum_{n=0} g_{00}^{[n,m]} \left(\frac{M}{R_p}\right) \left(\frac{M}{R_p}\right)^n \left(\frac{R_*}{R_p}\right)^m, \\
g_{0i} &= \sum_{m=2}^{\infty} \sum_{n=0} g_{0i}^{[n,m]} \left(\frac{M}{R_p}\right)^{3/2} \left(\frac{M}{R_p}\right)^n \left(\frac{R_*}{R_p}\right)^m, \\
g_{ij} &= \delta_{ij} + \sum_{m=2}^{\infty} \sum_{n=0} g_{ij}^{[n,m]} \left(\frac{M}{R_p}\right) \left(\frac{M}{R_p}\right)^n \left(\frac{R_*}{R_p}\right)^m,
\end{aligned} \tag{3.5.9}$$

over tidal multipoles, m, and orbital post-Newtonian corrections, n, though not all powers of δ^2 will be present.

In contrast, if we consider an isolated star (e.g., a white dwarf), the gravitational field represented in a post-Newtonian expansion in powers of ϵ will have terms of the following sizes [56],

$$
\begin{aligned}
g_{00} &= -1 - 2\Phi_* + \mathcal{O}\left[\left(\frac{M_*}{R_*}\right)^2\right] + \cdots\,, \\
g_{0i} &= \mathcal{O}\left[\left(\frac{M_*}{R_*}\right)^{3/2}\right] + \cdots\,, \\
g_{ij} &= \delta_{ij} + \mathcal{O}\left(\frac{M_*}{R_*}\right) + \cdots\,.
\end{aligned} \tag{3.5.10}
$$

Here, the Newtonian potential Φ_* is displayed and the next order terms in each metric component are the first post-Newtonian. While not explicitly displayed here, their form for a fluid configuration is well known [64]. The strength of the gravitational field for a typical field white dwarf ($M_{\rm wd} \simeq 0.6 M_\odot$) is $\epsilon^2 \simeq 10^{-4}$, and so the stellar 1-PN corrections are of size 10^{-4} smaller than the Newtonian potential.

In this thesis we consider the Newtonian self-gravitational field of the star and Newtonian hydrodynamics as an adequate treatment for our purposes. This introduces fractional errors on the order of 10^{-4}. Using this assumption, we consider the superposition of the tidal field and self-gravitational field while retaining all necessary terms without making errors larger than those already made by neglecting the (stellar) 1-PN corrections. A set of relativistic corrections in the tidal field are retained because the small mass ratio μ yields a difference between orbital PN parameter δ and stellar PN parameter ϵ, with typically $\delta \gg \epsilon$.

For a star in an external tidal field, we cannot simply add the stellar gravitational field to the tidal field because the Einstein field equations are nonlinear. However, if both the stellar field and the tidal field are weak, the combined field can be taken to be the superposition plus a (higher order) interaction expansion [65]. The form of the combined fields is

$$
\begin{aligned}
g_{00} &= -1 - 2\Phi_* + h_{00}^{\rm tidal} + h_{00}^{\rm int} + \mathcal{O}\left(\frac{M_*^2}{R_*^2}\right), \\
g_{0i} &= h_{0i}^{\rm tidal} + h_{0i}^{\rm int} + \mathcal{O}\left[\left(\frac{M_*}{R_*}\right)^{3/2}\right], \\
g_{ij} &= \delta_{ij} + h_{ij}^{\rm tidal} + h_{ij}^{int} + \mathcal{O}\left(\frac{M_*}{R_*}\right),
\end{aligned} \tag{3.5.11}
$$

where the $h_{\mu\nu}^{\rm int}$ is the interaction field. The interaction terms arise from the nonlinearity of the

Einstein field equations. We expect the term $h_{00}^{\rm int}$ in g_{00} to be of order

$$h_{00}^{\rm int} \sim \Phi_* h_{00}^{\rm tidal} \sim \mathcal{O}\left(\frac{M_*}{R_*}\frac{M_*}{R_*}\eta^{-2}\right). \tag{3.5.12}$$

Since we consider $\eta \equiv \mathcal{O}(1)$ for this discussion, then $h_{00}^{\rm int} \sim \mathcal{O}(\epsilon^4)$ and it is at the level of already neglected (stellar) 1-PN corrections. Likewise, the interaction terms in g_{0i} and g_{ij} can be no larger than the respective neglected (stellar) 1-PN corrections. Thus, we are able to neglect the nonlinear interaction field as long as we neglect the first post-Newtonian corrections to the star's internal gravity and hydrodynamics. We therefore superimpose linearly the Newtonian self-gravitational field and the tidal field expressed previously in the FNC system. We set the cutoff of terms in the FNC tidal field to be those that are in order of magnitude size at or below the terms we have already neglected.

We now show that some parts of the metric in (3.5.11) can be ignored and that some of the terms we retain represent interesting (orbital) relativistic corrections. In Figure 3.4, we show schematically the relevant acceleration terms which correspond to the terms in the expansion of the metric. This is given for the range in mass ratio $\mu = 10^{-5} - 10^{-3}$. Any terms less than (stellar) 1-PN and the motion of the black hole are negligible.

Consider the tidal terms in the g_{00} expansion. The quadrupole tidal term (3.4.11) has a Newtonian term and a δ^2 correction,

$$\begin{aligned} C_{ij}x^i x^j = {} & \mathcal{O}\left(\frac{M}{R_p}\frac{R_*^2}{R_p^2}\right) \quad \& \quad \mathcal{O}\left(\frac{M}{R_p}\frac{M}{R_p}\frac{R_*^2}{R_p^2}\right) \\ = {} & \mathcal{O}\left(\epsilon^2\eta^{-2}\right) \quad \& \quad \mathcal{O}\left(\epsilon^4\mu^{-2/3}\eta^{-8/3}\right). \end{aligned} \tag{3.5.13}$$

We see that the first term (denoted as $\alpha_{l=2}^{0PN}$) is the same size as the Newtonian stellar potential. For mass ratios $\mu \lesssim 10^{-3}$, the post-Newtonian correction (denoted as $\alpha_{l=2}^{1PN}$) is several orders of magnitude larger than (stellar) 1-PN ($\epsilon^4 \sim 10^{-8}$) and is therefore an important term. The octupole tidal term (3.4.13) has a Newtonian term, and δ^2 and δ^4 corrections,

$$\begin{aligned} C_{ijk}x^i x^j x^k = {} & \mathcal{O}\left(\frac{M}{R_p}\frac{R_*^3}{R_p^3}\right) \quad \& \quad \mathcal{O}\left(\frac{M}{R_p}\frac{M}{R_p}\frac{R_*^3}{R_p^3}\right) \quad \& \quad \mathcal{O}\left(\frac{M}{R_p}\frac{M^2}{R_p^2}\frac{R_*^3}{R_p^3}\right) \\ = {} & \mathcal{O}\left(\epsilon^2\mu^{1/3}\eta^{-8/3}\right) \quad \& \quad \mathcal{O}\left(\epsilon^4\mu^{-1/3}\eta^{-10/3}\right) \quad \& \quad \mathcal{O}\left(\epsilon^6\mu^{-1}\eta^{-4}\right). \end{aligned} \tag{3.5.14}$$

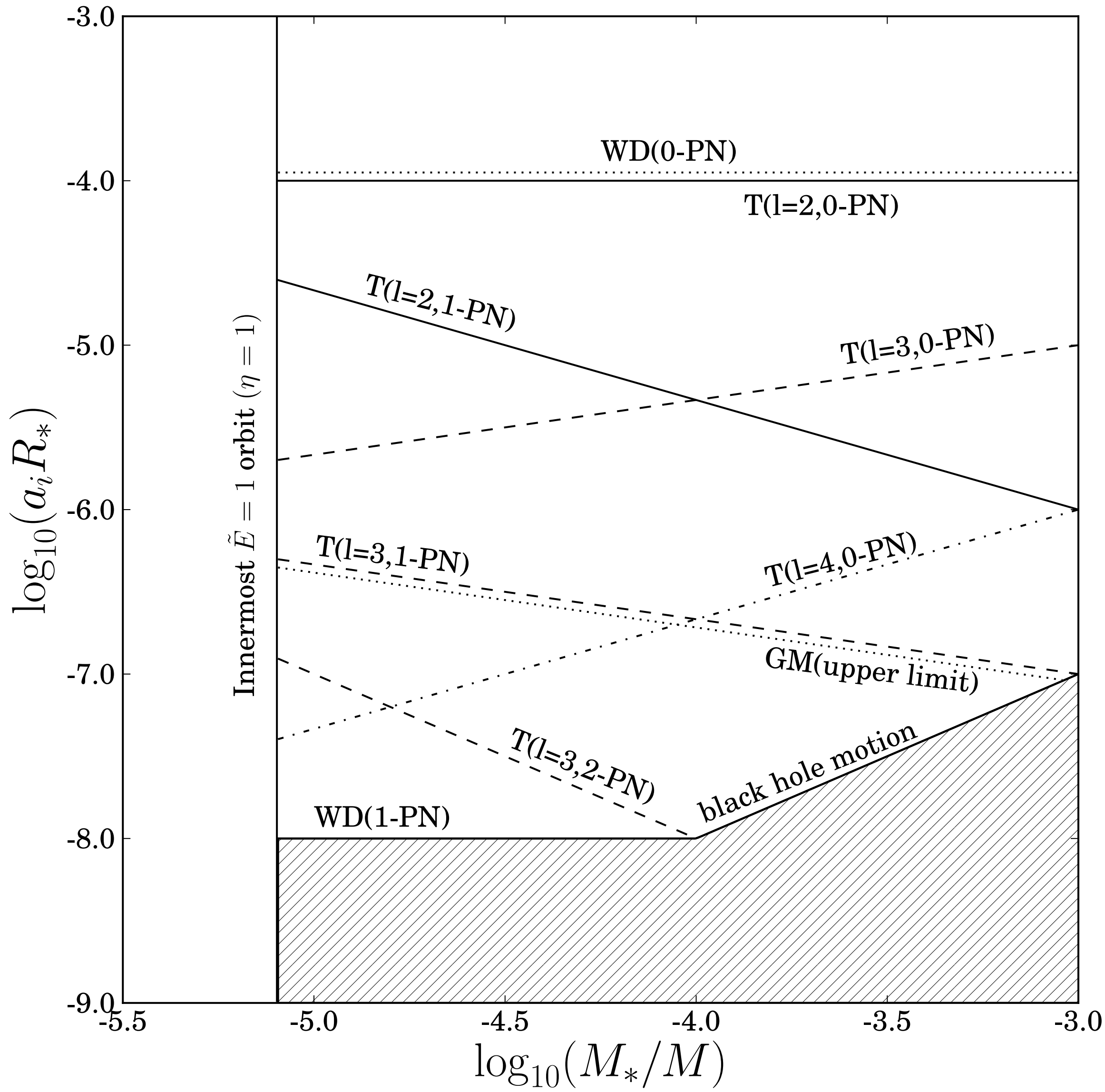

Figure 3.4: Acceleration terms in the metric of combined self- and tidal gravity fields. The formalism for calculating the relativistic tidal interaction in Fermi normal coordinates allows the addition of an arbitrary number of terms in the tidal expansion. However, the use of Newtonian hydrodynamics and self-gravity [WD (0PN)] limits the number. The diagram above gives the number of relevant post-Newtonian terms [T (l=2,0-PN), T (l=2,1-PN), ...] in the tidal expansion. Any accelerations multiplied by the radius of the star that are smaller than that of (stellar) 1PN and the motion of the black hole are negligible.

We see that the first term (denoted as $\alpha_{l=3}^{0PN}$) is one or two orders of magnitude smaller than the Newtonian stellar potential. The first (denoted as $\alpha_{l=3}^{1PN}$) and second (denoted as $\alpha_{l=3}^{2PN}$) post-Newtonian corrections are larger than (stellar) 1-PN for mass ratios of $\mu \lesssim 10^{-3}$ and $\mu \lesssim 10^{-4}$. The $l = 4$ has a Newtonian term and several δ corrections,

$$\begin{aligned} R_{0(i|0|j;kl)}x^i x^j x^k x^l &= \mathcal{O}\left(\frac{M}{R_p}\frac{R_*^4}{R_p^4}\right) \quad \& \quad \mathcal{O}\left(\frac{M}{R_p}\frac{M}{R_p}\frac{R_*^4}{R_p^4}\right) \quad \& \quad \cdots \\ &= \mathcal{O}\left(\epsilon^2\mu^{2/3}\eta^{-10/3}\right) \quad \& \quad \mathcal{O}\left(\epsilon^4\eta^{-4}\right) \quad \& \quad \cdots . \end{aligned} \tag{3.5.15}$$

The first term (denoted as $\alpha_{l=4}^{0PN}$) is significant for mass ratios $\mu > 10^{-6}$. The post-Newtonian correction is too small. The next term in the tidal expansion of g_{00} is

$$\begin{aligned} C_{(ij}C_{kl)}x^i x^j x^k x^l &= \mathcal{O}\left(\frac{M^2}{R_p^2}\frac{R_*^4}{R_p^4}\right) \quad \& \quad \cdots \\ &= \mathcal{O}\left(\epsilon^4\eta^{-4}\right) \quad \& \quad \cdots , \end{aligned} \tag{3.5.16}$$

and is at the cutoff and is too small to retain. The next term is

$$\begin{aligned} B_{(kl|n|}B_{ij)n}x^i x^j x^k x^l &= \mathcal{O}\left(\frac{M^2}{R_p^2}\frac{M}{R_p}\frac{R_*^4}{R_p^4}\right) \quad \& \quad \cdots \\ &= \mathcal{O}\left(\epsilon^6\mu^{1/3}\eta^{-2/3}\right) \quad \& \quad \cdots , \end{aligned} \tag{3.5.17}$$

and is also too small. The significance of g_{00} metric terms for different mass ratio can be seen in the corresponding acceleration terms in Figure 3.4. For the other components of the metric, g_{0i} and g_{ij}, we should consider the acceleration terms directly and we address this in the next section.

3.5.3 Fluid equations of motion

We now obtain the fluid equations of motion for a self-gravitating star in a relativistic tidal field. We use the relevant terms in the tidal expansion of the metric with the limit at stellar 1-PN. For a perfect fluid, the stress-energy tensor is given by

$$T^{ab} = (\rho + \rho\epsilon + p)u^a u^b + pg^{ab}, \tag{3.5.18}$$

where the rest (baryon) energy density is ρ and the specific energy is ε. We define the spatial velocity in terms of the four-velocity components as $v^i \equiv dx^i/dt = u^i/u^0$ where $u^0 = dt/d\tau$ and $u^i = dx^i/d\tau$.

Writing out the components of the stress-energy tensor,

$$
\begin{aligned}
T^{00} &= \rho\left(1+\varepsilon+\frac{p}{\rho}\right)(u^0)^2 + pg^{00}, \\
T^{i0} &= \rho\left(1+\varepsilon+\frac{p}{\rho}\right)(u^0)^2 v^i, \\
T^{ij} &= \rho\left(1+\varepsilon+\frac{p}{\rho}\right)(u^0)^2 v^i v^j + pg^{ij},
\end{aligned}
\tag{3.5.19}
$$

where the specific internal energy ε is approximately the same order as the stellar potential, $\varepsilon \sim p/\rho \sim \Phi_* \sim \epsilon^2$. Expanding the velocity constraint, $u_a u^a = -1 = g_{ab}u^a u^b = g_{00}(u^0)^2 + 2g_{0i}(u^0)^2 v^i + g_{ij}(u^0)^2 v^i v^j$. Then, $(u^0)^2 = 1 + v^2 + 2({}_2h_{00})$, where ${}_2h_{00}$ denotes the terms in the metric expansion of order $\mathcal{O}\left(\epsilon^2\right)$. In our calculations we consider Newtonian hydrodynamics. We have that the stress-energy tensor at the stellar 1-PN cutoff is

$$
\begin{aligned}
T^{00} &= \rho + \mathcal{O}(\rho\varepsilon) \\
T^{i0} &= \rho v^i + \mathcal{O}(\rho\varepsilon^3) \\
T^{ij} &= \rho v^i v^j + \delta^{ij} p + \mathcal{O}(\rho\varepsilon^4).
\end{aligned}
\tag{3.5.20}
$$

Consider the $b = i$ case of the conservation equation (momentum equation),

$$
T^{ia}{}_{;a} = T^{ia}{}_{,a} + \Gamma^i{}_{ba}T^{ba} + \Gamma^a{}_{ab}T^{ib} = 0. \tag{3.5.21}
$$

The connection coefficients written in terms of the combined metric for the self-gravity and the tidal gravity are,

$$
\begin{aligned}
\Gamma^i{}_{00} &= \tfrac{1}{2} g^{i\nu}(g_{0\nu,0} + g_{0\nu,0} - g_{00,\nu}) \\
&= -\tfrac{1}{2}\ {}_2h_{00,i} - \tfrac{1}{2}\ {}_4h_{00,i} - \tfrac{1}{2}\ {}_6h_{00,i} +\ {}_3h_{0i,0} - \tfrac{1}{2}\ {}_2h_{ij}\ {}_2h_{00,j}, \\
\Gamma^i{}_{0j} &= \tfrac{1}{2} g^{i\nu}(g_{0\nu,j} + g_{j\nu,0} - g_{0j,\nu}) = \tfrac{1}{2}(\ {}_3h_{0i,j} +\ {}_2h_{ij,0} -\ {}_3h_{0j,i}), \\
\Gamma^i{}_{jk} &= \tfrac{1}{2} g^{i\nu}(g_{j\nu,k} + g_{k\nu,j} - g_{jk,\nu}) \\
&= \tfrac{1}{2}(\ {}_2h_{ij,k} +\ {}_4h_{ij,k} +\ {}_2h_{ik,j} +\ {}_4h_{ik,j} -\ {}_2h_{jk,i} -\ {}_4h_{jk,i}) \\
&\quad -\tfrac{1}{2}(\ {}_2h_{il}\ {}_2h_{jl,k} +\ {}_2h_{il}\ {}_2h_{kl,j} -\ {}_2h_{il}\ {}_2h_{jk,l}), \\
\Gamma^0{}_{00} &= \tfrac{1}{2} g^{0\nu}(g_{0\nu,0} + g_{0\nu,0} - g_{00,\nu}) \\
&= -\tfrac{1}{2}(\ {}_2h_{00,0} +\ {}_4h_{00,0} +\ {}_6h_{00,0}) - \tfrac{1}{2}\ {}_3h_{0i}\ {}_2h_{00,i} - \tfrac{1}{2}\ {}_2h_{00}\ {}_2h_{00,0} - \tfrac{1}{2}\ {}_3h_{0i}\ {}_2h_{00,i}, \\
\Gamma^0{}_{0i} &= \tfrac{1}{2} g^{0\nu}(g_{0\nu,i} + g_{i\nu,0} - g_{0i,\nu}) = -\tfrac{1}{2}(\ {}_2h_{00,i} +\ {}_4h_{00,i} +\ {}_6h_{00,i}) + \tfrac{1}{2}\ {}_2h_{00}\ {}_2h_{00,i}, \\
\Gamma^0{}_{ij} &= \tfrac{1}{2} g^{0\nu}(g_{i\nu,j} + g_{j\nu,i} - g_{ij,\nu}) = -\tfrac{1}{2}(\ {}_3h_{i0,j} +_3 h_{j0,i} -\ {}_2h_{ij,0}),
\end{aligned}
\tag{3.5.22}
$$

where ${}_Nh_{ab}$ denotes the terms in the combined metric expansion of the order $\mathcal{O}\left(\epsilon^N\right)$. Before substituting the components into the combined metric, consider the size of the g_{0i} and g_{ij} terms. The first term in g_{0i} is the gravitomagnetic term and we have that

$$
\begin{aligned}
B_{ijk}x^i x^j x^k = &\quad \mathcal{O}\left[\left(\frac{M}{R_p}\right)^{3/2} \frac{R_*^2}{R_p^2}\right] \quad \& \quad \mathcal{O}\left[\left(\frac{M}{R_p}\right)^{5/2} \frac{R_*^2}{R_p^2}\right] \quad \& \quad \cdots \\
= &\quad \mathcal{O}\left(\epsilon^3 \mu^{-1/3} \eta^{-7/3}\right) \quad \& \quad \mathcal{O}\left(\epsilon^5 \mu^{-1} \eta^{-3}\right) \quad \& \quad \cdots,
\end{aligned}
\tag{3.5.23}
$$

where the first part is (denoted $\alpha^1_{\rm GM}$) and the second term (denoted $\alpha^2_{\rm GM}$) is smaller by a factor of δ^2. The successsive terms in g_{0i} are smaller by a factor of R_*/R_p. We will show in the following that only the $\alpha^1_{\rm GM}$ term is significant. Consider the first term in g_{ij}

$$
\begin{aligned}
(R_{imnj} + R_{inmj})x^i x^j = &\quad \mathcal{O}\left(\frac{M}{R_p}\frac{R_*^2}{R_p^2}\right) \quad \& \quad \mathcal{O}\left(\frac{M^2}{R_p^2}\frac{R_*^2}{R_p^2}\right) \quad \& \quad \cdots \\
= &\quad \mathcal{O}\left(\epsilon^2 \eta^{-2}\right) \quad \& \quad \mathcal{O}\left(\epsilon^4 \mu^{-2/3} \eta^{-8/3}\right) \quad \& \quad \cdots.
\end{aligned}
\tag{3.5.24}
$$

We will show below that these two terms (denoted β^1 and β^2) and successive terms may be neglected.

Substituting the combined metric, we can re-express the connection coefficients in terms of orders,

$$
\begin{aligned}
\Gamma^{i}{}_{00} = \quad & \mathcal{O}\left(\alpha^{0PN}_{l=2}\ \frac{1}{\mathcal{L}}\right) \quad \& \quad \mathcal{O}\left(\alpha^{1PN}_{l=2}\ \frac{1}{\mathcal{L}}\right) \quad \& \quad \mathcal{O}\left(\alpha^{0PN}_{l=3}\ \frac{1}{\mathcal{L}}\right) \\
\& \quad & \mathcal{O}\left(\alpha^{1PN}_{l=3}\ \frac{1}{\mathcal{L}}\right) \quad \& \quad \mathcal{O}\left(\alpha^{2PN}_{l=3}\ \frac{1}{\mathcal{L}}\right) \quad \& \quad \mathcal{O}\left(\alpha^{0PN}_{l=4}\ \frac{1}{\mathcal{L}}\right) \\
\& \quad & \cdots \\
\Gamma^{i}{}_{0j} = \quad & \mathcal{O}\left(\alpha^{1}_{\mathrm{GM}}\ \frac{1}{\mathcal{L}}\right) \quad \& \quad \mathcal{O}\left(\beta^{1}\ \frac{\epsilon}{\mathcal{L}}\right) \quad \& \quad \cdots \\
\Gamma^{i}{}_{jk} = \quad & \mathcal{O}\left(\beta^{1}\ \frac{1}{\mathcal{L}}\right) \quad \& \quad \mathcal{O}\left(\beta^{2}\ \frac{1}{\mathcal{L}}\right) \quad \& \\
& \mathcal{O}\left((\beta^{1})^{2}\ \frac{1}{\mathcal{L}}\right) \quad \& \quad \cdots
\end{aligned}
$$

$$
\begin{aligned}
\Gamma^{0}{}_{00} = \quad & \mathcal{O}\left(\alpha^{0PN}_{l=2}\ \frac{\epsilon}{\mathcal{L}}\right) \quad \& \quad \mathcal{O}\left(\alpha^{0PN}_{l=3}\ \frac{\epsilon}{\mathcal{L}}\right) \quad \& \\
& \mathcal{O}\left(\alpha^{0PN}_{l=4}\ \frac{\epsilon}{\mathcal{L}}\right) \quad \& \quad \cdots \\
\Gamma^{0}{}_{0i} = \quad & \mathcal{O}\left(\alpha^{0PN}_{l=2}\ \frac{1}{\mathcal{L}}\right) \quad \& \quad \mathcal{O}\left(\alpha^{1PN}_{l=2}\ \frac{1}{\mathcal{L}}\right) \quad \& \quad \mathcal{O}\left(\alpha^{0PN}_{l=2}\ \frac{1}{\mathcal{L}}\right) \\
\& \quad & \mathcal{O}\left(\alpha^{1PN}_{l=2}\ \frac{1}{\mathcal{L}}\right) \quad \& \quad \mathcal{O}\left(\alpha^{0PN}_{l=3}\ \frac{1}{\mathcal{L}}\right) \quad \& \quad \mathcal{O}\left(\alpha^{1PN}_{l=3}\ \frac{1}{\mathcal{L}}\right) \\
\& \quad & \mathcal{O}\left(\alpha^{2PN}_{l=3}\ \frac{1}{\mathcal{L}}\right) \quad \& \quad \mathcal{O}\left(\alpha^{0PN}_{l=4}\ \frac{1}{\mathcal{L}}\right) \quad \& \quad \cdots \\
\Gamma^{0}{}_{ij} = \quad & \mathcal{O}\left(\alpha^{1}_{\mathrm{GM}}\ \frac{\epsilon}{\mathcal{L}}\right) \quad \& \quad \mathcal{O}\left(\beta^{1}\ \frac{\epsilon}{\mathcal{L}}\right) \quad \& \quad \cdots
\end{aligned}
\tag{3.5.25}
$$

The first term in the momentum equation (3.5.21) may be further expanded as,

$$
T^{ia}{}_{,a} = \quad (\rho v^{i}) \times \mathcal{O}\left(\frac{\epsilon}{\mathcal{L}}\right) \quad \& \quad \rho v^{i} v^{j} \times \mathcal{O}\left(\frac{1}{\mathcal{L}}\right) \quad \& \quad \delta^{ij} p \times \mathcal{O}\left(\frac{1}{\mathcal{L}}\right). \tag{3.5.26}
$$

For the next term,

$$
\Gamma^{i}{}_{ba} T^{ba} = \Gamma^{i}{}_{00} T^{00} + \Gamma^{i}{}_{0j} T^{0j} + \Gamma^{i}{}_{j0} T^{j0} + \Gamma^{i}{}_{jk} T^{jk}, \tag{3.5.27}
$$

we have for a cut-off at stellar 1-PN,

$$
\begin{aligned}
{\Gamma^i}_{ba}T^{ba} = \quad & \rho \times \mathcal{O}\left(\alpha^{0PN}_{l=2}\ \frac{1}{\mathcal{L}}\right) \quad \& \quad \rho \times \mathcal{O}\left(\alpha^{1PN}_{l=2}\ \frac{1}{\mathcal{L}}\right) \quad \& \\
& \rho \times \mathcal{O}\left(\alpha^{0PN}_{l=3}\ \frac{1}{\mathcal{L}}\right) \quad \& \quad \rho \times \mathcal{O}\left(\alpha^{1PN}_{l=3}\ \frac{1}{\mathcal{L}}\right) \quad \& \\
& \rho \times \mathcal{O}\left(\alpha^{2PN}_{l=3}\ \frac{1}{\mathcal{L}}\right) \quad \& \quad \rho \times \mathcal{O}\left(\alpha^{0PN}_{l=4}\ \frac{1}{\mathcal{L}}\right) \quad \& \\
& \rho v^i \times \mathcal{O}\left(\alpha^{1}_{\mathrm{GM}}\ \frac{1}{\mathcal{L}}\right).
\end{aligned}
$$

For the next term,

$$
{\Gamma^a}_{ab}T^{ib} = {\Gamma^0}_{00}T^{i0} + {\Gamma^0}_{0j}T^{ij} + {\Gamma^j}_{j0}T^{i0} + {\Gamma^j}_{jk}T^{ik}, \tag{3.5.28}
$$

we have for a cut-off at 1PN,

$$
\begin{aligned}
{\Gamma^a}_{ab}T^{ib} = \quad & \rho v^i \times \mathcal{O}\left(\alpha^{0PN}_{l=2}\ \frac{1}{\mathcal{L}}\right) \quad \& \quad \rho v^i \times \mathcal{O}\left(\alpha^{0PN}_{l=3}\ \frac{1}{\mathcal{L}}\right) \quad \& \\
& \rho v^i \times \mathcal{O}\left(\alpha^{0PN}_{l=4}\ \frac{1}{\mathcal{L}}\right) \quad \& \quad \rho v^i \times \mathcal{O}\left(\alpha^{1}_{\mathrm{GM}}\ \frac{1}{\mathcal{L}}\right)
\end{aligned}
$$

We have substituted the terms in the combined metric into the momentum equation and we see that there are several terms in the tidal expansion that are significant. We have Newtonian tidal terms for $l = 2, 3, 4$ that are relevant. Although we have a cut-off at stellar 1-PN, we have the following post-Newton terms: the first correction (1-PN) to $l = 2$, the second (1-PN) and third (2-PN) corrections to $l = 3$. We also have the gravitomagnetic term that is significant. Note that this corresponds with the acceleration terms in Figure 3.4.

Finally, the equations of motion of the fluid can be given in the approximation. We find that [58]

$$
\rho\frac{\partial v_i}{\partial \tau} + \rho v^j \frac{\partial v_i}{\partial x^j} = -\frac{\partial p}{\partial x^i} - \rho\frac{\partial}{\partial x^i}\left(\Phi_* + \Phi_{\mathrm{tidal}}\right) + \rho\left[v_j\left(\frac{\partial A_j}{\partial x^i} - \frac{\partial A_i}{\partial x^j}\right) - \frac{\partial A_i}{\partial \tau}\right], \tag{3.5.29}
$$

where Φ_* is the self-gravity potential and Φ_{tidal} is given by

$$
\Phi_{\mathrm{tidal}} = \tfrac{1}{2}C_{ij}x^ix^j + \tfrac{1}{6}C_{ijk}x^ix^jx^k + \tfrac{1}{24}\left[C_{ijkl} + 4C_{(ij}C_{kl)} - 4B_{(kl|n|}B_{ij)n}\right]x^ix^jx^kx^l + \mathcal{O}(x^5). \tag{3.5.30}
$$

In this chapter, we have introduced the coordinate frame for our calculations, Fermi normal coordinates. We have explicitly given the tidal tensors to calculate the tidal field. We have considered how the star's self-gravity and the black hole tidal field can be combined. By neglecting terms smaller than stellar 1-PN, we are able to ignore the interaction between the two fields and superpose them linearly. We have shown that there are several post-Newtonian terms in the tidal field that are relevant despite the fact that we consider only Newtonian hydrodynamics and stellar self-gravity for our calculations. We justified the various tidal terms used in the numerical method described in Chapter 4.

Chapter 4

Numerical method

In this chapter, we give the numerical method for calculating the tidal disruption of a star by a Schwarzschild black hole. We assume that the star is a Newtonian fluid and use the piecewise parabolic method with Lagrangian remap (PPMLR) to solve the hydrodynamic equations. We also assume that the self-gravity is Newtonian and solve Poisson's equation for the gravitational field of the star. We calculate the relativistic tidal interaction using a routine to update the location of the FNC frame along the geodesic using the hydrodynamic time as the proper time. From the location and proper time, we calculate the tidal accelerations due to the black hole using the formalism of Chapter 3.

4.1 Overview of the numerical method

The numerical method for calculating the tidal interaction between a black hole and a self-gravitating star consists of three modules. The main module is the hydrodynamics solver which evolves the density, pressure, and velocities of the fluid as it undergoes accelerations from pressure gradients, its own self-gravity, and the tidal interaction with the black hole. The self-gravity and tidal modules provide added acceleration terms incorporated into the hydrodynamics solver.

The simulated star evolves over hydrodynamic time, τ. We consider this to also be the proper time for the Fermi normal coordinate frame with origin assumed to be a point along the chosen geodesic. Using the proper time along the geodesic, we are able to obtain the location of the FNC frame from the black hole. We use this information to calculate the tidal accelerations.

4.2 PPMLR hydrodynamics

In this section, we present the numerical method for calculating the hydrodynamics of the fluid star. We begin with an overview of the Newtonian hydrodynamic equations. We give the relevant equations for our calculations and present the hydrodynamic solver for our numerical method.

4.2.1 Newtonian hydrodynamic equations

We apply fluid dynamics to macroscopic phenomena by assuming that the fluid is a continuous medium where the individual elements are large enough to contain a large number of atoms or molecules. The fluid elements are assumed to be very small compared to the overall volume, but large compared to the intermolecular spacings. The state of a moving fluid is characterized by five quantities, the three components of velocity, the pressure, and the density. For an ideal fluid, a complete system of five equations consists of the three momentum (Euler) equations, the equation of continuity, and the equation of state.

The behavior of the fluid may be understood using either a Eulerian or Lagrangian description. In the Eulerian description, we observe the fluid from a fixed laboratory frame. The physical properties of the fluid are regarded as field quantities, $\vec{f}(\vec{r},t)$, where $\vec{f}$ may be the velocity $\vec{v}$ and $\vec{r}$ and t are independent variables. In the Lagrangian description, the motion of a fluid element is followed. The position vector $\vec{r}(\vec{\xi},t)$ is a function of a Lagrangian variable $\vec{\xi}$, which may denote different physical properties, and time t. These two descriptions are linked by the *convective derivative*, taken following the motion of a particular fluid element, given by

$$\frac{d}{dt} = \frac{\partial}{\partial t} + \vec{v}\cdot\vec{\nabla}, \tag{4.2.1}$$

where $\vec{v}(\vec{r},t) \equiv d\vec{r}/dt = \dot{\vec{r}}$ and $\vec{r}$ is the Eulerian position variable.

Consider the equations of hydrodynamics in the Eulerian description. We first derive the equation of continuity. The mass of fluid flowing in unit time through an element $d\vec{f}$ of the surface bounding a volume is

$$-\frac{\partial M}{\partial t} = -\frac{\partial}{\partial t}\int \rho dV = \oint \rho\vec{v}\cdot d\vec{f}. \tag{4.2.2}$$

The differential form of the continuity equation is then,

$$\frac{\partial \rho}{\partial t} + \vec{\nabla}\cdot(\rho\vec{v}) = \frac{\partial \rho}{\partial t} + \rho\vec{\nabla}\cdot\vec{v} + \vec{v}\cdot\vec{\nabla}\rho = 0. \tag{4.2.3}$$

Consider the momentum equation. The total force acting on some volume in a fluid is

$$-\oint P d\vec{f} = -\int \vec{\nabla}\cdot\mathbf{P} dV, \tag{4.2.4}$$

where $\mathbf{P}$ is the pressure tensor. The equation of motion can then be written as

$$\rho \frac{d\vec{v}}{dt} = -\vec{\nabla} \cdot \mathbf{P} + \rho \vec{g}, \tag{4.2.5}$$

where g is the total body or external force per unit mass. In order to obtain the conservative form of this equation, we rewrite the left-hand side as

$$\begin{aligned}
\rho \frac{d\vec{v}}{dt} &= \rho \frac{\partial \vec{v}}{\partial t} + \left(\rho \vec{v} \cdot \vec{\nabla}\right) \vec{v} \\
&= \frac{\partial}{\partial t}(\rho \vec{v}) - \vec{v} \frac{\partial \rho}{\partial t} + \left(\rho \vec{v} \cdot \vec{\nabla}\right) \vec{v} \\
&= \frac{\partial}{\partial t}(\rho \vec{v}) + \vec{v} \vec{\nabla} \cdot (\rho \vec{v}) + \left(\rho \vec{v} \cdot \vec{\nabla}\right) \vec{v} \\
&= \frac{\partial}{\partial t}(\rho \vec{v}) + \vec{\nabla} \cdot (\rho \vec{v} \vec{v}).
\end{aligned}$$

Then,

$$\frac{\partial}{\partial t}(\rho \vec{v}) + \vec{\nabla} \cdot (\rho \vec{v} \vec{v} + \mathbf{P}) = \rho \vec{g} \tag{4.2.6}$$

For pressures that are purely isotropic, the pressure tensor is of the form

$$\mathbf{P} = P\mathbf{I}, \tag{4.2.7}$$

where $\mathbf{I}$ is the identity tensor and $\vec{\nabla} \cdot \mathbf{P} = \vec{\nabla} P$. Consider the conservation of energy equation. The change in energy of a unit volume of fluid with time is

$$\frac{\partial}{\partial t}\left(\frac{1}{2}\rho v^2 + \rho \varepsilon\right).$$

The first quantity is

$$\begin{aligned}
\frac{\partial}{\partial t}\left(\frac{1}{2}\rho v^2\right) &= \frac{1}{2} v^2 \frac{\partial \rho}{\partial t} + \rho \vec{v} \cdot \frac{\partial \vec{v}}{\partial t} \\
&= -\frac{1}{2} v^2 \vec{\nabla} \cdot (\rho \vec{v}) - \vec{v} \cdot \vec{\nabla} P - \rho \vec{v} \cdot (\vec{v} \cdot \vec{\nabla}) \vec{v} \\
&= -\frac{1}{2} v^2 \vec{\nabla} \cdot (\rho \vec{v}) - \rho \vec{v} \cdot \vec{\nabla}\left(\frac{1}{2} v^2 + w\right) + \rho T \vec{v} \cdot \vec{\nabla} s. \qquad (4.2.8)
\end{aligned}$$

To write the second quantity, consider the thermodynamic relation

$$d\varepsilon = T ds - p dV = T ds + \frac{P}{\rho^2} d\rho$$

and the definition of the enthalpy, $w = \varepsilon + P/\rho$, such that

$$d(\rho\varepsilon) = \varepsilon d\rho + \rho d\varepsilon = w d\rho + \rho T ds.$$

Then, the second quantity is

$$\frac{\partial(\rho\varepsilon)}{\partial t} = w\frac{\partial \rho}{\partial t} + \rho T\frac{\partial s}{\partial t} = -w\vec{\nabla}\cdot(\rho\vec{v}) - \rho T\vec{v}\cdot\vec{\nabla}s. \tag{4.2.9}$$

The conservation of total energy equation is then

$$\begin{aligned} \frac{\partial}{\partial t}\left(\frac{1}{2}\rho v^2 + \rho\varepsilon\right) &= -\left(\frac{1}{2}v^2 + w\right)\vec{\nabla}\cdot(\rho\vec{v}) - \rho\vec{v}\cdot\vec{\nabla}\left(\frac{1}{2}v^2 + w\right) \\ &= -\vec{\nabla}\cdot\left[\rho\vec{v}\left(\frac{1}{2}v^2 + w\right)\right]. \end{aligned} \tag{4.2.10}$$

Integrating and applying Gauss' law, we have the integral form,

$$\begin{aligned} \frac{\partial}{\partial t}\int\left(\frac{1}{2}\rho v^2 + \rho\varepsilon\right)dV &= -\oint \rho\vec{v}\left(\frac{1}{2}v^2 + w\right)\cdot d\sigma \\ &= -\oint \rho\vec{v}\left(\frac{1}{2}v^2 + \varepsilon\right)\cdot d\sigma - \oint p\vec{v}\cdot d\sigma. \end{aligned} \tag{4.2.11}$$

We would like to have the hydrodynamic equations in the Lagrangian description. Define the Lagrangian mass coordinate $\xi = m$ and Lagrangian time t' in one dimensional Cartesian coordinates as

$$m = m(r,t) = \int^r dr'\rho(r',t), \qquad\qquad t' = t. \tag{4.2.12}$$

Using these equations, we express a coordinate transformation from the Eulerian frame (r,t) to the Lagrangian frame (m,t'). The Jacobian matrix is

$$J^i{}_j = \begin{pmatrix} \frac{\partial m}{\partial r} & \frac{\partial t'}{\partial r} \\ \frac{\partial m}{\partial t} & \frac{\partial t'}{\partial t} \end{pmatrix} = \begin{pmatrix} \rho & 0 \\ -\rho V & 1 \end{pmatrix}, \tag{4.2.13}$$

where $J = |J^i{}_j| = \rho$. Then, we may transform the partial derivatives as

$$\frac{\partial}{\partial r} = \rho\frac{\partial}{\partial m}, \qquad\qquad \frac{\partial}{\partial t} = -\rho V\frac{\partial}{\partial m} + \frac{\partial}{\partial t'}. \tag{4.2.14}$$

We may also define a volume coordinate τ such that

$$\tau = r, \qquad\qquad d\tau = dr. \tag{4.2.15}$$

Then, we have the following partial derivatives,

$$\frac{\partial}{\partial r} = \frac{\partial}{\partial \tau} = \rho\frac{\partial}{\partial m}, \qquad \frac{\partial}{\partial \tau} = \rho\frac{\partial}{\partial m}, \qquad \frac{\partial \tau}{\partial m} = \frac{1}{\rho}. \tag{4.2.16}$$

Transforming the Eulerian forms of the continuity (4.2.3), momentum (4.2.6), and energy (4.2.10) equations, we obtain the Lagrangian continuity equation,

$$\frac{\partial \tau}{\partial t} - \frac{\partial v}{\partial m} = 0, \tag{4.2.17}$$

the Lagrangian momentum equation,

$$\frac{\partial v}{\partial t} + \frac{\partial p}{\partial m} = g, \tag{4.2.18}$$

and the Lagrangian energy equation,

$$\frac{\partial E}{\partial t} + \frac{\partial}{\partial m}(vp) = vg, \tag{4.2.19}$$

in one dimension, with total energy $E = \varepsilon + \frac{1}{2}v^2$.

4.2.2 Riemann problem

A conservation law with piece-wise constant data having a single discontinuity is known as a Riemann problem. For our calculations, this occurs at every zone interface in our computational domain in solving the hydrodynamic equations. The fluid variables are discretized on the domain and appear as piece-wise constant across the interface. The Riemann problem for our equations is non-linear and we present the solver for our code below.

4.2.3 Godunov method

In this subsection we present the Godunov method, as discussed more generally in [66]. Consider a hyperbolic conservation law of the form

$$\frac{\partial q}{\partial t} + \frac{\partial}{\partial x}f(q,t) = 0, \tag{4.2.20}$$

where q is the vector of conserved quantities and f is the flux function. Let the i^{th} grid cell be defined by

$$\mathcal{C}_i = (x_{i-1/2}, x_{i+1/2}) \tag{4.2.21}$$

with cell-average value of $q(x, t_n)$,

$$Q_i^n \approx \frac{1}{\Delta x} \int_{x_{i-1/2}}^{x_{i+1/2}} q(x, t_n) \equiv \frac{1}{\Delta x} \int_{C_i} q(x, t_n) dx, \tag{4.2.22}$$

where $\Delta x = x_{i+1/2} - x_{i-1/2}$. The conservative update is

$$Q_i^{n+1} = Q_i^n - \frac{\Delta t}{\Delta x} \left(F_{i+1/2}^n - F_{i-1/2}^n \right), \tag{4.2.23}$$

where

$$F_{i-1/2}^n \approx \frac{1}{\Delta t} \int_{t_n}^{t_{n+1}} f(q(x_{i-1/2,t}, t))dt, \tag{4.2.24}$$

is an approximation to the average flux along $x = x_{i-1/2}$. We assume that the average flux is defined by a numerical flux function $\mathcal{F}$, where

$$F_{i-1/2}^n = \mathcal{F}\left(Q_{i-1}^n, Q_i^n\right). \tag{4.2.25}$$

Then, (4.2.23) becomes

$$Q_i^{n+1} = Q_i^n - \frac{\Delta t}{\Delta x} \left[\mathcal{F}\left(Q_i^n, Q_{i+1}^n\right) - \mathcal{F}\left(Q_{i-1}^n, Q_i^n\right) \right]. \tag{4.2.26}$$

Note that the sum of the flux differences cancels out except for the fluxes at the boundary. Therefore, over the full domain, there is exact conservation except for the fluxes at the boundaries.

We may compute the integral of (4.2.24) exactly by replacing $q(x, t)$ by $\tilde{q}^n(x, t)$. Let $Q_{i-1/2}^* = q^*(Q_{i-1}^n, Q_i^n)$ be the solution to the Riemann problem at $x_{i-1/2}$. We define the numerical flux $F_{i-1/2}^n$ as

$$F_{i-1/2}^n = \frac{1}{\Delta t} \int_{t_n}^{t_{n+1}} f(q^*(Q_{i-1}^n, Q_i^n))dt = f(q^*(Q_{i-1}^n, Q_i^n)). \tag{4.2.27}$$

Then, the Godunov method may be defined as (1) solving the Riemann problem at $x_{i-1/2}$ to obtain $q^*(Q_{i-1}^n, Q_i^n)$, (2) defining the flux $F_{i-1/2}^n = \mathcal{F}(Q_{i-1}^n, Q_i^n)$ by (4.2.27), (3) applying the flux-differencing formula (4.2.23).

4.2.4 PPMLR algorithm

The hydrodynamics solver is a version of Virginia Hydrodynamics-1 (VH-1) [67] for parallel processors (MPI) and written in C. The hydrodynamics calculation is performed for one time step using the piecewise parabolic method (PPM) in Lagrangian coordinates by Woodward and Colella [68]. The method is an extension of Godunov's first-order method by taking into account the correct domain of dependence of zone edges in calculating the conservative fluxes. The method consists of the interpolation of hydrodynamic variables across the domain, the calculation at the zone edges of the solution to the initial value problem using characteristic equations and Riemann solvers, and the use of these solutions to calculate effective fluxes in conservative form. The results are then mapped onto a fixed Eulerian grid using a Lagrangian remap step (PPMLR).

In our calculations, we consider a finite volume domain where cell centers are denoted by j and cell faces by $j+1/2$. We assume that the conserved quantities $U = (\tau, v, E)$ are mass-weighted averages at time t^n,

$$U_j^n = \frac{1}{\Delta m_j} \int_{m_{j-1/2}}^{m_{j+1/2}} U(m, t^n) dm, \qquad m_{j+1/2} = \sum_{k \leq j} \Delta m_k, \tag{4.2.28}$$

where Δm_j is the amount of mass contained in the j^{th} zone. Define $r_{j+1/2}^n = r(m_{j+1/2}, t^n)$ as a separate dependent variable given by

$$r_{j+1/2}^n - r_{j_0+1/2}^n = \sum_{j_0 \leq k \leq j} \tau_k^m \Delta m_k \tag{4.2.29}$$

We apply a conservative update method to calculate U_j^{n+1}, the average values for the conserved quantitites at time $t^{n+1} = t^n + \Delta t$. The known quantities at time step t^n are the mass increments Δm_j and mass-weighted averages τ_j^n, u_j^n, and E_j^n. In PPMLR, pressure p is interpolated instead of the total energy in order to obtain a better-behaved solution near shocks. The average value of the pressure in the zone is evaluated from the averages of the conserved quantities and is a second-order-accurate value.

Next we shall give the interpolation parabola for the fluid variables. Consider the linear advection equation

$$\frac{\partial a}{\partial t} + c\frac{\partial a}{\partial \xi} = 0, \qquad a(\xi, 0) = a_0(\xi). \tag{4.2.30}$$

Let $\xi_{j+1/2}$ be the boundary between zones j and the $j+1$. We assume that the average value a_j^n of the solution between $\xi_{j+1/2}$ and $\xi_{j-1/2}$ at time t^n is known,

$$a_j^n = \frac{1}{\Delta\xi_j}\int_{\xi_{j-1/2}}^{\xi_{j+1/2}} a(\xi, t^n)d\xi, \qquad \Delta\xi_j = \xi_{j+1/2} - \xi_{j-1/2}. \tag{4.2.31}$$

We calculate a_j^{n+1}, the average value of the solution at time $t^{n+1} = t^n + \Delta t$ such that Δt satisfies the stability condition $u\Delta t \leq \min_j \Delta\xi_j$. First, construct a piecewise polynomial interpolation function $a(\xi)$ such that

$$a_j^n = \frac{1}{\Delta\xi_j}\int_{\xi_{j-1/2}}^{\xi_{j+1/2}} a(\xi)d\xi \tag{4.2.32}$$

and that no new extrema appear in the interpolation function than the ones that already exist for a_j^n. Using the exact solution to the advection equation (4.2.30), $a(\xi, t^n + \Delta t) = a(\xi - c\Delta t)$, we have

$$a_j^{n+1} = \frac{1}{\Delta\xi_j}\int_{\xi_{j-1/2}}^{\xi_{j+1/2}} a(\xi - c\Delta t)d\xi. \tag{4.2.33}$$

We define the interpolating polynomial as

$$a(\xi) = a_{L,j} + x[\Delta a_j + a_{6,j}(1-x)], \qquad x = \frac{\xi - \xi_{j-1/2}}{\Delta\xi_j}, \tag{4.2.34}$$

where $\xi_{j-1/2} \leq \xi \leq \xi_{j+1/2}$, $\lim_{\xi\to\xi_{j-1/2}} = a_{L,j}$, $\lim_{\xi\to\xi_{j+1/2}} = a_{R,j}$, and

$$\Delta a_j = a_{R,j} - a_{L,j}, \qquad a_{6,j} = 6[a_j^n - \frac{1}{2}(a_{L,j} + a_{R,j})]. \tag{4.2.35}$$

The formula for the value of $a_{j+1/2}$ at the zone faces is given by [68]

$$\begin{aligned} a_{j+1/2} \quad = \quad & a_j^n + \frac{\Delta\xi_j}{\Delta\xi_j + \Delta\xi_{j+1}}\left(a_{j+1}^n - a_j^n\right) + \frac{1}{\sum_{k=-1}^{2}\Delta\xi_{j+k}} \\ & \times\Big\{\frac{2\Delta\xi_{j+1}\Delta\xi_j}{\Delta\xi_j + \Delta\xi_{j+1}}\left[\frac{\Delta\xi_{j-1} + \Delta\xi_j}{2\Delta\xi_j + \Delta\xi_{j+1}} - \frac{\Delta\xi_{j+2} + \Delta\xi_{j+1}}{2\Delta\xi_{j+1} + \Delta\xi_j}\right](a_{j+1}^n - a_j^n) \\ & -\Delta\xi_j\frac{\Delta\xi_{j-1} + \Delta\xi_j}{2\Delta\xi_j + \Delta\xi_{j+1}}\delta a_{j+1} + \Delta\xi_{j+1}\frac{\Delta\xi_{j+1} + \Delta\xi_{j+2}}{\Delta\xi_j + 2\Delta\xi_{j+1}}\delta a_j\Big\}, \end{aligned} \tag{4.2.36}$$

where

$$\delta_m a_j = \min(|\delta a_j|, 2|a_j^n - a_{j-1}^n|, 2|a_j^n - a_{j-1}^n|)\mathrm{sgn}(\delta a_j), \tag{4.2.37}$$

if $(a_{j+1}^n - a_j^n)(a_j^n - a_{j-1}^n) > 0$ and 0 otherwise. The value at the zone faces $a_{j+1/2}$ will be assigned to variables $a_{L,j}$ and $a_{R,j}$ (the left and right faces of cell j) for most values of j. There are a few exceptions that require the following conditions,

$$
\begin{aligned}
a_{L,j} \to a_j^n, a_{R,j} \to a_j^n \qquad & \text{if} \quad (a_{R,j} - a_j^n)(a_j^n - a_{L,j}) \geq 0, \\
a_{L,j} \to 3a_j^n - 2a_{R,j} \qquad & \text{if} \quad (a_{R,j} - a_{L,j}) \left(a_j^n - \tfrac{1}{2}(a_{L,j} + a_{R,j})\right) > \tfrac{1}{6}(a_{R,j} - a_{L,j})^2 \\
a_{R,j} \to 3a_j^n - a_{L,j} \qquad & \text{if} \quad -\tfrac{1}{6}(a_{R,j} - a_{L,j})^2 > (a_{R,j} - a_{L,j}) \left(a_j^n - \tfrac{1}{2}(a_{R,j} + a_{L,j})\right).
\end{aligned} \tag{4.2.38}
$$

For the Lagrangian hydrodynamic equations, we use the same algorithm above for the advection equation to interpolate profiles for τ, u, p as functions of the mass coordinate m on the grid. We then solve the Riemann problem at the zone faces to calculate the time-averaged pressures and velocities. In the final step we make a conservative update of the quantities by applying the forces implied by the time-averaged pressures and velocities at the zone faces.

Consider the time-averaged pressures and velocities at the edges of the zones. In smooth regions, $\bar{u}_{j+1/2}$ and $\bar{p}_{j+1/2}$ approximate time averages to the solution of the equations in characteristic form

$$
du \pm dp/C = gdt \qquad \text{along} \qquad dm = \pm Cdt, \tag{4.2.39}
$$

where $C = (\gamma p \rho)^{1/2}$ [69]. We consider the two domains of dependence for a zone interface during the time step by tracing the paths of sound waves arriving at the interface at the end of the time step. The interpolated variable within each domain of dependence is replaced by its mass-weighted average ($u_{j+1/2,L}$ and $u_{j+1/2,R}$, and $p_{j+1/2,L}$ and $p_{j+1/2,R}$). From Colella and Woodward [68], this facilitates the computation of the nonlinear interaction of the two domains of dependence. The quantities $\bar{u}_{j+1/2}$ and $\bar{p}_{j+1/2}$ are the interaction of these averaged states and may be obtained by solving the Riemann problem.

The Riemann solver will calculate the time-averaged pressures $\bar{p}_{j+1/2}$ and velocities $\bar{u}_{j+1/2}$ at the edges of zones given the input states $u_{j+1/2,L}$ and $u_{j+1/2,R}$ and $p_{j+1/2,L}$ and $p_{j+1/2,R}$. We may then apply the same procedure as the Godunov method to obtain the numerical fluxes with the difference that the left and right states input states to the Riemann problem are the averages over only the parts of each zone which are in the domain of dependence.

We now show how to calculate the input states for the Riemann solver [68]. The averages of the interpolation functions are

$$
\begin{aligned}
f^a_{j+1/2,L}(y) &= \frac{1}{y}\int_{\xi_{j+1/2}-y}^{\xi_{j+1/2}} a(\xi)d\xi, && (4.2.40)\\
f^a_{j+1/2,R}(y) &= \frac{1}{y}\int_{\xi_{j+1/2}+y}^{\xi_{j+1/2}} a(\xi)d\xi, && (4.2.41)
\end{aligned}
$$

for positive y. We may write

$$
\begin{aligned}
f^a_{j+1/2,L}(y) &= a_{R,j} - \frac{x}{2}\left[\Delta a_j - \left(1-\frac{2}{3}x\right)a_{6,j}\right], \quad \text{for } x = \frac{y}{\Delta\xi_j}, && (4.2.42)\\
f^a_{j+1/2,R}(y) &= a_{L,j+1} - \frac{x}{2}\left[\Delta a_{j+1} - \left(1-\frac{2}{3}x\right)a_{6,j+1}\right], \quad \text{for } x = \frac{y}{\Delta\xi_{j+1}}. && (4.2.43)
\end{aligned}
$$

First consider the absence of body forces ($g = 0$). Define the average values of the dependent variables over the region between $m_{j+1/2}$ and the point where the $\pm$ characteristic through $(m_{j+1/2}, t^{n+1})$ intersects the line $t = t^n$,

$$
\begin{aligned}
a^+_{j+1/2} &= f^a_{j+1/2,L}(\Delta t C^n_j A^n_j), && (4.2.44)\\
a^-_{j+1/2} &= f^a_{j+1/2,R}(\Delta t C^n_{j+1} A^n_{j+1}), && (4.2.45)
\end{aligned}
$$

where $a^\pm_{j+1/2} = (\tau^\pm_{j+1/2}, u^\pm_{j+1/2}, p^\pm_{j+1/2})$ and

$$
A^n_j = \frac{r^n_{j+1/2} - r^n_{j-1/2}}{r^n_{j+1/2} - r^n_{j-1/2}}. \quad (4.2.46)
$$

Then, the input states for the Riemann problem are $a_{j+1/2,L} = a^+_{j+1/2}$ and $a_{j+1/2,R} = a^-_{j+1/2}$. For body forces ($g \neq 0$),

$$
\begin{aligned}
p_{j+1/2,L} &= p^+_{j+1/2} + \Delta t C^+_{j+1/2} g^n_j,\\
p_{j+1/2,R} &= p^-_{j+1/2} + \Delta t C^-_{j+1/2} g^n_{j+1}. && (4.2.47)
\end{aligned}
$$

Note that in VH-1, the body forces are treated differently. Instead, the left and right input states of the velocity are modified,

$$
\begin{aligned}
u_{j+1/2,L} &= u_{j+1/2,L} + \tfrac{1}{2}\Delta t g^n_j,\\
u_{j+1/2,R} &= u_{j+1/2,R} + \tfrac{1}{2}\Delta t g^n_{j+1}. && (4.2.48)
\end{aligned}
$$

We now give the Riemann solver for our calculations. From the Rankine-Hugoniot relations, we obtain the following nonlinear equations [68]

$$\begin{aligned}
\frac{\bar{p}_{j+1/2} - p_{j+1/2,L}}{W_L} + (\bar{u}_{j+1/2} - u_{j+1/2,L}) = 0, \\
W_L^2 = \left(\frac{\gamma p^{+}_{j+1/2}}{\tau^{+}_{j+1/2}}\right)\left[1 + \frac{\gamma+1}{2\gamma}\left(\frac{\bar{p}_{j+1/2}}{p_{j+1/2,L}} - 1\right)\right], \\
\frac{\bar{p}_{j+1/2} - p_{j+1/2,R}}{W_R} + (\bar{u}_{j+1/2} - u_{j+1/2,R}) = 0, \\
W_R^2 = \left(\frac{\gamma p^{-}_{j+1/2}}{\tau^{-}_{j+1/2}}\right)\left[1 + \frac{\gamma+1}{2\gamma}\left(\frac{\bar{p}_{j+1/2}}{p_{j+1/2,R}} - 1\right)\right],
\end{aligned} \tag{4.2.49}$$

which are finite difference approximations to the characteristic equations. We use Newton's method with a fixed number of iterations to solve for $\bar{p}_{j+1/2}$ and $\bar{u}_{j+1/2}$.

From Colella and Woodward [68], to produce a well-behaved Eulerian method, all interpolations for both the Lagrangian step and the remap must be performed in the volume coordinate r rather than in the mass coordinate. The finite difference approximation to the fundamental conservation laws may then be written as

$$\begin{aligned}
r^{n+1}_{j+1/2} &= r^{n}_{j+1/2} + \Delta t \bar{u}_{j+1/2}, \\
\tau^{n+1}_{j} &= \frac{r^{n+1}_{j+1/2} - r^{n+1}_{j-1/2}}{\Delta m_j}, \\
u^{n+1}_{j} &= u^{n}_{j}\frac{\Delta t}{\Delta m_j}(\bar{p}_{j-1/2} - \bar{p}_{j+1/2}) + \frac{\Delta t}{2}\left(g^n_j + g^{n+1}_j\right), \\
E^{n+1}_{j} &= E^{n}_{j} + \frac{\Delta t}{\Delta m_j}\left(\bar{p}_{j-1/2} - \bar{p}_{j+1/2}\right) + \frac{\Delta t}{2}\left(u^n_j g^n_j + u^{n+1}_j g^{n+1}_j\right),
\end{aligned} \tag{4.2.50}$$

where $\bar{p}_{j+1/2}$ and $\bar{u}_{j+1/2}$ the time-averaged pressures and velocities at the edges of zones. Note that in our calculations we do not calculate g^{n+1} so instead we have

$$\begin{aligned}
u^{n+1}_{j} &= u^{n}_{j}\frac{\Delta t}{\Delta m_j}(\bar{p}_{j-1/2} - \bar{p}_{j+1/2}) + \Delta t g^n_j, \\
E^{n+1}_{j} &= E^{n}_{j} + \frac{\Delta t}{\Delta m_j}\left(\bar{p}_{j-1/2} - \bar{p}_{j+1/2}\right) + \Delta t u^n_j g^n_j.
\end{aligned} \tag{4.2.51}$$

4.2.5 Numerical tests

In this subsection, we present results of applying the hydrodynamics solver to a set of standard test problems. For all of these tests, we use $\gamma = 1.4$. The first test is known as the one-dimensional Sod shock tube problem [70], which has a known analytical solution [71]. We used 1024 zones and a Courant number of 0.5. In the left panel of Figure 4.1, we give the density along $x = [0, 1]$ at a final time $t = 0.05$. We initialize the domain into two regions: Region I from $x = [0, 0.5]$ and Region II from $x = [0.5, 1]$. The velocity of the gas in both regions is initially zero and we have the density and pressure for Region I and II,

$$\rho_I = 1.0, \qquad p_I = 1.0, \qquad \rho_{II} = 0.125, \qquad p_{II} = 0.1. \tag{4.2.52}$$

We may compare the results in the left panel in Figure 4.1 with [71]. The next three tests are from Woodward and Colella [72]. The second test is for two one-dimensional interacting blast waves. We used 1024 zones and a Courant number of 0.8. In the right panel of Figure 4.1, we give the density along $x = [0, 1]$ at final time $t = 0.04$. The domain is initially divided into three regions: Region I from $x = [0, 0.1]$, Region II from $x = [0.1, 0.9]$, and Region III from $x = [0.9, 1.0]$. Initially, the gas is stationary and has density and pressure in the three regions as

$$\rho_I = 1.0, \quad p_I = 1000.0, \quad \rho_{II} = 1.0, \quad p_{II} = 0.01, \quad \rho_{III} = 1.0, \quad p_{III} = 100.0. \tag{4.2.53}$$

The velocity of the gas in all three regions is zero. We may compare the results in the right panel of Figure 4.1 with that of [72].

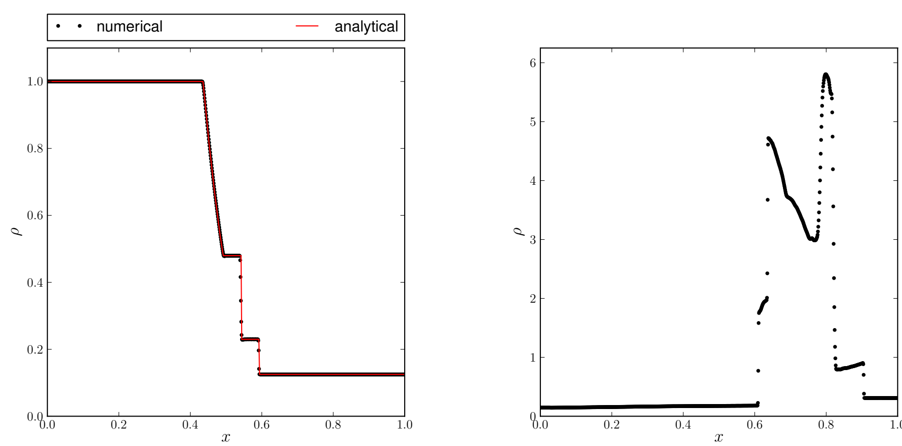

Figure 4.1: Density profiles for 1D tests: Sod shock tube and two interacting blast waves. The time given in the left panel is $t = 0.05$ and the right panel is $t = 0.04$. We compare the left results with [71] and the right results with [72].

The third test is a two-dimensional Mach 3 wind tunnel with a step. We used 480 zones along $x = [0, 3]$, 160 zones along $y = [0, 1]$, and a Courant number of 0.8. In Figure 4.2 we give the 2D

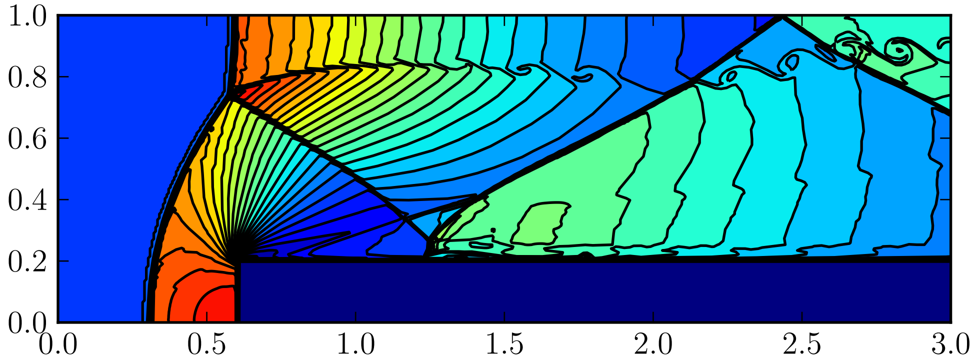

Figure 4.2: 2D density profile for Mach 3 wind tunnel with a step. The time given is $t = 4.0$. We compare the results with [72].

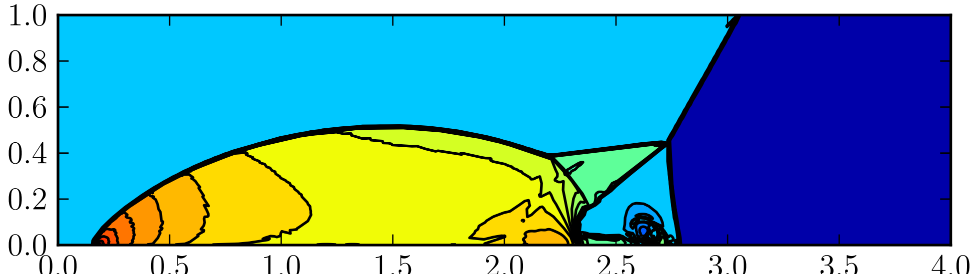

Figure 4.3: 2D density profile for the double Mach reflection of a strong shock test. The time given is $t = 0.2$. We compare the results with [72].

density profile at a final time $t = 4.0$. The step is defined to be at $x = [0.6, 3]$ and $y = [0, 0.2]$. The rest of the domain is initialized to

$$\rho = 1.4, \qquad p = 1.0, \qquad v_x = 3.0, \qquad v_y = 0. \tag{4.2.54}$$

The inner boundary in the x-direction has an inflow condition with the above variables. At the step, at $x = 0.6$ and $y \leq 0.2$, the outer boundary is a solid wall condition. For $y > 0.2$, the outer boundary at the end of the domain is a zero-gradient outflow condition. The boundary condition for the y-direction at the edges of the domain as well as the step at $x \geq 0.6$ and $y = 0.2$ are solid wall conditions. We compare the results in Figure 4.2 with [72]. The fourth test is a double Mach reflection of a strong shock. We used 480 zones along $x = [0, 4.0]$, 160 zones along $y = [0, 1.0]$, and a Courant number of 0.8. In Figure 4.3 we give the 2D density profile at a final time $t = 0.2$. Instead of modeling the wedge, we set up an appropriate boundary treatment to model the shock wave [73].

We define two sets of initial conditions: post-shock

$$\rho_{\text{post}} = 0.8, \qquad p_{\text{post}} = 116.6, \qquad v_{x,\text{post}} = 8.25\cos(30^o), \qquad v_{y,\text{post}} = -8.25\sin(30^o) \qquad (4.2.55)$$

and pre-shock,

$$\rho_{\text{pre}} = 0.8, \qquad p_{\text{pre}} = 116.6, \qquad v_{x,\text{pre}} = 8.25\cos(30^o), \qquad v_{y,\text{pre}} = -8.25\sin(30^o). \qquad (4.2.56)$$

Define a point on the x-axis as $x_0 = 1/6$. We initialize the domain to have a post-shock region defined for all $x < x_0 + y/\sqrt{3}$. We initialize the rest to be the pre-shock region. The inner boundary in the x-direction uses the post-shock variables as the inflow condition. The outer boundary in the y-direction uses the pre-shock variables in the ghost-zone region. For the y-direction, if $x < x_0$ then the inner boundary condition is an inflow condition with the post-shock variables, otherwise it is a solid wall condition. We define the location of the shock front as $x_s = x_0 + (1 + 20t)/\sqrt{3}$. The outer boundary then has post-shock variables for the ghost zones at $x < x_s$ and the pre-shock variables otherwise. We compare the results in Figure 4.3 with [72].

4.3 Pseudo-spectral Poisson solver

In this section, we present our numerical method for solving for the Newtonian self-gravitational potential of the star. This method is based on that of Broderick and Rathore [74] and we present an extension for cell-centered data.

4.3.1 Overview of the method

We add accelerations for a self-gravitating fluid to the hydrodynamics solver using the gravitational potential obtained in a separate calculation. The Poisson equation for a 3D Cartesian grid,

$$\nabla^2 \Phi(x, y, z) = 4\pi G \rho(x, y, z), \qquad (4.3.1)$$

is solved with parallel, partial-sum, discrete sine transforms and an image-mass treatment of the boundary. For homogeneous boundary conditions, this may be solved directly using a discrete sine transform (DST) method. To obtain the appropriate solution for the self-gravity of the star, we must specify inhomogeneous boundary conditions. The physical solution will only vanish at infinity and, in general, Φ will be non-zero at the edge of the computational domain. In order to use DSTs, we convert the inhomogenous boundary condition into a homogeneous one with the introduction of a boundary mass, ρ_B. Poisson's equation may then be written as

$$\nabla^2\Phi = 4\pi G\left(\rho + \rho_B\right) = 4\pi G\rho_{total}. \tag{4.3.2}$$

Thus, we obtain the solution to Poisson's equation by applying a three-dimensional discrete sine transform to a source which includes the density of interest and boundary image mass, integrate to obtain the spectral amplitudes, then compute the inverse transform for Φ with proper asymptotic fall-off built in.

4.3.2 Sine transforms

1D Discrete sine transform

The grid consists of cell-centered data. For data that behave as odd functions at the boundary, the type-II DST may be implemented. Let I be the number of zones in the x-direction. Let i and l denote the number of basis functions in the real and frequency domain where $k_l = (l+1)/(I\Delta)$ and $x_i = (i+1/2)\Delta$ for grid spacing Δ. The discrete sine transform of a function f may be defined [75] as

$$\hat{f}(k_l) = \sum_{i=0}^{I-1} f(x_i)\sin\left(\pi k_l x_i\right), \tag{4.3.3}$$

with inverse

$$f(x_i) = \frac{2}{I}\sum_{l=0}^{I-2}\hat{f}(k_l)\sin\left(\pi k_l x_i\right) + \frac{(-1)^i}{I}\hat{f}(k_{I-1}), \tag{4.3.4}$$

3D Discrete sine transform

Let I, J, K be the number of zones in the x-,y-, and z-direction. Let i, j, k and l, m, n denote the number of basis functions in the real and frequency domain. The 3D discrete sine transform of a function f may be defined, as a three-step partial sum, as

$$\begin{aligned}
u_{ljk} &= \sum_{i=0}^{I-1} f_{ijk}\sin\left[\frac{\pi(i+1/2)(l+1)}{I}\right], \\
v_{lmk} &= \sum_{j=0}^{J-1} u_{ljk}\sin\left[\frac{\pi(j+1/2)(m+1)}{J}\right], \\
\hat{f}_{lmn} &= \sum_{k=0}^{K-1} v_{lmk}\sin\left[\frac{\pi(k+1/2)(n+1)}{K}\right],
\end{aligned} \tag{4.3.5}$$

with inverse

$$
\begin{aligned}
w_{lmk} &= \frac{2}{K}\sum_{n=0}^{K-2}\hat{f}_{lmn}\sin\left[\frac{\pi(k+1/2)(n+1)}{K}\right]+\frac{(-1)^k}{K}\hat{f}_{lm,K-1} \\
y_{ljk} &= \frac{2}{J}\sum_{m=0}^{J-2}w_{lmk}\sin\left[\frac{\pi(j+1/2)(m+1)}{J}\right]+\frac{(-1)^j}{J}w_{l,J-1,k} \\
f_{ijk} &= \frac{2}{I}\sum_{l=0}^{I-2}y_{ljk}\sin\left[\frac{\pi(i+1/2)(l+1)}{I}\right]+\frac{(-1)^i}{I}y_{I-1,j,k}.
\end{aligned}
\tag{4.3.6}
$$

4.3.3 Spectral integration

Consider the 3D Poisson equation in finite difference form,

$$
\begin{aligned}
\nabla^2\Phi_{ijk} &= (\Phi_{i+1,jk}-2\Phi_{ijk}+\Phi_{i-1,jk})/(\Delta x_i)^2 \\
&\quad +(\Phi_{i,j+1,k}-2\Phi_{ijk}+\Phi_{i,j-1,k})/(\Delta y_j)^2 \\
&\quad +(\Phi_{ij,k+1}-2\Phi_{ijk}+\Phi_{ij,k-1})/(\Delta z_k)^2 \\
&= 4\pi G\rho_{ijk}.
\end{aligned}
$$

Substituting the inverse transform, one obtains the solution

$$
\hat{\Phi}_{lmn} = -4\pi G\frac{\hat{\rho}_{lmn}}{\kappa^2_{lmn}}, \tag{4.3.7}
$$

where

$$
\begin{aligned}
\kappa^2_{lmn} &= \frac{2}{(\Delta x_i)^2}\left[1-\cos\left(\frac{\pi(l+1)}{I}\right)\right] \\
&\quad +\frac{2}{(\Delta x_j)^2}\left[1-\cos\left(\frac{\pi(m+1)}{J}\right)\right] \\
&\quad +\frac{2}{(\Delta x_k)^2}\left[1-\cos\left(\frac{\pi(n+1)}{K}\right)\right].
\end{aligned}
$$

This may be shown in one dimension upon considering the second-derivative of the inverse transform

$$
\begin{aligned}
\Phi_{i+1} - 2\Phi_i + \Phi_{i-1} \qquad &= \frac{2}{I}\sum_{l=0}^{I-2}\hat{\Phi}_l \Bigg\{ \sin\left[\frac{\pi(i+1+1/2)(l+1)}{I}\right] - 2\sin\left[\frac{\pi(i+1/2)(l+1)}{I}\right] \\
&\quad + \sin\left[\frac{\pi(i+1/2-1)(l+1)}{I}\right]\Bigg\} + \frac{1}{I}\Phi_{I-1}\left[(-1)^{i+1} + (-1)^i + (-1)^{i-1}\right] \\
&= \frac{2}{I}\sum_{l=0}^{I-2}\hat{\Phi}_l \Bigg\{ -2\sin\left[\frac{\pi(i+1/2)(l+1)}{I}\right] \\
&\quad +2\sin\left[\frac{\pi(i+1/2)(l+1)}{I}\right]\cos\left[\frac{\pi(l+1)}{I}\right]\Bigg\} + \frac{1}{I}\Phi_{I-1}(-4)(-1)^i \\
&= \frac{2}{I}\sum_{l=0}^{I-2}\hat{\Phi}_l \sin\left[\frac{\pi(i+1/2)(l+1)}{I}\right]\left\{-2\left(1-\cos\left[\frac{\pi(l+1)}{I}\right]\right)\right\} \\
&\quad +\Phi_{I-1}(-4)(-1)^i \\
&= \frac{2}{I}\sum_{l=0}^{I-1}\hat{\Phi}_l \sin\left[\frac{\pi(i+1/2)(l+1)}{I}\right](-2)\left\{1-\cos\left[\frac{\pi(l+1)}{I}\right]\right\}.
\end{aligned}
$$

4.3.4 Image mass boundary condition

Initially, there is a non-zero distribution of mass in the center of the computational domain. If we solve Poisson's equation with this distribution, the resulting potential will fall off faster than it should in order to be zero at the edge of the domain. We add image mass to the boundary faces in order to obtain a more appropriate large r behavior, consistent with $\mathcal{O}(1/r)$ fall off at infinity. The image mass is constructed using the multipole expansion,

$$\Phi^B(\vec{x}) = -\sum_{l=0}^{l_{max}}\sum_{m=-l}^{l}\frac{4\pi G}{2l+1}r^{-(l+1)}Q_{lm}Y_{lm}(\vec{x}), \tag{4.3.8}$$

where

$$Q_{lm} = \int d\vec{x}' r'^l Y^*_{lm}(\vec{x}')\rho(\vec{x}').$$

Let $n = 0$ be the innermost cell in the computational domain. For cell-centered data, the Dirichlet boundary condition is specified at the cell edge at $n = -1/2$. For second-order boundary conditions, we write the value of the potential at the boundary to be

$$\Phi_{-1/2} = \frac{1}{2}(\Phi_{-1} + \Phi_0), \tag{4.3.9}$$

where Φ_{-1} is outside the computational domain, i.e., a ghost zone. For homogeneous boundary conditions,

$$\Phi_{-1/2} = 0 \longrightarrow \Phi_{-1} = -\Phi_0. \tag{4.3.10}$$

In order to obtain ρ_B, consider the discretized Poisson equation applied to the innermost cell $n = 0$ with the substitution of the value of the potential at the boundary in terms of the ghost zone,

$$\begin{aligned}\nabla^2\Phi_0 &= \frac{1}{(\Delta x_0)^2}\left(\Phi_1 - 2\Phi_0 + \Phi_{-1}\right)\\ &= \frac{1}{(\Delta x_0)^2}\left[\Phi_1 - 2\Phi_0 + (2\Phi_{-1/2} - \Phi_0)\right].\end{aligned}$$

Applying the homogeneous boundary condition,

$$4\pi G\left(\rho_0 + \rho_0^B\right) = \frac{1}{(\Delta x_0)^2}\left(\Phi_1 - 2\Phi_0 + \Phi_{-1} + 2\Phi_{-1/2}\right),$$

we obtain the expression for ρ_0 and ρ_0^B, where

$$\rho_0^B = -\frac{2\Phi_{-1/2}}{4\pi G(\Delta x_0)^2}, \tag{4.3.11}$$

where $\Phi_{-1/2} = \Phi^B(\vec{x})$.

In the following we give the moments of the multipole expansion of the potential (4.3.8) up to $l = 5$ for Cartesian coordinates. For $l = 0$,

$$Y_{00} = \frac{1}{2}\sqrt{\frac{1}{\pi}}, \qquad -\Phi_{l=0} = \frac{G}{r}\int d^3\vec{x}'\rho(\vec{x}'),$$

for $l = 1$,

$$\begin{aligned}Y_{10} &= \frac{1}{2}\sqrt{\frac{3}{\pi}}\frac{z}{r}, \qquad Y_{11} = -\sqrt{\frac{3}{2\pi}}\frac{(x+iy)}{2r}\\ -\Phi_{l=1} &= \frac{Gx}{r^3}\int d^3\vec{x}'\rho(\vec{x}')x' + \frac{Gy}{r^3}\int d^3\vec{x}'\rho(\vec{x}')y' + \frac{Gz}{r^3}\int d^3\vec{x}'\rho(\vec{x}')z',\end{aligned} \tag{4.3.12}$$

for $l=2$,

$$\begin{aligned}
Y_{20} &= -\sqrt{\frac{5}{\pi}}\frac{\left(r^2-3z^2\right)}{4r^2}, \qquad Y_{21}=-\sqrt{\frac{15}{2\pi}}\frac{z(x+iy)}{2r^2}, \qquad Y_{22}=\sqrt{\frac{15}{2\pi}}\frac{(x+iy)^2}{4r^2}, \\
-\Phi_{l=2} &= \frac{G\left(r^2-3z^2\right)}{4r^5}\int d^3\vec{x}'\rho(\vec{x}')\left(r'^2-3z'^2\right)+\frac{3G\left(x^2-y^2\right)}{4r^5}\int d^3\vec{x}'\rho(\vec{x}')\left(x'^2-y'^2\right) \\
&\quad +\frac{3Gxz}{r^5}\int d^3\vec{x}'\rho(\vec{x}')x'z'+\frac{3Gyz}{r^5}\int d^3\vec{x}'\rho(\vec{x}')y'z'+\frac{3Gxy}{r^5}\int d^3\vec{x}'\rho(\vec{x}')x'y', \qquad (4.3.13)
\end{aligned}$$

for $l=3$,

$$\begin{aligned}
Y_{30} &= \sqrt{\frac{7}{\pi}}\frac{\left(5z^3-3r^2z\right)}{4r^3}, \qquad Y_{31}=\sqrt{\frac{21}{\pi}}\frac{\left(r^2-5z^2\right)(x+iy)}{8r^3}, \\
Y_{32} &= \sqrt{\frac{105}{2\pi}}\frac{z(x+iy)^2}{4r^3}, \qquad Y_{33}=-\sqrt{\frac{35}{\pi}}\frac{(x+iy)^3}{8r^3}, \\
-\Phi_{l=3} &= \frac{Gz\left(3r^2-5z^2\right)}{4r^7}\int d^3\vec{x}'\rho(\vec{x}')z'\left(3r'^2-5z'^2\right)+\frac{3Gx\left(r^2-5z^2\right)}{8r^7}\int d^3\vec{x}'\rho(\vec{x}')x'\left(r'^2-5z'^2\right) \\
&\quad +\frac{3Gy\left(r^2-5z^2\right)}{8r^7}\int d^3\vec{x}'\rho(\vec{x}')y'\left(r'^2-5z'^2\right)+\frac{15Gz\left(x^2-y^2\right)}{4r^7}\int d^3\vec{x}'\rho(\vec{x}')z'\left(x'^2-y'^2\right) \\
&\quad +\frac{15Gxyz}{r^7}\int d^3\vec{x}'\rho(\vec{x}')x'y'z'+\frac{5Gx\left(x^2-3y^2\right)}{8r^7}\int d^3\vec{x}'\rho(\vec{x}')x'\left(x'^2-3y'^2\right) \\
&\quad +\frac{5Gy\left(3x^2-y^2\right)}{8r^7}\int d^3\vec{x}'\rho(\vec{x}')y'\left(3x'^2-y'^2\right), \qquad (4.3.14)
\end{aligned}$$

for $l=4$,

$$
\begin{aligned}
Y_{40} &= \frac{1}{\sqrt{\pi}}\frac{3\left(3r^4-30r^2z^2+35z^4\right)}{16r^4}, \qquad\qquad Y_{41}=\sqrt{\frac{5}{\pi}}\frac{3\left(3r^2z-7z^3\right)(x+iy)}{8r^4},\\
Y_{42} &= -\sqrt{\frac{5}{2\pi}}\frac{3\left(r^2-7z^2\right)(x+iy)^2}{8r^4}, \qquad\qquad Y_{43}=-\frac{3\sqrt{\frac{35}{\pi}}z(x+iy)^3}{8r^4},\\
Y_{44} &= \sqrt{\frac{35}{2\pi}}\frac{3(x+iy)^4}{16r^4},\\
-\Phi_{l=4} &= \frac{G\left(3r^4-30r^2z^2+35z^4\right)}{64r^9}\int d^3\vec{x}'\rho(\vec{x}')\left(3r'^4-30r'^2z'^2+35z'^4\right)\\
&\quad+\frac{5Gx\left(3r^2-7z^2\right)}{8r^9}\int d^3\vec{x}'\rho(\vec{x}')x'zz'\left(3r'^2-7z'^2\right)\\
&\quad+\frac{5Gy\left(3r^2-7z^2\right)}{8r^9}\int d^3\vec{x}'\rho(\vec{x}')y'zz'\left(3r'^2-7z'^2\right)\\
&\quad+\frac{5G\left(r^2-7z^2\right)\left(x^2-y^2\right)}{16r^9}\int d^3\vec{x}'\rho(\vec{x}')\left(r'^2-7z'^2\right)\left(x'^2-y'^2\right)\\
&\quad+\frac{5Gxy\left(r^2-7z^2\right)}{4r^9}\int d^3\vec{x}'\rho(\vec{x}')x'y'\left(r'^2-7z'^2\right)\\
&\quad+\frac{35Gz\left(x^3-3xy^2\right)}{8r^9}\int d^3\vec{x}'\rho(\vec{x}')z'\left(x'^3-3x'y'^2\right)\\
&\quad+\frac{35Gz\left(y^3-3x^2y\right)}{8r^9}\int d^3\vec{x}'\rho(\vec{x}')z'\left(y'^3-3x'^2y'\right)\\
&\quad+\frac{35G\left(x^4-6x^2y^2+y^4\right)}{64r^9}\int d^3\vec{x}'\rho(\vec{x}')\left(x'^4-6x'^2y'^2+y'^4\right)\\
&\quad+\frac{35Gxy(x^2-y^2)}{4r^9}\int d^3\vec{x}'\rho(\vec{x}')x'y'(x'^2-y'^2)
\end{aligned}
\tag{4.3.15}
$$

and for $l = 5$,

$$
\begin{aligned}
Y_{50} &= \sqrt{\frac{11}{\pi}}\frac{\left(15r^4z - 70r^2z^3 + 63z^5\right)}{16r^5}, \\
Y_{51} &= -\sqrt{\frac{165}{2\pi}}\frac{\left(r^4 - 14r^2z^2 + 21z^4\right)(x+iy)}{16r^5}, \\
Y_{52} &= -\sqrt{\frac{1155}{2\pi}}\frac{z\left(r^2(x+iy)^2 - 3z^2\left(x^2 + ixy - y^2\right)\right)}{8r^5}, \\
Y_{53} &= \frac{\sqrt{\frac{385}{\pi}}\left(r^2 - 9z^2\right)(x+iy)^3}{32r^5}, \\
Y_{54} &= \frac{3\sqrt{\frac{385}{2\pi}}z(x+iy)^4}{16r^5}, \qquad Y_{55} = -\frac{3\sqrt{\frac{77}{\pi}}(x+iy)^5}{32r^5}, \\
-\Phi_{l=5} &= \frac{Gz\left(15r^4 - 70r^2z^2 + 63z^4\right)}{64r^{11}}\int d^3\vec{x}'\rho(\vec{x}')z'\left(15r'^4 - 70r'^2z'^2 + 63z'^4\right) \\
&+\frac{15Gx\left(r^4 - 14r^2z^2 + 21z^4\right)}{64r^{11}}\int d^3\vec{x}'\rho(\vec{x}')x'\left(r'^4 - 14r'^2z'^2 + 21z'^4\right) \\
&+\frac{15Gy\left(r^4 - 14r^2z^2 + 21z^4\right)}{64r^{11}}\int d^3\vec{x}'\rho(\vec{x}')y'\left(r'^4 - 14r'^2z'^2 + 21z'^4\right) \\
&+\frac{105Gz\left(r^2 - 3z^2\right)\left(x^2 - y^2\right)}{16r^{11}}\int d^3\vec{x}'\rho(\vec{x}')z'(x'^2 - y'^2)\left(r'^2 - 3z'^2\right) \\
&+\frac{105Gxy\left(2r^2z - 3z^3\right)}{16r^{11}}\int d^3\vec{x}'\rho(\vec{x}')x'y'\left(2r'^2z' - 3z'^3\right) \\
&+\frac{35G\left(r^2 - 9z^2\right)\left(x^3 - 3xy^2\right)}{128r^{11}}\int d^3\vec{x}'\rho(\vec{x}')\left(r'^2 - 9z'^2\right)\left(x'^3 - 3x'y'^2\right) \\
&+\frac{315Gz\left(x^4 - 6x^2y^2 + y^4\right)}{64r^{11}}\int d^3\vec{x}'\rho(\vec{x}')z'\left(x'^4 - 6x'^2y'^2 + y'^4\right) \\
&+\frac{315Gxyz(x^2 - y^2)(x'^2 - y'^2)}{4r^{11}}\int d^3\vec{x}'\rho(\vec{x}')x'y'z' \\
&+\frac{63G\left(x^5 - 10x^3y^2 + 5xy^4\right)}{128r^{11}}\int d^3\vec{x}'\rho(\vec{x}')\left(x'^5 - 10x'^3y'^2 + 5x'y'^4\right) \\
&+\frac{63G\left(5x^4y - 10x^2y^3 + y^5\right)}{128r^{11}}\int d^3\vec{x}'\rho(\vec{x}')\left(5x'^4y' - 10x'^2y'^3 + y'^5\right). \qquad (4.3.16)
\end{aligned}
$$

We have taken this expansion to $l = 5$ as we expect the distortion of the star to be at most to $l = 3$. As we will see later in our test problem, this is a sufficient number of multipole moments for our second-order method to converge appropriately.

We may write a parallel code for the Poisson solver by noting that the three-dimensional transform (4.3.5) and its inverse (4.3.6) are computed in one dimension at each step. One step of the partial sum may be computed along one dimension while data in another dimension is scattered across the processors. We then apply a transpose of the data and transform the other dimension.

4.3.5 Numerical test: distorted density fields with analytical solutions

To test the Poisson solver, a density function with an analytical solution for Φ is chosen. The order of the derivative at which this function is discontinuous should be one higher order than the order of desired convergence for the method [76]. Our method is likely no better than second-order convergent since the boundary condition is derived using a second-order approximation for the Laplacian. We consider test densities of the form

$$\rho = r^l \left(1 - r^2\right)^3 P_l(\cos\gamma), \qquad \text{for } r < 1, \tag{4.3.17}$$

and $\rho = 0$, otherwise. The solution should converge to fourth-order. Consider the following densities and analytically derived potentials,

$$\begin{aligned}
\rho_0 &= \left(1 - r^2\right)^3 P_0(\cos\gamma), \\
\Phi_0^i &= -\frac{\pi}{630}\left(35r^8 - 180r^6 + 378r^4 - 420r^2 + 315\right) P_0(\cos\gamma), \qquad \Phi_0^o = -\frac{64\pi}{315r} P_0(\cos\gamma), \\
\rho_1 &= r\left(1 - r^2\right)^3 P_1(\cos\gamma), \\
\Phi_1^i &= \pi\left(-\frac{r^9}{22} + \frac{2r^7}{9} - \frac{3r^5}{7} + \frac{2r^3}{5} - \frac{r}{6}\right) P_1(\cos\gamma), \qquad \Phi_1^o = -\frac{64\pi}{3465r^2} P_1(\cos\gamma), \\
\rho_2 &= r^2\left(1 - r^2\right)^3 P_2(\cos\gamma), \\
\Phi_2^i &= \pi\left(-\frac{r^{10}}{26} + \frac{2r^8}{11} - \frac{r^6}{3} + \frac{2r^4}{7} - \frac{r^2}{10}\right) P_2(\cos\gamma), \qquad \Phi_2^o = -\frac{64\pi}{15015r^3} P_2(\cos\gamma), \\
\rho_3 &= r^3\left(1 - r^2\right)^3 P_3(\cos\gamma), \\
\Phi_3^i &= \pi\left(-\frac{r^{11}}{30} + \frac{2r^9}{13} - \frac{3r^7}{11} + \frac{2r^5}{9} - \frac{r^3}{14}\right) P_3(\cos\gamma), \qquad \Phi_3^o = -\frac{64\pi}{45045r^4} P_3(\cos\gamma), \\
\rho_4 &= r^4\left(1 - r^2\right)^3 P_4(\cos\gamma), \\
\Phi_4^i &= \pi\left(-\frac{r^{12}}{34} + \frac{2r^{10}}{15} - \frac{3r^8}{13} + \frac{2r^6}{11} - \frac{r^4}{18}\right) P_4(\cos\gamma), \qquad \Phi_4^o = -\frac{64\pi}{109395r^5} P_4(\cos\gamma), \\
\rho_5 &= r^5\left(1 - r^2\right)^3 P_5(\cos\gamma), \\
\Phi_5^i &= \pi\left(-\frac{r^{13}}{38} + \frac{2r^{11}}{17} - \frac{r^9}{5} + \frac{2r^7}{13} - \frac{r^5}{22}\right) P_5(\cos\gamma), \qquad \Phi_5^o = -\frac{64\pi}{230945r^6} P_5(\cos\gamma).
\end{aligned}$$

We perform the following tests which should result in at least second-order convergence:

1. For each l, solve for the density, ρ_l, using the associated analytical solution, Φ_l^o, to construct the image mass.

2. Same as (1), but using the multipole expansion Φ_l^{mp} to construct the image mass.

3. Consider the sum of the densities, $\rho_{tot} = \sum_l c_l \rho_l$, where c_l is chosen so that the $l = 0$ density

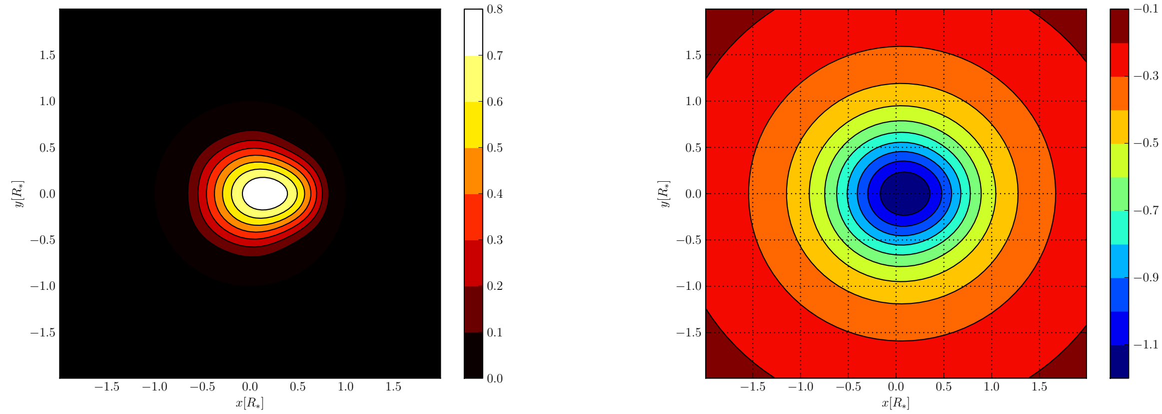

Figure 4.4: Test density and analytical potential for Poisson solver. We obtain an analytical solution to a density $\rho_{tot} = \sum_l c_l \rho_l$ where c_l is chosen so that $\rho_{l=0}$ does not contribute significantly.

does not contribute significantly. Solve for the density, ρ_l, using the associated analytical solution, Φ_l^o, to construct the image mass.

4. Consider the sum of the densities, $\rho_{tot} = \sum_l c_l \rho_l$, where c_l is chosen so that the $l = 0$ density does not contribute significantly. Solve for the density, ρ_l, using the multipole expansion, Φ_l^{mp}, to construct the image mass.

Computing for $\cos\gamma = \{x/r, y/r, z/r\}$ will yield the same results. In the following, we have results of Test 4 for $\cos\gamma = x/r$ with constants c_l given by

$$c_0 = 0.75, \quad c_1 = 0.5, \quad c_2 = 0.75, \quad c_3 = 1.0, \quad c_4 = 1.0, \quad c_5 = 1.0. \tag{4.3.18}$$

We show the density and analytical potential for this test problem in Figure 4.4.

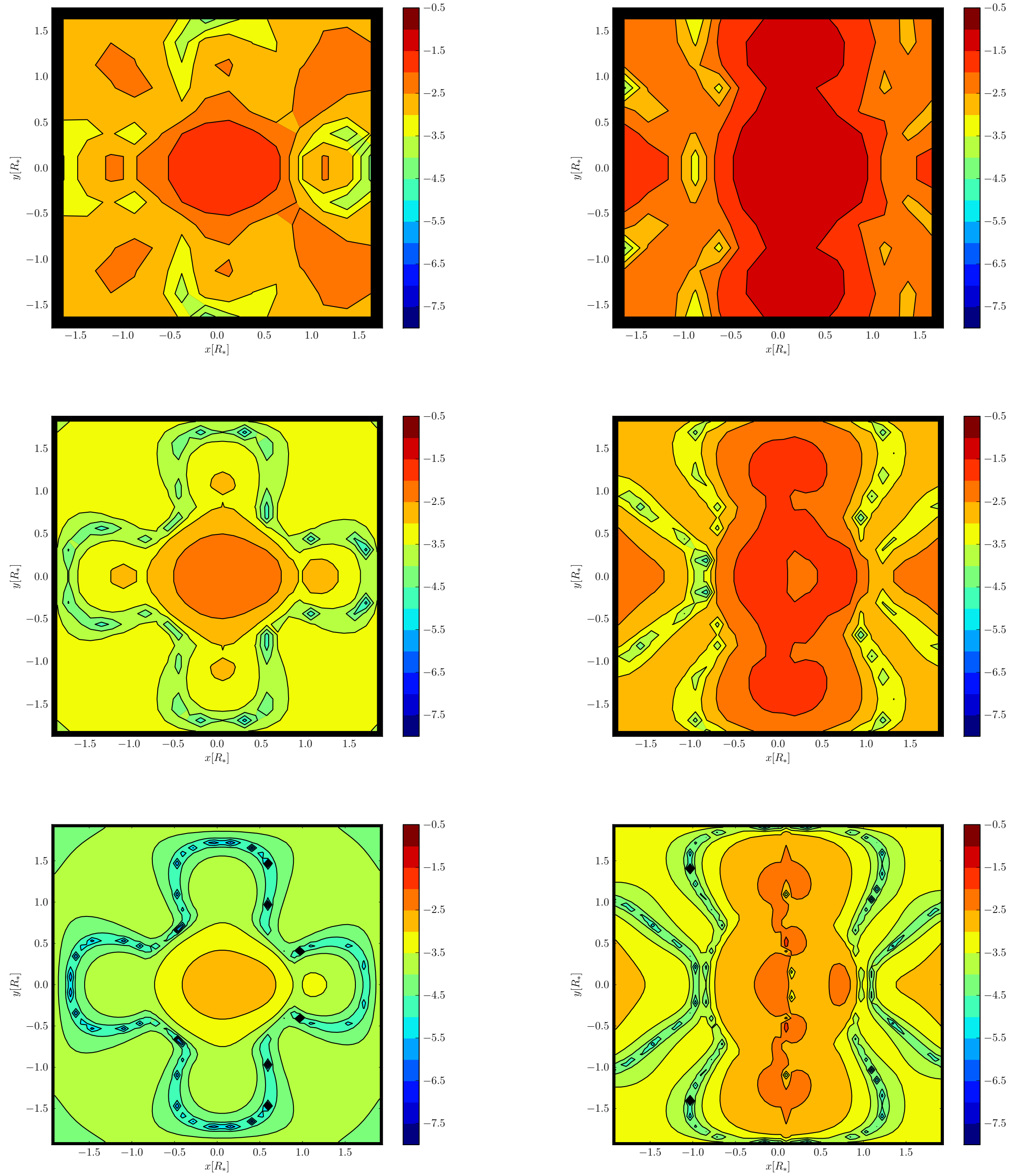

Figure 4.5: Relative error between the analytical and computed gravitational potential. Results are given in the xy-plane.

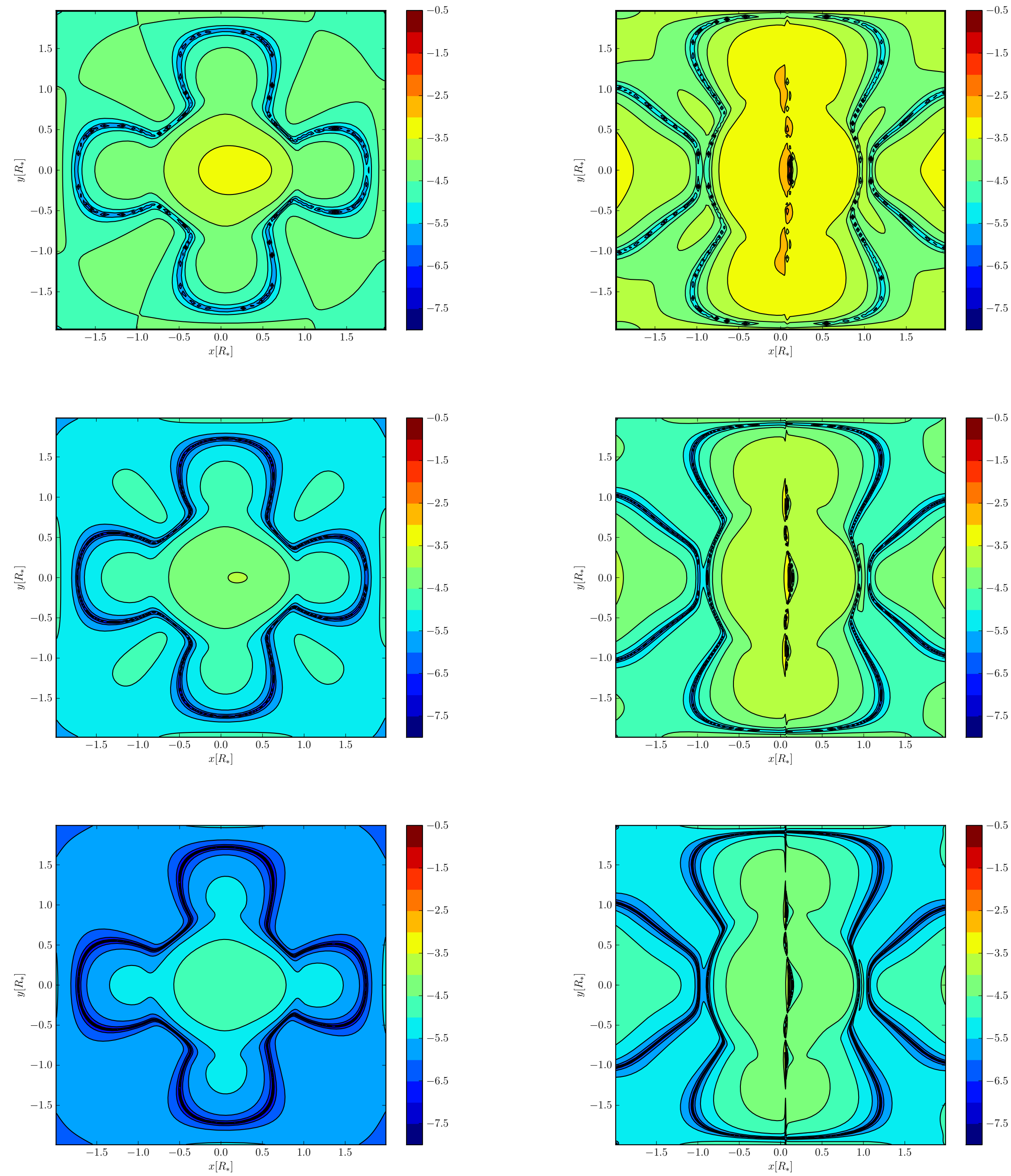

Figure 4.6: Relative error in the x-derivative of the gravitational potential. Results are given in the xy-plane.

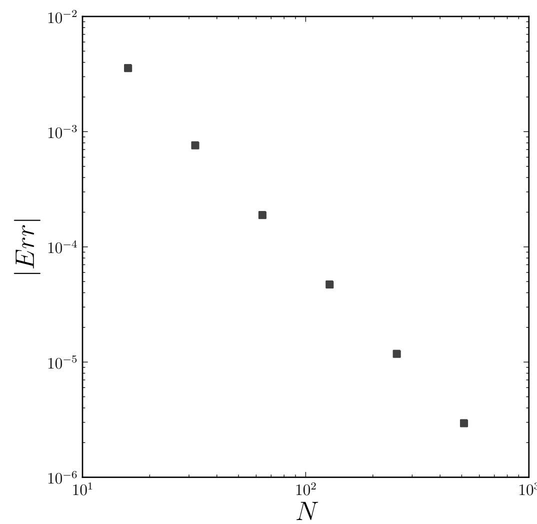

Figure 4.7: L_2 error between the analytical and computed solution. Results are given for different zones, N, in one direction where N^3 is the total number of zones in the computational domain. The Poisson solver method exhibits second order convergence.

The L_2, or root-mean-square error, is defined as

$$\mathrm{Err}[\mathrm{f}^{\mathrm{analytical}}, \mathrm{f}^{\mathrm{computed}}] = \sqrt{\frac{1}{\mathrm{IJK}} \sum_{\mathrm{ijk}} |\mathrm{f}^{\mathrm{analytical}}_{\mathrm{ijk}} - \mathrm{f}^{\mathrm{computed}}_{\mathrm{ijk}}|^2}. \tag{4.3.19}$$

In Table 4.1 and Figure 4.7, we show that the method exhibits second order convergence for the L_2 error between the analytically computed solution to the self-gravitational potential.

N^3	L_2
16^3	3.56531726783 E-3
32^3	7.61089631365 E-4
64^3	1.88954840925 E-4
128^3	4.71658287748 E-5
256^3	1.17893020983 E-5
512^3	2.94715758706 E-6

Table 4.1: Second-order convergence of Poisson solver. We give the L_2 error between the analytical and computed solution to the self-gravitational potential.

We show the error in the xy-plane in the gravitational potential (Figure 4.5) and the derivative of the potential in the x-direction (Figure 4.6).

4.4 Tidal module

In this section, we give the numerical method to calculate the tidal interaction due to the black hole. We compute the tidal interaction with the $l = 2$ and $l = 3$ tidal terms. We use a fourth-order Runge-Kutta method to integrate the first-order geodesic equations, parameterized using the Darwin method, from Chapter 3. We choose the periastron distance, R_p and the type of encounter η and obtain the initial values for the semi-latus rectum p, the eccentricity e, the specific orbital energy E, and specific orbital angular momenum L. Thus, the following equations are integrated with respect to proper time: for the radial phase,

$$\frac{d\chi}{d\tau} = \left[\frac{p^{3/2}M}{(1+e\cos\chi)^2}\left(\frac{p-3-e^2}{p-6-2e\cos\chi}\right)^{1/2}\right]^{-1}, \tag{4.4.1}$$

and the FNC frame rotation angle,

$$\frac{d\Psi}{d\tau} = \frac{EL}{r^2+L^2}. \tag{4.4.2}$$

From the radial phase, we have the orbital radius as a function of proper time,

$$R[\chi(\tau)] = \frac{pM}{1+e\cos\chi(\tau)}. \tag{4.4.3}$$

Using $R(\tau)$ and $\Psi(\tau)$, we compute the tidal acceleration using the tidal tensors C_{ij} and C_{ijk} and the tidal potential Φ_{tidal} (3.5.30) at each time step. The accelerations due to the quadrupole term are then

$$\begin{aligned}
\frac{\partial}{\partial x}\Phi^{\text{tidal}}_{l=2} &= C_{11}x + C_{13}y, && (4.4.4)\\
\frac{\partial}{\partial y}\Phi^{\text{tidal}}_{l=2} &= C_{13}x + C_{33}y, && (4.4.5)\\
\frac{\partial}{\partial z}\Phi^{\text{tidal}}_{l=2} &= C_{22}z, && (4.4.6)
\end{aligned}$$

and the octupole term are

$$\begin{aligned}
\frac{\partial}{\partial x}\Phi^{\text{tidal}}_{l=3} &= \tfrac{1}{2}\left(C_{111}x^2 + 2C_{131}xy + C_{133}y^2 + C_{122}z^2\right), && (4.4.7)\\
\frac{\partial}{\partial y}\Phi^{\text{tidal}}_{l=3} &= \tfrac{1}{2}\left(C_{131}x^2 + 2C_{133}xy + C_{333}y^2 + C_{322}z^2\right), && (4.4.8)\\
\frac{\partial}{\partial z}\Phi^{\text{tidal}}_{l=3} &= C_{122}xz + C_{322}yz. && (4.4.9)
\end{aligned}$$

In this chapter, we have given the principal parts of the numerical method. We now apply the method to calculate the relativistic tidal interaction between a white dwarf and a Schwarzschild black hole in the next chapter.

Chapter 5

White Dwarf–Intermediate Mass Black Hole Encounters

We now apply the analytic and numerical method outlined in previous chapters to tidal interactions between a white dwarf and an intermediate mass black hole ($M \sim 10^3 - 10^5 M_\odot$). With this method, we study encounters at the threshold of disruption and weaker encounters that partially strip the star or excite it into oscillations. In the first section, we first present the initial models of the white dwarf for the simulations. We then describe a control simulation for the encounters –a star in hydrostatic equilibrium. Next we present the results for encounters in the regime of weak tidal interactions ($\eta = 4 - 6$). We also examine stronger, disruptive encounters with $\eta = 1 - 3$. These results are compared with predictions from the linear theory. We focus on the amount of energy and spin angular momentum deposited on the star. We show a difference in the energy deposition for relativistic encounters and the predicted amount according to the linear theory.

5.1 Initial models

The simulated white dwarf star is assumed to be a polytrope and at rest. We solve the 1D Lane-Emden equation of polytropic index n to obtain the initial density and pressure radial profiles for the star. The results are then mapped onto a 3D Cartesian grid. We consider an $n = 1.5$ polytrope with properties [50]

$$\xi_1 = 3.6537, \qquad \left.\frac{d\theta}{d\xi}\right|_{\xi=\xi_1} = -0.2033, \qquad \left[\frac{\xi}{3}\frac{1}{d\theta/d\xi}\right]_{\xi=\xi_1} = -5.9907 \tag{5.1.1}$$

and equation of state $p = \kappa\rho^{1+1/n}$. The central density and pressure may be expressed as [46]

$$\rho_c = -\left[\frac{\xi}{3}\frac{1}{d\theta/d\xi}\right]_{\xi=\xi_1}\bar{\rho}, \qquad \bar{\rho} = \frac{3M_*}{4\pi R_*^3},$$

$$p_c = W\frac{GM_*^2}{R_*^4}, \qquad W = \left[10\pi\left(\frac{d\theta}{d\xi}\right)^2\Big|_{\xi=\xi_1}\right]^{-1} = 0.7701.$$

The fundamental radial pulsation period is given by $\Pi = 2\pi\sqrt{R_*^3/(\alpha M_*)}$, where $\alpha = 2.712$ for an $n = 1.5$ polytrope [52], with specific heat ratio $\gamma = 5/3$. We choose a mass M_* and a radius R_* for the star and then obtain values for the constant κ, the central density ρ_c, and the central pressure p_c.

	CGS
M_*	$0.64 M_\odot$
R_*	8.62×10^8 cm
L_*	3.44×10^{50} g cm^2/s
I_*	9.67×10^{49} g cm^2
Φ_*	1.10×10^{-4}
ρ_c	2.84×10^6 g/cm^3
p_c	1.51×10^{23}ergs/cm^3
τ_0	10.5 s
E_g	-1.08×10^{50} ergs
E_{int}	5.37×10^{49} ergs
E_{tot}	-5.37×10^{49} ergs

Table 5.1: Properties of the star in CGS units: mass of the star, M_*; radius of the star, R_*; spin angular momentum scale, $L_* = \sqrt{GM_*^3 R_*}$; moment of inertia, $I_* = \frac{1}{3}\int x_i x_i \rho d$; dimensionless stellar potential, $\Phi_* = (G/c^2)M_*/R_*$; central density, ρ_c; central pressure, p_c; fundamental radial oscillation period of the star, τ_0; gravitational energy, E_g; internal energy, E_{int}; total energy, $E_{tot} = E_g + E_{int}$.

μ	1.28×10^{-3}	4.21×10^{-4}	3.77×10^{-5}
M_*	1.28×10^{-3} M	4.21×10^{-4} M	3.77×10^{-5} M
R_*	11.7 M	3.84 M	0.344 M
L_*	1.56×10^{-4} M^2	1.69×10^{-5} M^2	1.36×10^{-7} M^2
I_*	1.78×10^{-2} M^3	6.35×10^{-4} M^3	4.56×10^{-7} M^3
Φ_*	1.10×10^{-4}	1.10×10^{-4}	1.10×10^{-4}
ρ_c	1.15×10^{-6} M^{-2}	1.06×10^{-5} M^{-2}	1.33×10^{-3} M^{-2}
p_c	6.80×10^{-11} M^{-2}	6.28×10^{-10} M^{-2}	7.85×10^{-8} M^{-2}
τ_0	4.25×10^3 M	1.40×10^3 M	1.25×10^2 M
E_g	-1.20×10^{-7} M	-3.96×10^{-8} M	-3.54×10^{-9} M
E_{int}	6.02×10^{-8} M	1.98×10^{-8} M	1.77×10^{-9} M
E_{tot}	-6.02×10^{-8} M	-1.98×10^{-8} M	-1.77×10^{-9} M

Table 5.2: Properties of the star in black hole mass units for different mass ratios, $\mu = M_*/M$, where $\mu = 1.28 \times 10^{-3}, 4.21 \times 10^{-4}$, and 3.77×10^{-5}.

In our work, we choose the mass $M_{\rm wd} = 0.64 M_\odot$ and radius $R_{\rm wd} = 8.62 \times 10^8$ cm. We use an $n = 1.5$ polytrope model instead of a full realistic white dwarf equation of state. For a non-relativistic completely degenerate white dwarf equation of state (2.2.18) [47], we have that $\kappa = 1.0036 \times 10^{13}/\mu_e^{5/3} = 3.1611 \times 10^{12}$, if the mean molecular weight per electron is $\mu_e = 2$. If we use this for the polytropic model, the radius in terms of mass is then given by $R_* = 1.1167 \times 10^{20} M_*^{-1/3}$. For $M_{\rm wd} = 0.64 M_\odot$, $R_{\rm wd,polytrope} = 1.030 \times 10^9$cm. In comparison with our models, there is a 16.3% difference in radius. We also have a difference in the polytropic constant where $\kappa_{\rm wd} = 2.6444 \times 10^{12}$ for our models. We note that the central density is $\rho_c \sim 10^6$g/cm^3, which is the upper limit for reasonably treating the white dwarf as being non-relativistic.

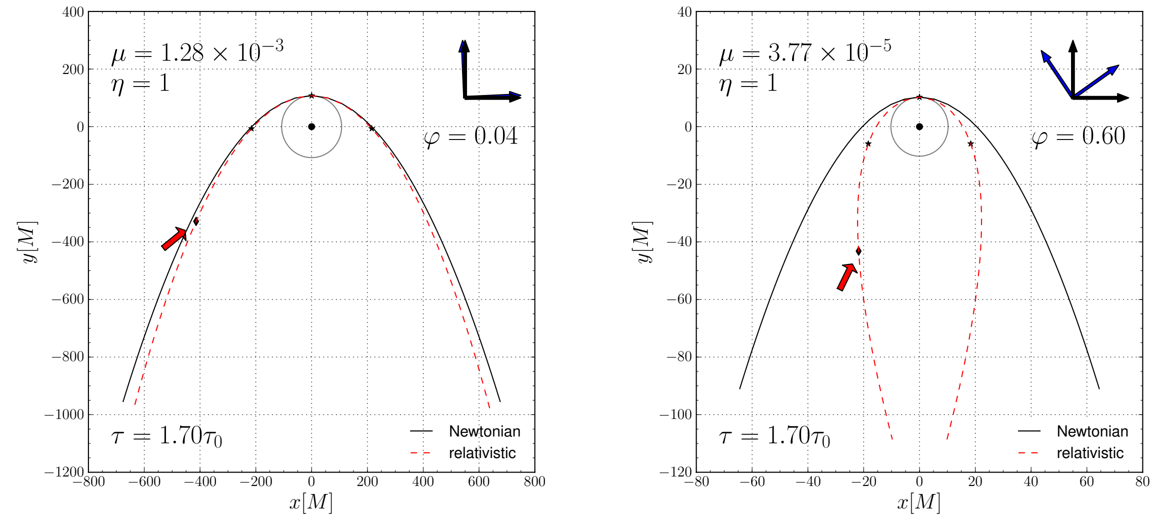

Figure 5.1: Trajectories of the FNC frame for two mass ratios in the black hole frame. The encounter strength is $\eta = 1$ and the mass ratios are $\mu = 1.28 \times 10^{-3}$ and $\mu = 3.77 \times 10^{-5}$. The orbital motion is counter-clockwise. The star marks on the trajectory indicate the radial distances at periastron (center) R_p and at $r = 2R_p$. The diamond mark on the trajectory is the location of the FNC frame at $\tau = 1.70\tau_0$. This is also indicated by the arrow. The ratio of radius of star to periastron distance is much larger for the mass ratio $\mu = 1.28 \times 10^{-3}$ ($R_*/R_p = 0.107$) than for $\mu = 3.77 \times 10^{-5}$ ($R_*/R_p = 0.034$) for encounter strength $\eta = 1$. After the star passes the black hole, the FNC frame is rotated from its original orientation by an angle φ. This is slight for the $\mu = 1.28 \times 10^{-3}$ case and much more pronounced for the $\mu = 3.77 \times 10^{-5}$ case. Plotted along with the relativistic trajectory, for reference, is the Newtonian parabolic orbit with the same periastron distance.

The properties of the white dwarf used in our simulations are given in CGS units in Table 5.1. We simulate encounters between a white dwarf and a black hole with mass ratios $\mu \equiv M_*/M = 1.28 \times 10^{-3}$, 4.21×10^{-4}, and 3.77×10^{-5}. In Table 5.2, the properties of the star are given in terms of black hole mass for the three different cases.

We let the duration of the encounters be equal to ten fundamental radial oscillations of the star, with the star reaching periastron at $\tau = 0$. The motion of the orbit is obtained using the Darwin method given in Section 3.3.1. The Schwarzschild black hole coordinates are $\{t', r', \theta', \phi'\}$. Each encounter is initialized such that at periastron, $r = R_p$, the radial phase is $\chi = 0$. In the FNC frame, the star is at the origin and we can consider the black hole to be orbiting about it with an angle $\Psi(\tau)$. We are allowed to choose initial values for Ψ and ϕ' arbitrarily. We calculate the precession of the frame, φ, using the change in the frame rotation angle $\Delta\Psi = \Psi_f - \Psi_i$ and the azimuthal angle $\Delta\phi = \phi_f - \phi_i$ during the encounter such that $\varphi = \Delta\phi - \Delta\Psi$.

In Figure 5.1, plots of the trajectories of the FNC frame for $\eta = 1$ encounters are given (for

μ	η	$L[M]$	$R_p[M]$	$R_i[M]$	$\Delta\chi$	$\Delta\phi$	$\Delta\Psi$	φ
1.28×10^{-3}	1	14.8	107.5	1167	5.050	5.128	5.083	4.479e-02
-	2	18.6	170.6	1120	4.679	4.725	4.697	2.792e-02
-	3	21.2	223.6	1086	4.399	4.433	4.411	2.115e-02
-	4	23.4	270.9	1060	4.164	4.190	4.173	1.733e-02
-	5	25.2	314.3	1041	3.956	3.978	3.964	1.482e-02
-	6	26.7	354.9	1027	3.769	3.788	3.775	1.300e-02
4.21×10^{-4}	1	10.3	51.2	555.4	5.049	5.216	5.120	9.638e-02
-	2	12.9	81.3	532.8	4.678	4.776	4.716	5.949e-02
-	3	14.7	106.6	516.7	4.397	4.469	4.424	4.490e-02
-	4	16.2	129.1	504.7	4.162	4.218	4.181	3.672e-02
-	5	17.4	149.8	495.6	3.954	4.001	3.970	3.134e-02
-	6	18.5	169.2	488.8	3.767	3.807	3.779	2.746e-02
3.77×10^{-5}	1	5.0	10.2	109.0	5.037	6.103	5.497	6.068e-01
-	2	6.1	16.3	104.9	4.664	5.229	4.890	3.396e-01
-	3	6.9	21.3	101.8	4.382	4.778	4.530	2.475e-01
-	4	7.5	25.8	99.6	4.146	4.452	4.253	1.986e-01
-	5	8.0	30.0	97.9	3.938	4.188	4.020	1.675e-01
-	6	8.5	33.8	96.6	3.750	3.961	3.816	1.455e-01

Table 5.3: Parameters for different types of encounters. For each mass ratio μ and encounter strength η, the following are given: the specific orbital angular momentum $L = 2R_p^2/(R_p - 2M)$, the periastron distance R_p, the initial orbital distance of the star at the beginning of the simulation R_i, the total change of radial phase $\Delta\chi$, azimuthal $\Delta\phi$, frame rotation $\Delta\Psi$, and the total precession of the frame $\varphi = \Delta\phi - \Delta\psi$ during the encounter.

mass ratios $\mu = 1.28 \times 10^{-3}$ and $\mu = 3.77 \times 10^{-5}$) in the black hole frame. The ratio of radius of star to periastron distance is much larger for the mass ratio $\mu = 1.28 \times 10^{-3}$ ($R_*/R_p = 0.107$) than for $\mu = 3.77 \times 10^{-5}$ ($R_*/R_p = 0.034$) for encounter strength $\eta = 1$. At time $\tau = 1.7\tau_0$, the star has passed the black hole and we see that because the frame is parallel transported, the black hole will cause a slight precession φ relative to the distant stars. This frame precession is larger for the $\mu = 3.77 \times 10^{-5}$ orbit, which is considerably more relativistic in that the periastron is closer and the apsidal precession of the orbit is more noticeable. Plotted along with the relativistic trajectory is the Newtonian parabolic orbit with the same periastron distance, for comparison. In Table 5.3, the specific orbital angular momentum, periastron, starting radius on the orbit, and total changes in angles for the encounter are given for different mass ratios and encounter strengths.

An atmosphere surrounding the star ($\rho_{\rm atm}, p_{\rm atm}$), as well as minimum values for the density and pressure ($\rho_{\rm floor}, p_{\rm floor}$), must be specified because PPMLR may only be applied to non-zero hydrodynamic variables. We specify these values by first considering the sound speed at the center of the star, $c_s = \sqrt{\gamma p_c/\rho_c}$, and choosing the sound speed of the atmosphere to be the virial velocity at $2R_*$, $c_{\rm atm} = \sqrt{M_*/(2R_*)}$. We choose the atmospheric density to be $\rho_{\rm atm} = \rho_c \times 10^{-15}$ and it follows that the atmospheric pressure is $p_{\rm atm} = c_{\rm atm}^2 \rho_{\rm atm}/\gamma$. We set the floor density to be $\rho_{\rm floor} = \rho_c \times 10^{-25}$

and obtain the floor pressure using the sound speed of the atmosphere, $p_{\text{floor}} = c^2_{\text{atm}}\rho_{\text{floor}}/\gamma$.

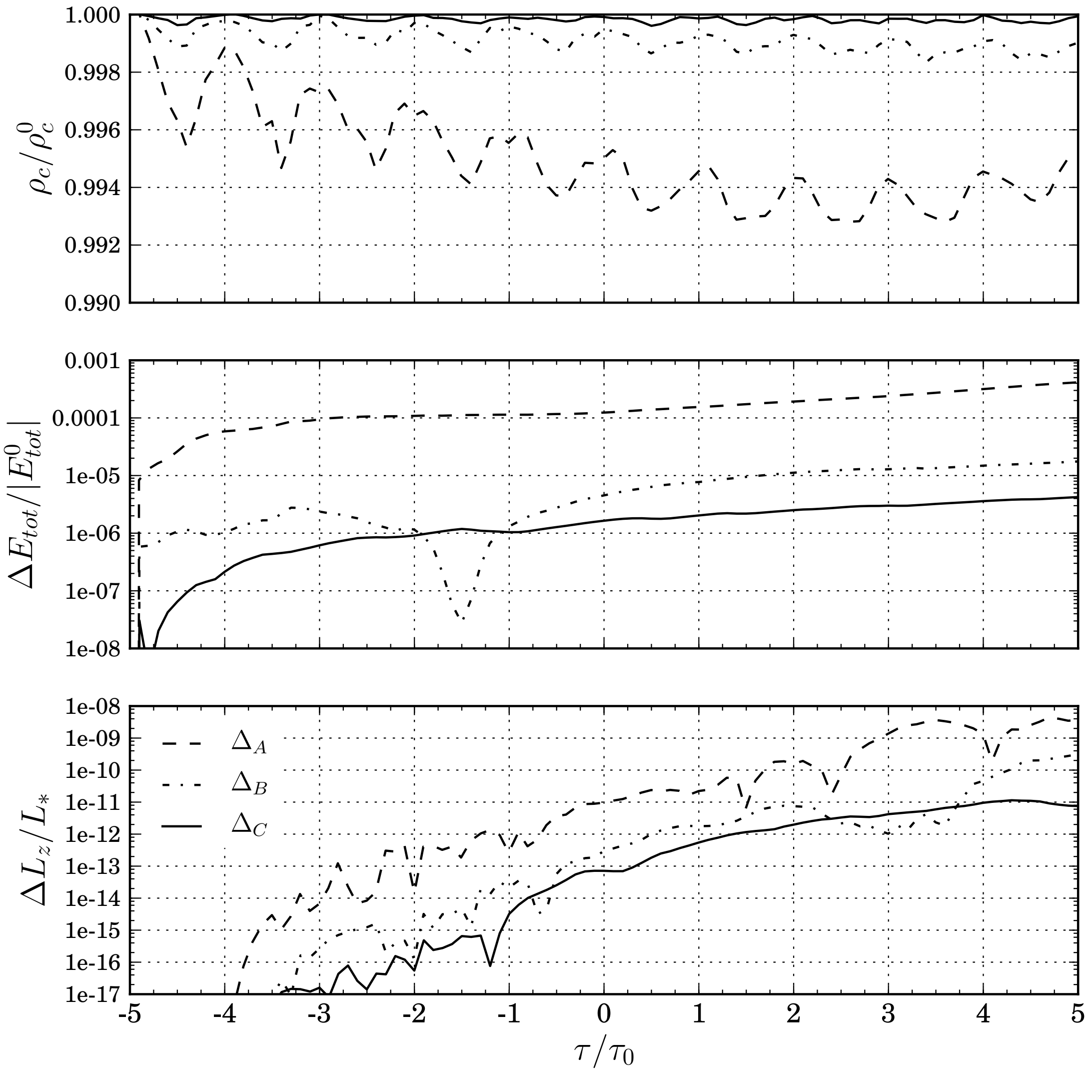

Figure 5.2: Stellar equilibrium model. In the top panel we plot the normalized central density, dividing the central density $\rho(\tau)$ by the initial central density ρ_c^0. In the next panel, we plot the fractional change in total energy using the total energy $E_{\text{tot}}(\tau)$ and the initial total energy E^0_{tot}. In the bottom panel, we plot the change in total z-component of the spin angular momentum using the spin angular momentum $L_z(\tau)$, the initial spin angular momentum L^0_z, and the maximal break-up spin angular momentum L_*. Results are given for three different resolutions: Δ_A, Δ_B, Δ_C.

For all of the simulations, an evenly-spaced Cartesian grid is implemented with 128^3, 256^3, or

512^3 zones. The computational domain for stellar equilibrium and non-disruptive encounters has a length of four times the radius of the star, $L = 4R_*$. For partial and completely disruptive encounters, the domain is taken to be larger, $L = 8R_*$, in order to follow gas that streams off of the star. We use $\alpha = A, B, C$ to denote the resolution, Δ_α, for each simulation: $\Delta_A = R_*/32$, $\Delta_B = R_*/64$, $\Delta_C = R_*/128$. Solid wall or (most often) zero gradient outflow boundary conditions are implemented. The number of computer processors used for each simulation is set to the number of zones in one direction. Thus, at our highest resolution we are using 512 processors.

5.2 Numerical validation of entire code

We test our code by using stellar equilibrium as the control simulation. One may identify three main sources of error in the stellar equilibrium simulation. The first is the discretization error due to mapping the 1D Lane-Emden radial profiles onto a 3D Cartesian grid. The second is due to the nature of the PPM algorithm. Any gradient in density and pressure, even in hydrostatic equilibrium, is viewed by the method as a set of discontinuities or small shocks. This has the effect of generating small spurious increases in entropy. This effect is reduced with higher resolution. The third source of error is due to the accuracy of the Poisson solver in obtaining the self-gravitational field, which also is improved with higher resolution. The overall effect of these errors is to generate small amplitude oscillations of the star in various modes, particularly in the fundamental radial mode. These oscillations tend to damp in amplitude over time. In comparing the use of solid wall and outgoing boundary conditions, simulations with outgoing boundary conditions have a slight advantage in providing less feedback, although the differences are slight.

In the top panel of Figure 5.2, we show the central density versus time for three equilibrium simulations of 128^3, 256^3, and 512^3 zones, and with a domain size of $L = 4R_*$ (Δ_A, Δ_B, and Δ_C) and with outgoing boundary conditions. The models are computed for a period of ten radial oscillations. The dominant behavior is an oscillation in the fundamental radial mode. Note the average decrease over time and the improvement with higher resolution. This downward drift in density is attributed to the spurious entropy generation at the "shock" at each zone interface. We set the lower limit for simulations of physical interest to 32 zones across the radius of the star (e.g.,Δ_A). Total energy and spin-angular momentum conservation at different resolutions is exhibited in the next panels of Figure 5.2. Note the improvement in normalized error with increase in resolution.

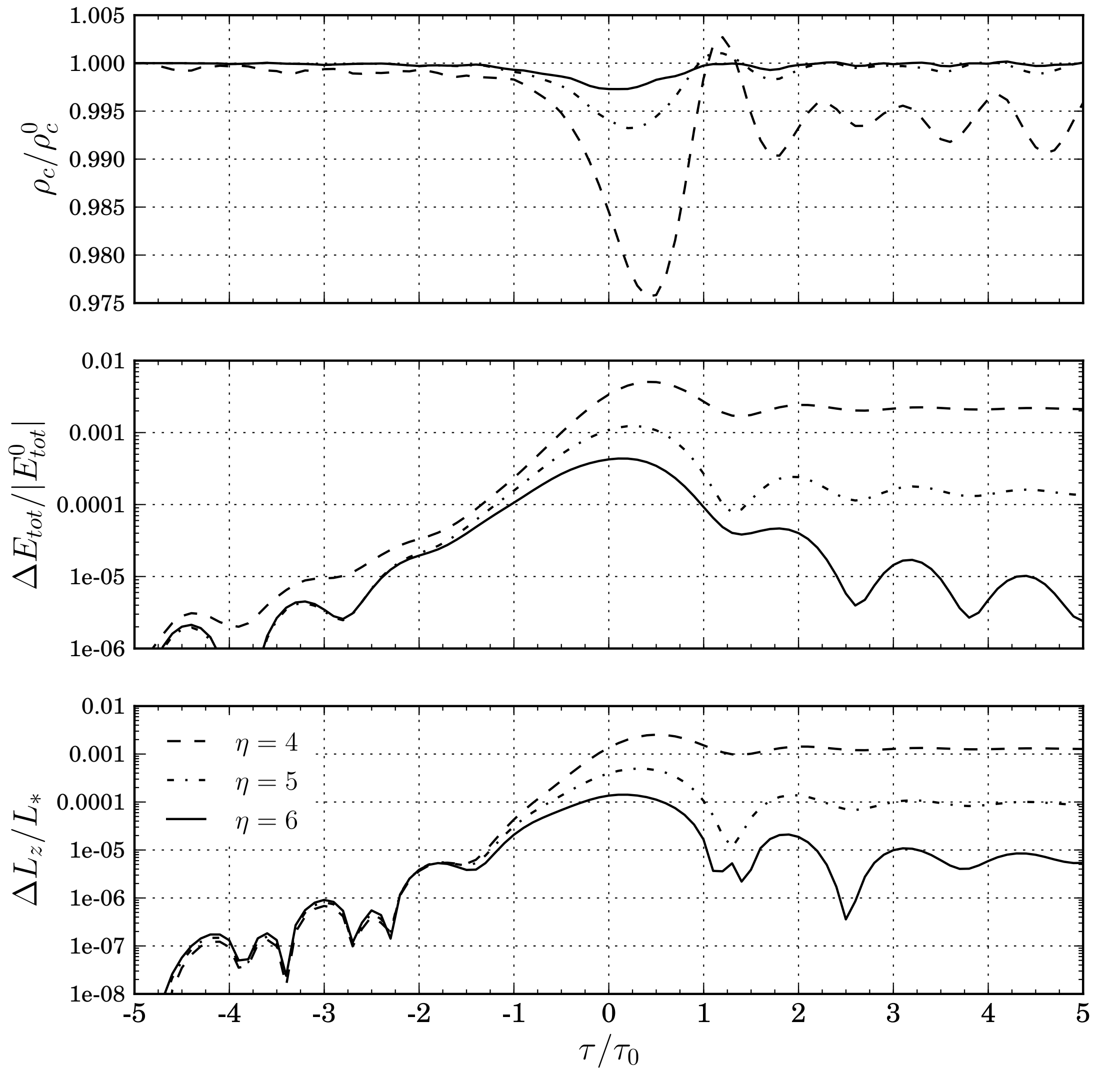

Figure 5.3: Weak tidal encounters. In the top panel, we give the normalized central density for each tidal encounter simulation by subtracting from it the normalized central density for the equilibrium simulation and adding unity ($\rho_c^\eta/\rho_c^0 - \rho_c^{equil}/\rho_c^0 + 1$). In the next panel, we give the total energy deposited on the star for each tidal encounter simulation subtracted by the change in total energy for the equilibrium simulation ($E_{\rm tot}^\eta - E_{tot}^{\rm equil}$) and divide by the magnitude of the initial total energy $|E_{tot}^0|$. In the bottom panel, we give the total z-component of the spin angular momentum deposited on the star for each tidal encounter simulation subtracted by the change in total z-component of the spin angular momentum for the equilibrium simulation ($L_z^\eta - L_z^{equil}$). Results are given at the highest resolution, Δ_C.

In this section, we present the results of tidal interactions between a white dwarf and a black hole in the non-disruptive limit ($\eta = 4, 5, 6$) and at the threshold of disruption ($\eta = 1, 2, 3$). The amount of CPU time for each type of simulation at different resolutions is given in Table 5.4.

model	$L[R_*]$	Resol.	N_p	Processor hours	Wall clock (hr)
$\eta = 1$	8	Δ_A	256	2.6×10^3	10.4
	8	Δ_B	512	6.5×10^4	127.0
$\eta = 2$	8	Δ_A	256	9.8×10^2	3.8
	8	Δ_B	512	4.6×10^4	89.7
$\eta = 3$	8	Δ_A	256	3.0×10^3	11.6
	8	Δ_B	512	4.5×10^4	87.5
$\eta = 4$	4	Δ_A	128	2.4×10^2	1.9
	4	Δ_B	256	3.3×10^3	12.8
	4	Δ_C	512	5.9×10^4	115.5
$\eta = 5$	4	Δ_A	128	1.4×10^2	1.1
	4	Δ_B	256	3.0×10^3	11.6
	4	Δ_C	512	6.2×10^4	121.2
$\eta = 6$	4	Δ_A	128	3.1×10^2	2.4
	4	Δ_B	256	2.7×10^3	10.7
	4	Δ_C	512	5.8×10^4	113.6
equilibrium	4	Δ_A	128	5.8×10^1	0.45
	4	Δ_B	256	1.7×10^3	6.5
	4	Δ_C	512	4.7×10^4	92.6

Table 5.4: Wall clock time for simulating stellar equililbrium and $\eta = 1 - 6$ encounters. We use $l = 2$ and $l = 3$ tidal terms in the relativistic tidal field. Results are given for different resolutions where N_p denotes the number of processors and L denotes the length of the computational domain in terms of the radius of the star.

5.3.1 Weak tidal encounters

We apply the numerical method first to $\eta = 4, 5, 6$ encounters, during which the star does not disrupt, with a WD-BH mass ratio $\mu = 1.28 \times 10^{-3}$. We use 128^3, 256^3, and 512^3 zones for a domain size of $L = 4R_*$ (Δ_A, Δ_B, and Δ_C). We implement solid wall boundary conditions in order to calculate the change in total energy and spin angular momentum in a straightforward manner. We consider the tidal expansion up through the octupole ($l = 3$) tidal term. We will calculate the effects of $l = 4$ in a future study. We have made attempts to see the gravitomagnetic effect in these simulations. At the resolutions so far considered, these effects are too small to see. The top panel of Figure 5.3 gives the normalized central density for each weak encounter. The weak tidal interaction perturbs the star, causing it to oscillate but not disrupt. The next panel gives the fractional change in total energy and the bottom panel gives the fractional change in spin-angular momentum deposited onto the star for these weak encounters.

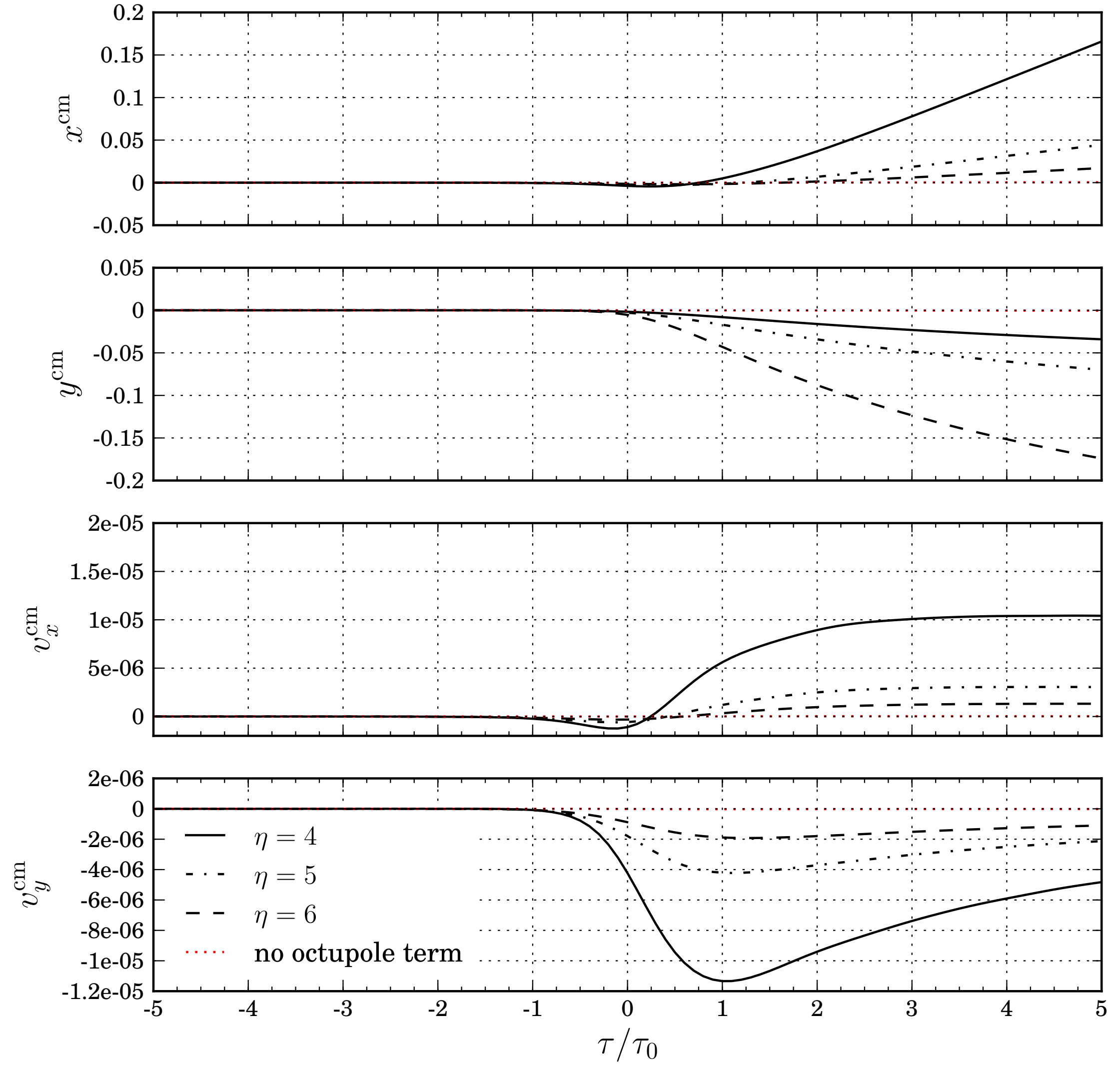

Figure 5.4: Deflection of the center of mass off of the origin of the FNC. Results are given for simulations of $\eta = 4, 5, 6$ encounters with mass ratio $\mu = 1.28 \times 10^{-3}$ using only the quadrupole ($l = 2$) tidal term (dotted red line) and simulations with both quadrupole ($l = 2$) and octupole ($l = 3$) tidal terms. The top two panels are plots of the position of the x-coordinate and y-coordinate of the center of mass. The bottom two panels are plots of the x-velocity and y-velocity of the center of mass. Note that the inclusion of the octupole term causes the center of mass of the star to deflect. The resolution of the grids in these simulations is Δ_C.

In our code, we track the position and velocity of the center of mass. We compare simulations where we used only the quadrupole ($l = 2$) tidal term with simulations where we used both the

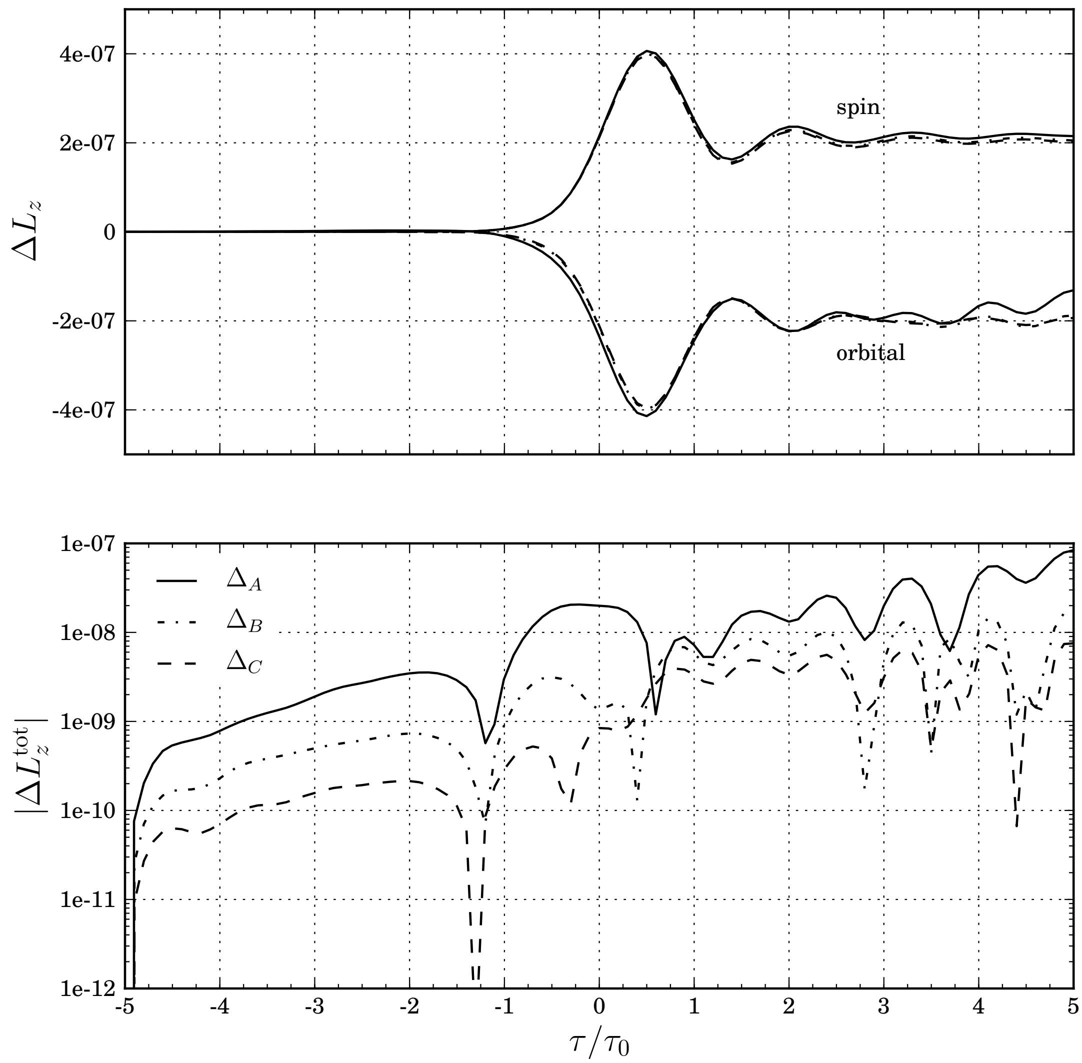

Figure 5.5: Conservation of total angular momentum for Newtonian simulations. The change in orbital and spin angular momentum (top) and the change in total angular momentum (bottom) during a Newtonian simulation of an $\eta = 4$ encounter and mass ratio of $\mu = 1.28 \times 10^{-3}$. Results are given for three different resolutions ($\Delta_A, \Delta_B, \Delta_C$).

quadrupole ($l = 2$) and octupole ($l = 3$) tidal terms. In Figure 5.4, we see that the inclusion of the octupole tidal term causes the center of mass of the star to accelerate away from the origin of the FNC system in the x- and y- directions, in accordance with theoretical expectations.

We relate the change in orbital angular momentum due to the spin-up of the star and the acceleration of the center of mass in a straightforward manner by considering a Newtonian tidal interaction. From (2.3.67), we have that the change in total angular momentum about the z-axis is given by

$$\frac{d}{dt}L_z^{\rm tot} = \frac{d}{dt}L_z^{\rm spin} + \frac{d}{dt}L_z^{\rm orb}. \tag{5.3.1}$$

Given a conservative central force, the total angular momentum, $L_z$tot, will be conserved. Any change in the spin angular momentum of a fluid object must be compensated by a (negative) change in orbital angular momentum. The change in orbital angular momentum can be found from

$$\frac{d}{dt}L_z^{\rm orb} = \frac{d}{dt}\left(D_x V_y^{(0)} - D_y V_x^{(0)} - \dot{D}_x X_y^{(0)} + \dot{D}_y X_x^{(0)}\right), \tag{5.3.2}$$

where $X_k^{(0)}(\tau)$ and $V_k^{(0)}(\tau)$ are the position and velocity of the origin of the moving coordinate system as seen in the black hole frame and D_k and $\dot{D}_k$ are the first mass moment and its derivative defined by

$$D_k \equiv \int_{\mathcal{V}} \rho x_k d^3x, \qquad \dot{D}_k = \int_{\mathcal{V}} \rho v_k d^3x. \tag{5.3.3}$$

In the following, we consider a strictly Newtonian simulation of an $\eta = 4$ encounter and mass ratio of $\mu = 1.28 \times 10^{-3}$ (Newtonian orbit and Newtonian quadrupole and octupole tide). In Figure 5.5, we give the change in orbital and spin angular momenta (top) and the change in total angular momentum (bottom) during the Newtonian simulation. Results are given for three different resolutions ($\Delta_A, \Delta_B, \Delta_C$). We see that the spin up of the star is accompanied by a matching decrease in the orbital angular momentum. This is expected analytically. Thus, the calculation represents a considerable test of the sensitivity of the simulations, since it is the $l = 2$ tide that is primarily responsible for the spin up and it is the $l = 3$ tide that is responsible for the deflection of the fluid center of mass relative to the FNC frame center.

5.3.2 Complete and partial disruptions

For $\eta \leq 3$ encounters, gas streams off the star and out of the computational domain. We track the amounts of mass and energy that leave the grid and include these in our estimate of the total energy and angular momentum deposited onto the star. Furthermore, these simulations are modeled with a larger computational domain, $L = 8R_*$, than the weak encounters in order to contain as much gas streaming off of the star as possible.

In Table 5.5, the amount of mass and energy, normalized by their initial values, is given for $\eta = 1 - 4$ encounters with mass ratio $\mu = 1.28 \times 10^3$. For comparison, we have the amount of

η	Resol.	M_{outflow}/M_*	$E_{\text{outflow}}/(E_{\text{tot}})_0$	$\Delta E^{\text{rel.}}_{l=2,3}/(E_{\text{tot}})_0$
1	Δ_B	7.62282e-01	1.43009	2.417811
2	Δ_B	1.02146e-01	1.00925e-01	4.91648e-01
3	Δ_B	4.81726e-05	1.78255e-05	2.87480e-02
4	Δ_C	8.51158e-11	4.10234e-11	2.06173e-03
4^*	Δ_C	0	0	2.12101e-03

Table 5.5: Mass/energy outflow for $\eta = 1-4$ encounters. We consider a mass ratio $\mu = 1.28 \times 10^{-3}$. The values are normalized by the initial mass M_* and the initial total energy E^0_{tot}. Also given is the amount of normalized energy deposited onto the star at $\tau = 5\tau_0$ in the simulation using a quadrupole and octupole tide. We compare the use of outflow and solid wall boundary conditions for $\eta = 4$ where the asterisk denotes solid wall boundary conditions.

normalized energy deposited onto the star at $\tau = 5\tau_0$ in the simulation using a quadrupole and octupole tide. We compare the use of outflow and solid wall boundary conditions for $\eta = 4$. We note that the mass and energy outflow decreases with increasing η and at $\eta = 4$ the amount leaving the domain is negligible enough to use solid wall boundary conditions.

We see the result of including the octupole tidal term in Figure 5.6. Density contour plots in the xy-plane are given for an $\eta = 3$ encounter with mass ratio $\mu = 1.28 \times 10^{-3}$ simulated with only the quadrupole term (left panel) and with both the quadrupole and octupole term (right panel). The contour lines are given for $\log_{10} \rho$ from -11 to -5 in steps of 0.5. Note that with the inclusion

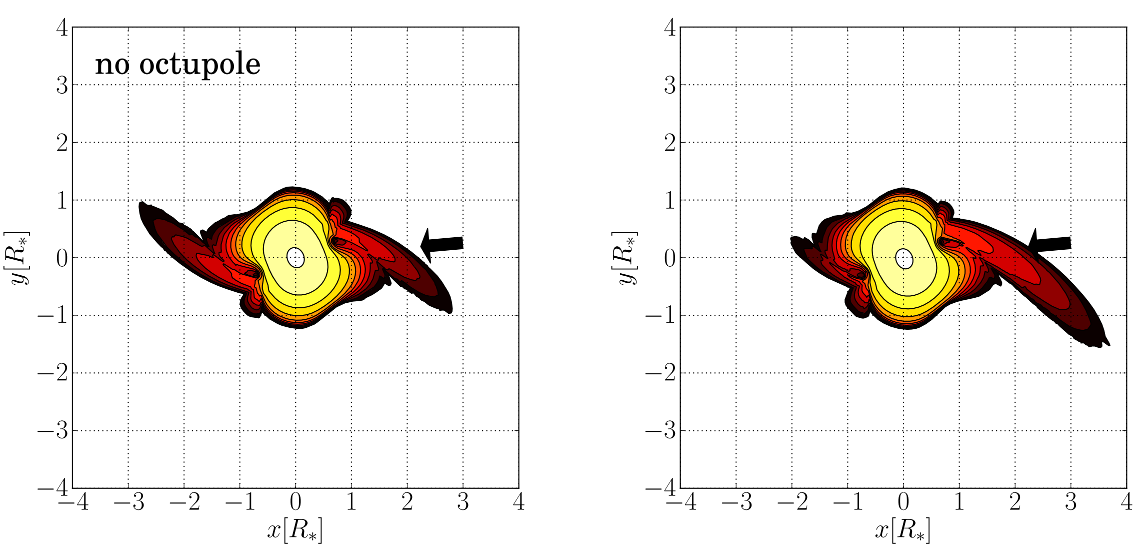

Figure 5.6: Asymmetrical star with octupole tidal term. Contour plots of density of the star in the xy-plane at $\tau = 1.7\tau_0$ for an $\eta = 3$ encounter and mass ratio $\mu = 1.28 \times 10^{-3}$. The contour lines are given for $\log_{10} \rho$ from -11 to -5 in steps of 0.5. Results are given for simulations with only quadrupole ($l = 2$) tidal terms (left) and quadrupole ($l = 2$) and octupole ($l = 3$) tidal terms (right). The resolution of the grids in these simulations is Δ_B. The effect of the octupole tidal term has in driving a deflection of the center of mass is evident in the asymmetrical tidal lobes.

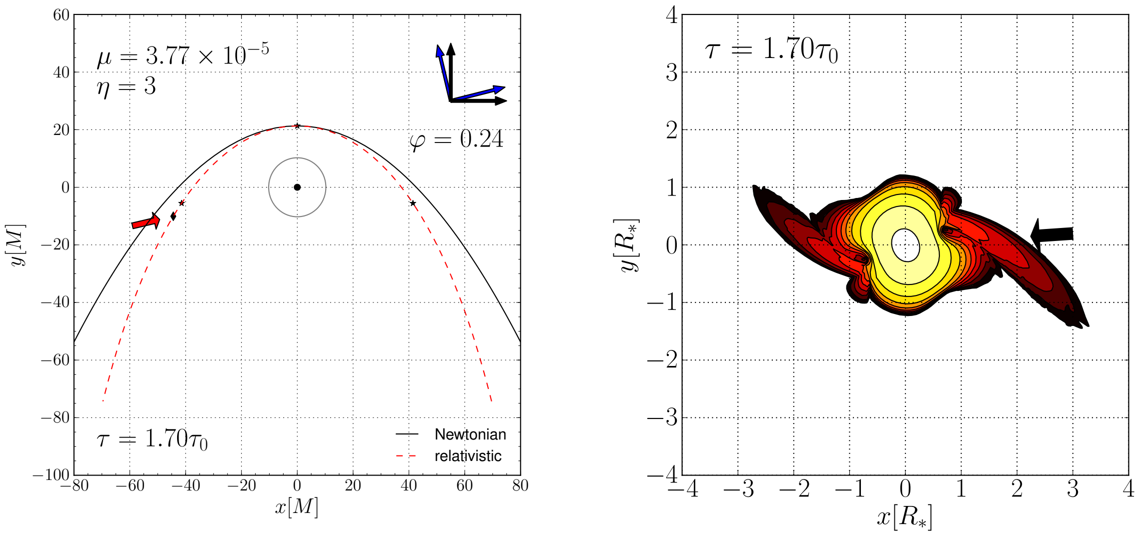

Figure 5.7: A snapshot of an $\eta = 3$ encounter in the black hole and FNC frame. The time is $\tau = 1.7\tau_0$ and the mass ratio is $\mu = 3.77 \times 10^{-5}$. The contour lines are given for $\log_{10} \rho$ from -8 to -2 in steps of 0.5. The quadrupole and octupole tidal terms have been included in the calculation. The arrow in the left panel (black hole frame) is the azimuthal coordinate ϕ' and the arrow in the right panel (FNC frame) gives the direction from the black hole to the origin of the FNC.

of the octupole term, the star is asymmetrical. The black arrow represents the direction from the black hole to the origin in the FNC coordinate system. Consider the results of an $\eta = 3$ encounter with a mass ratio $\mu = 3.77 \times 10^{-5}$ and both the quadrupole and octupole terms in the tidal field, as shown in Figure 5.7. The contour lines are given for $\log_{10} \rho$ from -8 to -2 in steps of 0.5. Note that the star is more asymmetrical for a mass ratio $\mu = 1.28 \times 10^{-3}$ than for $\mu = 3.77 \times 10^{-5}$. This agrees with the analysis from the previous chapter (see Figure 3.4) where the octupole term has more relative importance for mass ratios $\mu \sim 10^{-3}$ than $\mu \sim 10^{-5}$. We give density contour plots from $\tau = 0$ (at periastron) to $\tau = 2.2\tau_0$ in Figure 5.9.

The star is tidally disrupted when $\eta = 1$. In Figure 5.8, plots are given for $\eta = 1, 2, 3$ encounters with mass ratio $\mu = 1.28 \times 10^{-3}$ with grid resolution Δ_B. Inspecting the normalized central density, we see that for $\eta = 2$ and $\eta = 3$, the star is only partially stripped and what is left of the core oscillates violently. We give density contour plots for $\eta = 1$ from $\tau = 0$ (periastron) to $\tau = 1.6\tau_0$ in Figure 5.10.

We calculate the vorticity, $(\vec{\nabla} \times \vec{v})_z$ in the star. Contour plots in the xy-plane are given in Figure 5.11 and 5.12 for $\eta = 3$ and $\eta = 1$ encounters with mass ratio $\mu = 3.77 \times 10^{-5}$. We note that the core of the star remains irrotational. This agrees with the discussion found in Kochanek (1992) [28].

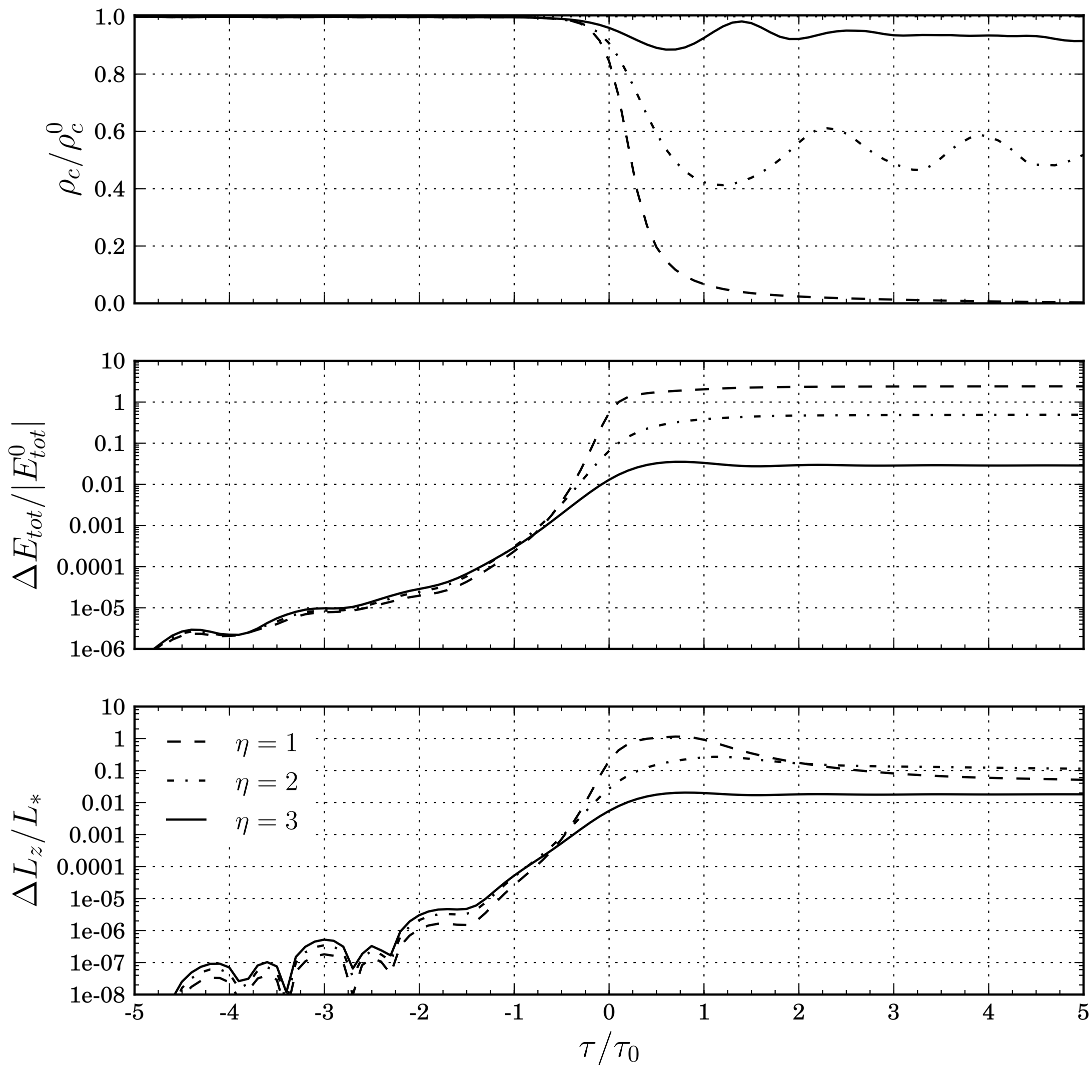

Figure 5.8: Partial and complete disruptions. In the top panel, we give the normalized central density for each tidal encounter simulation by subtracting from it the normalized central density for the equilibrium simulation and adding unity ($\rho_c^\eta/\rho_c^0 - \rho_c^{equil}/\rho_c^0 + 1$). In the next panel, we give the total energy deposited on the star for each tidal encounter simulation subtracted by the change in total energy for the equilibrium simulation ($E_{\rm tot}^\eta - E_{tot}^{\rm equil}$) and divide by the magnitude of the initial total energy $|E_{tot}^0|$. In the bottom panel, we give the total z-component of the spin angular momentum deposited on the star for each tidal encounter simulation subtracted by the change in total z-component of the spin angular momentum for the equilibrium simulation ($L_z^\eta - L_z^{equil}$). Results are given at the highest resolution, Δ_C.

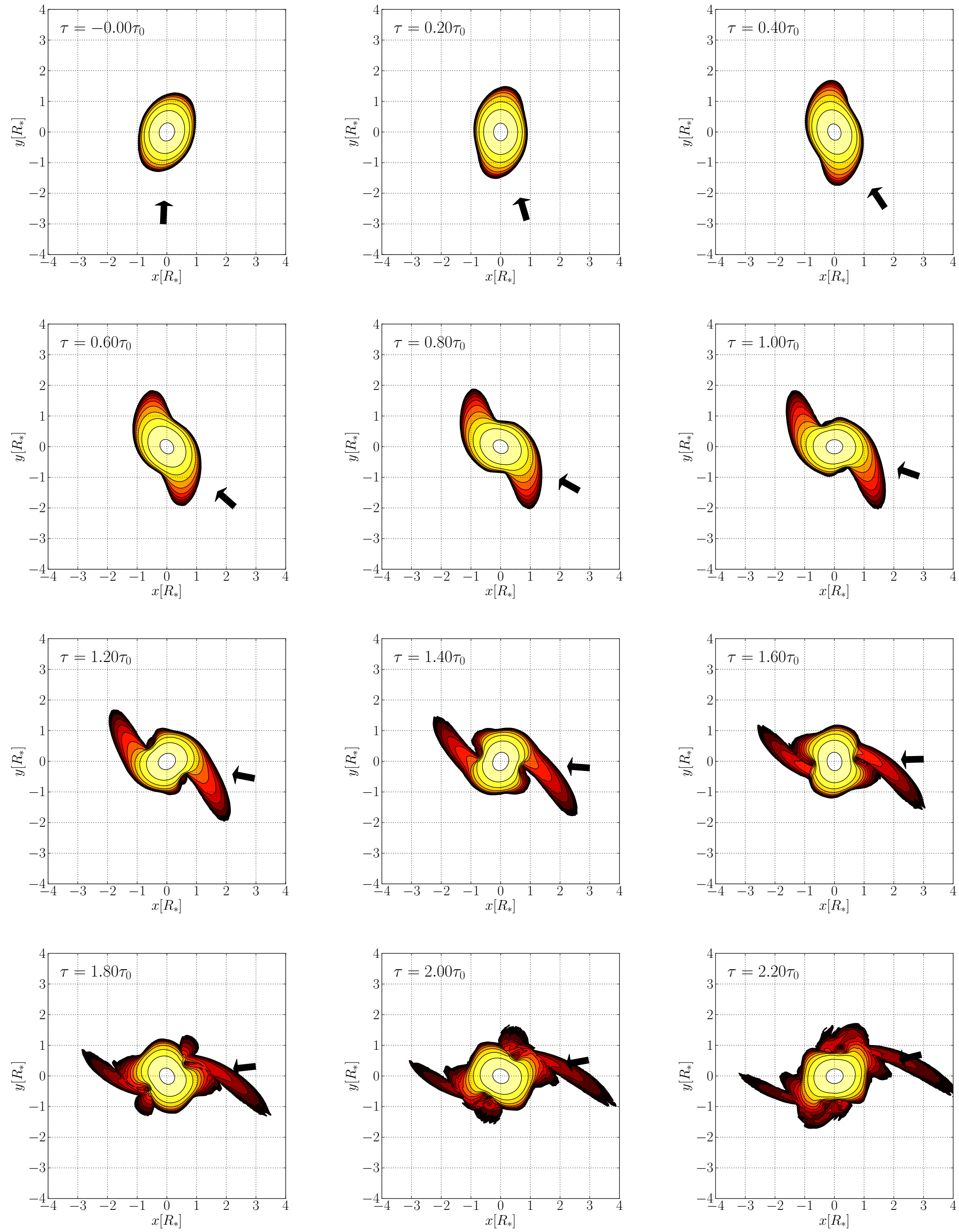

Figure 5.9: Density contours of an $\eta = 3$ encounter and mass ratio $\mu = 3.77 \times 10^{-5}$. The simulation begins at $\tau = -5\tau_0$, reaches periastron at $\tau = 0$, and ends at $\tau = 5\tau_0$. The contour lines are given for $\log_{10} \rho$ from -8 to -2 in steps of 0.5.

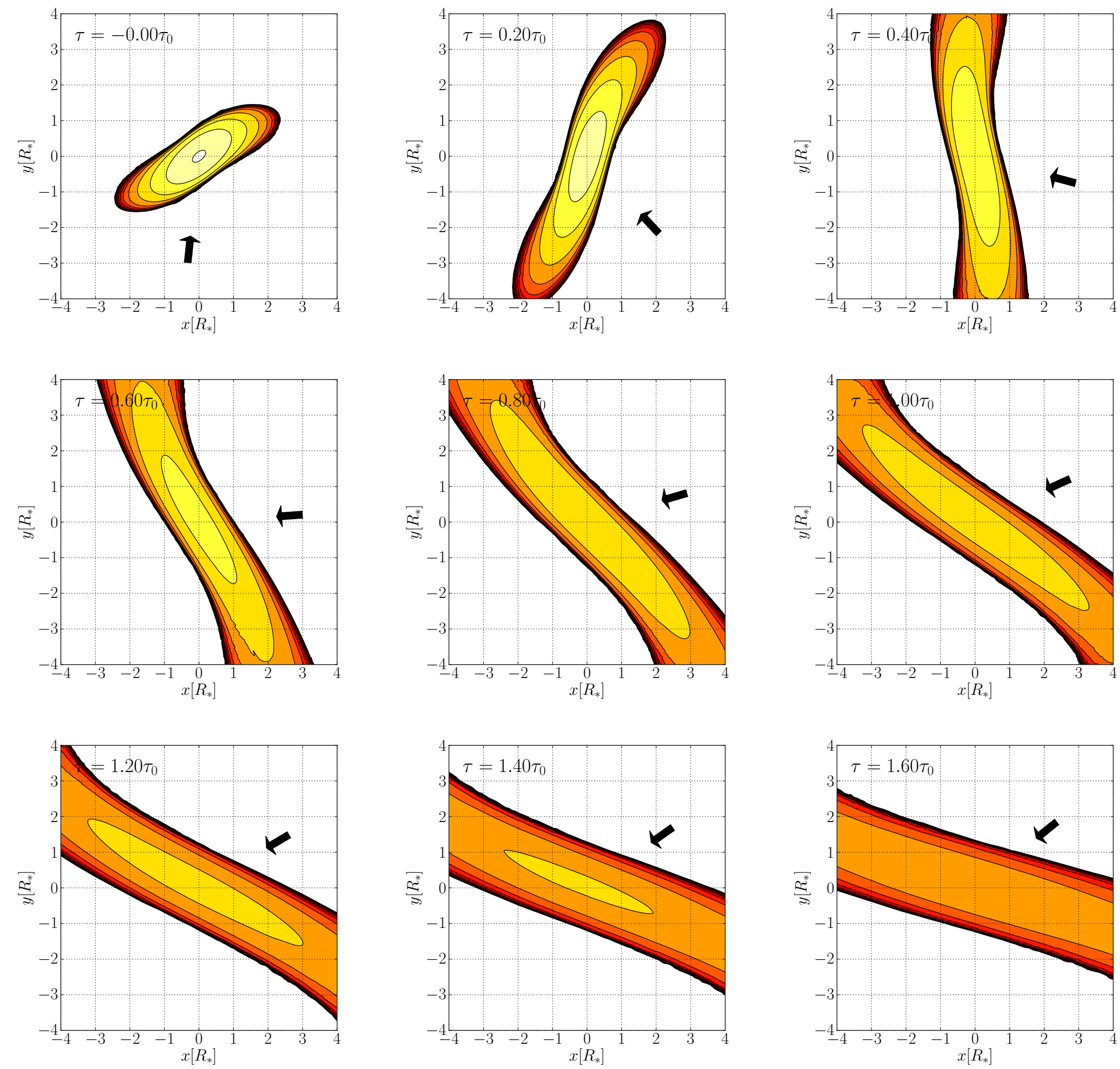

Figure 5.10: Density contours of an $\eta = 1$ encounter and mass ratio $\mu = 3.77 \times 10^{-5}$. The simulation begins at $\tau = -5\tau_0$, reaches periastron at $\tau = 0$, and ends at $\tau = 5\tau_0$. The contour lines are given for $\log_{10}\rho$ from -8 to -2 in steps of 0.5.

In Figures 5.11 and 5.12, it is apparent that vorticity is present only in the outer layers of the star, where shocks have broken the isentropic initial state. The contour lines are given for $|(\vec{\nabla} \times \vec{v})_z|$ from 0 to 0.1 in steps of 0.01.

5.3.3 Comparison with linear theory

We next compare the amount of energy and angular momentum deposited onto the star by the tidal interaction in our full simulations with the predictions of linear theory. We make these comparisons for all of the encounter strengths ($\eta = 1 - 6$) considered in this thesis. For these comparisons, we

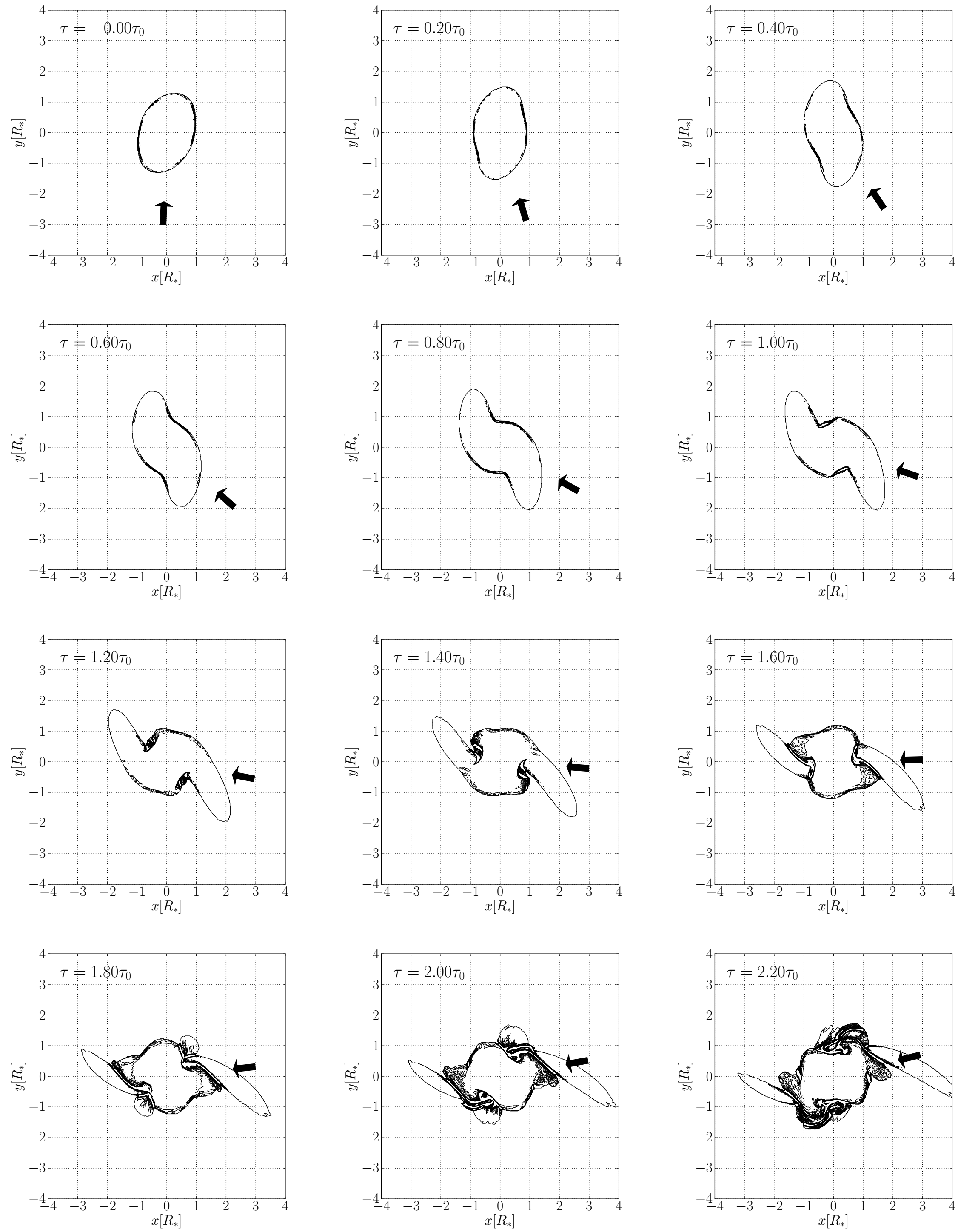

Figure 5.11: Vorticity contours of an $\eta = 3$ encounter and mass ratio $\mu = 3.77\times10^{-5}$. The simulation begins at $\tau = -5\tau_0$, reaches periastron at $\tau = 0$, and ends at $\tau = 5\tau_0$. The contour lines are given for $|(\vec{\nabla} \times \vec{v})_z|$ from 0 to 0.1 in steps of 0.01.

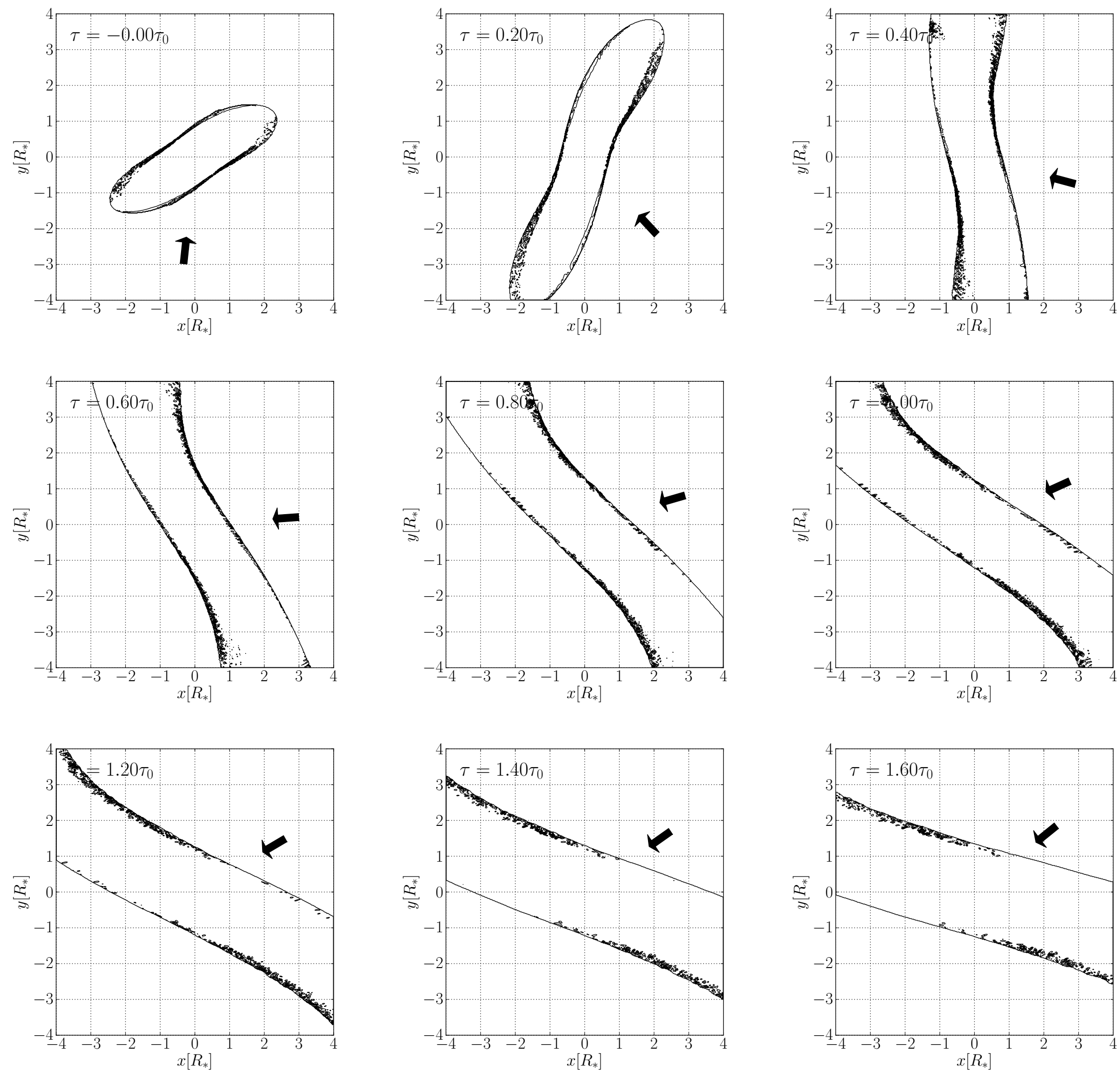

Figure 5.12: Vorticity contours of an $\eta = 1$ encounter and mass ratio $\mu = 3.77\times10^{-5}$. The simulation begins at $\tau = -5\tau_0$, reaches periastron at $\tau = 0$, and ends at $\tau = 5\tau_0$. The contour lines are given for $|(\vec{\nabla} \times \vec{v})_z|$ from 0 to 0.1 in steps of 0.01.

measure the deposited energy and angular momentum at a time of five radial oscillations after the star passes periastron. Each model is computed with three different resolutions $(\Delta_A, \Delta_B, \Delta_C)$. As mentioned above, for $\eta = 4 - 6$, the star does not disrupt and solid wall boundary conditions are used. For $\eta \leq 3$, the star is partially or fully disrupted and we measure the energy that leaves the grid and include it in our analysis.

According to the theoretical analysis of Press and Teukolsky [26] and Lee and Ostriker [27], the

η	Resol.	μ / $\Delta E^{\rm linear}_{l=2,3}$	1.28×10^{-3}	4.21×10^{-4}	3.77×10^{-5}
			$\Delta E_{\rm tot}$		
1	Δ_A	5.647e-08	1.452e-07	4.814e-08	5.693e-09
1	Δ_B	5.647e-08	1.454e-07	4.823e-08	5.707e-09
2	Δ_A	7.818e-09	2.995e-08	9.869e-09	1.078e-09
2	Δ_B	7.818e-09	2.958e-08	9.851e-09	1.069e-09
3	Δ_A	8.651e-10	1.764e-09	5.744e-10	4.941e-11
3	Δ_B	8.651e-10	1.730e-09	5.638e-10	4.850e-11
4	Δ_A	8.076e-11	1.635e-10	5.302e-11	4.213e-12
4	Δ_B	8.076e-11	1.248e-10	4.018e-11	3.045e-12
4	Δ_C	8.076e-11	1.240e-10	4.108e-11	3.027e-12
5	Δ_A	6.899e-12	4.560e-11	1.517e-11	1.328e-12
5	Δ_B	6.895e-12	9.355e-12	3.015e-12	2.129e-13
5	Δ_C	6.895e-12	8.454e-12	2.687e-12	1.830e-13
6	Δ_A	5.558e-13	3.732e-11	1.224e-11	1.065e-12
6	Δ_B	5.558e-13	1.177e-12	3.899e-13	2.830e-14
6	Δ_C	5.558e-13	3.993e-13	1.256e-13	7.144e-15

Table 5.6: Deposited energy $\Delta E_{\rm tot}$ onto the star for relativistic encounters. We use both $l=2$ and $l=3$ contributions to the tidal field. Results at the end of the simulation, $\tau = 5\tau_0$, are given for different resolutions (Δ_A, Δ_B, Δ_C). The amount of energy $\Delta E^{\rm linear}_{l=2,3}$ predicted by linear theory is also given.

η	μ / Δ	1.28×10^{-3}		4.21×10^{-4}		3.77×10^{-5}	
		$<\Delta E>$	$<\Delta L>$	$<\Delta E>$	$<\Delta L>$	$<\Delta E>$	$<\Delta L>$
1	Δ_B	1.450e-07	8.100e-06	4.823e-08	8.349e-07	5.700e-09	3.700e-09
2	Δ_B	2.940e-08	1.800e-05	9.851e-09	1.938e-06	1.060e-09	1.500e-08
3	Δ_B	1.740e-09	2.825e-06	5.650e-10	3.015e-07	4.860e-11	2.320e-09
4	Δ_C	1.270e-10	2.000e-07	4.100e-11	2.130e-08	3.100e-12	1.425e-10
5	Δ_C	9.000e-12	1.450e-08	2.900e-12	1.500e-09	1.980e-13	9.350e-12
6	Δ_C	7.000e-13	1.050e-09	1.900e-13	1.120e-10	1.400e-14	6.300e-13

Table 5.7: Average energy and angular momentum deposited onto the star. Results are given for the highest resolutions (Δ_B, Δ_C) for different encounters $\eta = 1-6$ and mass ratios $\mu = 1.28\times10^{-3}, 4.21\times10^{-4}, 3.77\times10^{-5}$.

amount of energy deposited onto the star into non-radial oscillations is given by

$$\Delta E = \left(\frac{GM_*^2}{R_*}\right)\left(\frac{M_{BH}}{M_*}\right)^2 \sum_{l=2,3,\ldots}\left(\frac{R_*}{R_p}\right)^{2l+2} T_l(\eta), \tag{5.3.4}$$

for spherical harmonic index l and dimensionless functions T_l, which are functions of η alone [26]. We use T_l for an $n=1.5$ polytrope that have been computed previously by others [27, 53].

Table 5.6 gives the amount of energy deposited onto the star at the end of the simulation ($\tau = 5\tau_0$) for Newtonian (quadrupole tide only) and relativistic (quadrupole and octupole tide) encounters. Results for different resolutions (Δ_A, Δ_B, Δ_C) are tabulated. Also given is the amount of energy predicted by linear theory. After the encounter, the amount of total energy and angular momentum

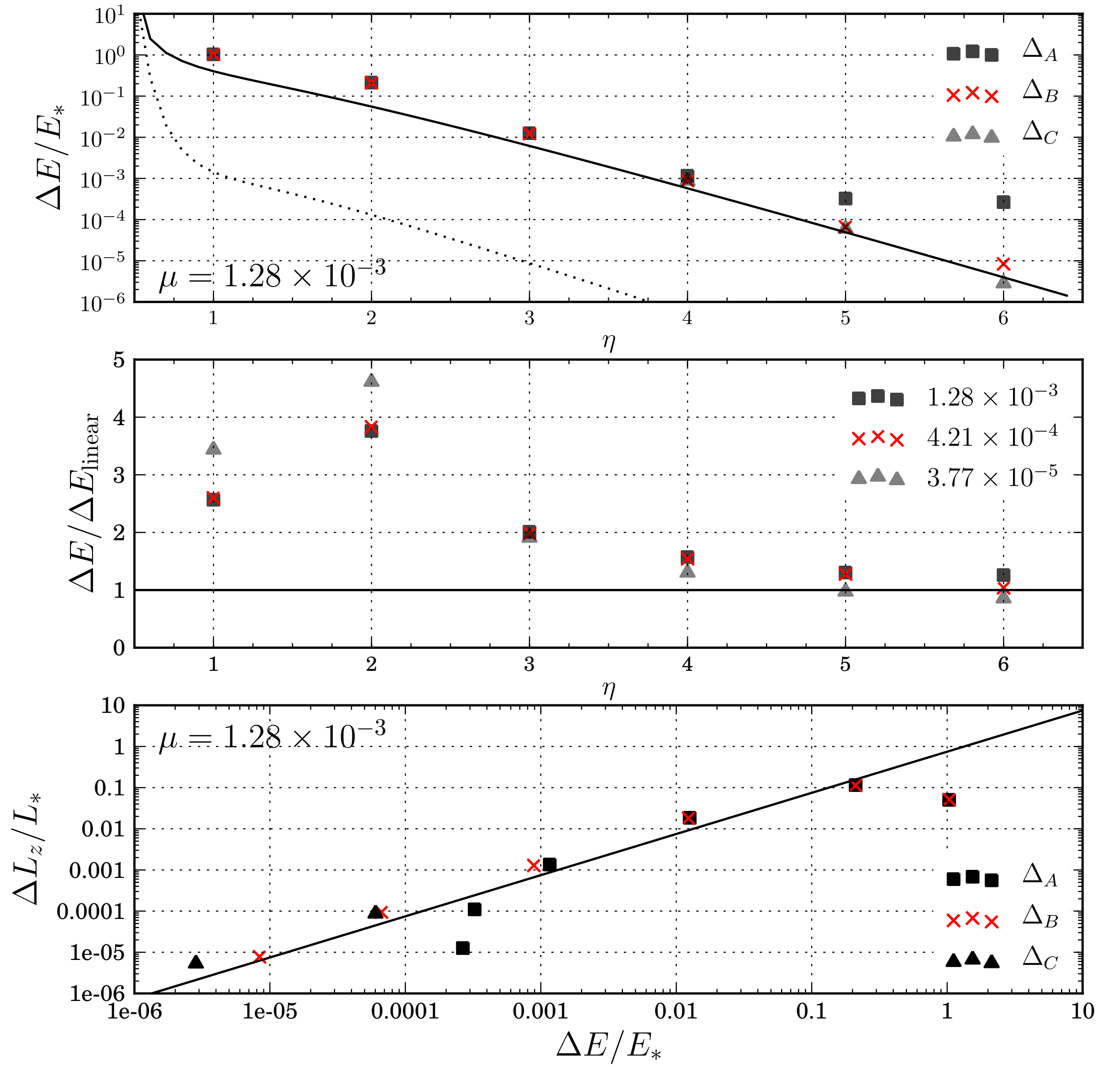

Figure 5.13: Comparison between full simulations and linear theory. Results of encounters $\eta = 1-6$ are shown for different resolutions Δ_A, Δ_B, and Δ_C. In the top panel, we compare the total energy deposited on the star with the predictions from the linear theory for mass ratio $\mu = 1.28\times10^{-3}$. The solid line indicates amount of energy deposited into both the $l = 2$ and $l = 3$ non-radial modes. The dotted line gives only the $l = 3$ contribution. The next panel gives the average amount of deposited energy onto the star divided by the prediction from linear theory. We give results for different mass ratios $\mu = 1.28\times10^{-3}, 4.21\times10^{-4}, 3.77\times10^{-5}$. The bottom panel is a plot of the normalized ΔL_z versus ΔE for mass ratio $\mu = 1.28\times10^{-3}$. The solid line is the proportionality given by [28].

deposited onto the star will oscillate about a new value and we give the average in Table 5.7.

We compare the predicted total energy due to the $l = 2$ and $l = 3$ modes with the change in total energy in the simulations with mass ratio $\mu = 1.28 \times 10^{-3}$ in the top panel of Figure 5.13. It is shown that the dominant contribution to (5.3.4) is due to the $l = 2$ mode, as expected. We compare this result with previous studies using an affine and hydrodynamic model [28, 38]. We see a clear convergence with linear theory as weaker encounters are considered ($\eta = 4, 5$), though our numerical results for $\eta = 6$ are not (yet) sufficiently resolved to include as further confirmation. We note that the results of our simulations for $\eta \leq 3$ indicate that close tidal encounters deposit more energy than linear theory would predict and this has consequences for increasing the tidal capture cross section. Nonlinear effects are apparent in the energy deposition into the fundamental radial mode, which does not occur in linear theory. We consider the average amount of deposited energy divided by the prediction from linear theory for mass ratios $\mu = 1.28 \times 10^{-3}$, 4.21×10^{-4}, and 3.77×10^{-5} in the second panel of Figure 5.13. We note a suppression in the energy with decreasing mass ratio for encounters $\eta \leq 3$. We recognize that for $\eta \geq 3$ the star is completely or partially disrupted and gas leaves the domain, which affects the accuracy of our energy measurement.

We consider the relation between the amount of spin angular momentum and total energy deposited onto the star. After the encounter, the $l = 2$, $m = -2$ f-mode is strongly excited (along with the other $l = 2$ and $l = 3$ modes at lower amplitudes). This mode will contain both angular momentum and vorticity. As we have seen, however, the star remains largely irrotational. This is especially true in the weak encounter limit where nonlinear effects like shock heating near the surface can be neglected and the encounter is adiabatic. In order for vorticity to be conserved, the star emerges from the encounter with also a net bulk rigid rotation superimposed with the nonradial oscillation that is just sufficient to cancel vorticity (see Figures 5.11 and 5.12). Kochanek has analyzed the post-encounter as an irrotational ellipsoid, and found, to lowest order, the proportionality between $\Delta E_{\rm tot}$ and ΔL_z is

$$\Delta E_{\rm tot} = \frac{|E_g|}{\sqrt{15}} \frac{\Delta L_z}{\sqrt{I_* |E_g|}}, \tag{5.3.5}$$

[28]. In the bottom panel of Figure 5.13, this relationship between $\Delta E_{\rm tot}$ and ΔL_z is plotted (solid line) against simulation data of the normalized spin angular momentum and energy deposited onto the star. Each point represents a single simulated encounter with mass ratio $\mu = 1.28 \times 10^{-3}$.

5.3.4 Relativistic encounters

We calculate a derived dimensionless function T_2 using the average amount of energy deposited onto the star during the simulation with (5.3.4). We compare this result with the prediction from

η	μ / $T_2^{\rm linear}$	1.28×10^{-3}	4.21×10^{-4}	3.77×10^{-5}
		$T_2^{\rm relativistic}$		
3	4.984e-01	1.004	9.905e-01	9.525e-01
4	1.472e-01	2.316e-01	2.272e-01	1.920e-01
5	3.070e-02	4.007e-02	3.923e-02	2.994e-02
6	5.126e-03	6.462e-03	5.329e-03	4.390e-03

Table 5.8: Dimensionless function T_2 from linear theory and simulations. We consider T_2 analytically ($_\mu T_2^{\rm linear}$) and calculated from the average energy deposited onto the star for relativistic encounters $\eta = 3 - 6$ with different mass ratios $\mu = 1.28 \times 10^{-3}$, 4.21×10^{-4}, and 3.77×10^{-5}. The values decrease with decreasing mass ratio.

the linear theory [27, 53] in Table 5.8 for $\eta = 3 - 6$ and $\mu = 1.28 \times 10^{-3}$, 4.21×10^{-4}, and 3.77×10^{-5}. For Newtonian encounters, the derived T_2 from simulation should be the same for any mass ratio. We see that for relativistic encounters, T_2 decreases with decreasing mass ratio. This suggests a suppression in T_2 due to relativistic effects. The predicted energy deposition in the linear theory (5.3.4) is derived from the assumption that the interaction is Newtonian. The dimensionless parameter $T_l(\eta)$ is defined in terms of a part, Q_{nl}, that is only dependent on the structure of the star and its non-radial eigenmodes, and a part, K_{nlm}, that depends only on the orbit, [26],

$$\begin{aligned}
T_l(\eta) &= 2\pi^2 \sum_n |Q_{nl}|^2 \sum_{m=-l}^{l} |K_{nlm}|^2, \\
Q_{nl} &= \int_0^1 r^2 dr \rho l r^{l-1} [\xi_{nl}^R + (l+1)\xi_{nl}^S], \\
K_{nlm} &= \frac{W_{lm}}{2\pi} \int_{-\infty}^{\infty} d\tau \left(\frac{R_p}{R(\tau)}\right)^{l+1} \exp\{i[\omega_n \tau + m\Phi(\tau)]\}, \\
W_{lm} &= (-1)^{(l+m)/2} \left[\frac{4\pi}{2l+1}(l-m)!(l+m)!\right]^{1/2} \Big/ \left[2^l \left(\frac{l-m}{2}\right)! \left(\frac{l+m}{2}\right)!\right], \qquad (5.3.6)
\end{aligned}$$

where ξ_{nl}^R and ξ_{nl}^S are the radial and poloidal components of the normal modes of a spherical star, ω_n are the eigenfrequencies associated with these normal modes, and Φ is the true anomaly. We estimate the difference in T_l for a relativistic orbit by considering the order of the correction to K_{nlm}. We will consider the quadrupole contribution only since it is the dominant term in the tidal field. The Newtonian quadrupole is of the order $\mathcal{O}(M/R_p^3)$ such that $|K_{n2m}| \sim \mathcal{O}(M/R_p^3)$ and $\sum_{m=-2}^{2} |K_{nlm}|^2 \sim \mathcal{O}(M/R_p^3)^2$. The relativistic quadrupole has an additional correction such that $|K_{n2m}| \sim \mathcal{O}(M/R_p^3) + \mathcal{O}[(M/R_p^3)(M/R_p)]$ and $\sum_{m=-2}^{2} |K_{n2m}|^2 \sim \mathcal{O}(M/R_p^3)^2 + \mathcal{O}[(M/R_p^3)^2(M/R_p)] + \cdots$. Thus, the relative percentage change between the overlap integral for a Newtonian encounter and the corrected one for a relativistic encounter is of order $|K_{nlm} - K_{nlm}^R|/|K_{nlm}| \sim \mathcal{O}(M/R_p)$. In the overlap integral for K_{nlm}, the M/R_p correction has a sharper time dependence from the $1/R(\tau)^5$ dependence and the phase factor $\Phi(\tau)$ rotates further and more rapidly in a relativistic orbit, due to apsidal advance. Thus, T_2 should not only be a function of η but also of a relativistic dimensionless parameter, $\Phi_p = M/R_p$, such that $T_2^{\text{rel.}}(\eta, \Phi_p)$.

5.3.5 Energy deposited into radial oscillations

After the encounter with the black hole, the star is observed to oscillate in a set of radial modes. This occurs for all encounters below the threshold of disruption and we see the presence of the fundamental radial mode in plots of time dependence of central density in Figures 5.3 and 5.8. In simulations by Khoklov, Novikov, and Pethick (1993) [38, 39], as in ours, there is an excess in the amount of deposited total energy from that predicted by linear theory. Khoklov et al. attributed this to the non-linearity of the non-radial oscillations and to the excitation of radial modes, which do not occur in linear theory. To examine this idea, we simulated models that were deliberately set into radial oscillation in order to quantify how much increase in energy might be due to radial oscillations and to compare the results to our tidal encounters simulations.

We generate radially radial pulsating models by introducing a simple scaling of the Lane-Emden density profile as an initial condition. Consider a homologous mapping of the star that takes the original radius R_* to $R'_* = R_*/\lambda$, where λ is a scaling parameter. The range in radius $r' = a\xi'$ for the new configuration is $r' = [0, R'_*]$. We write the new density profile as $\bar{\rho}(r') = \bar{\rho}_c \theta(\xi')^n$ for some $\bar{\rho}_c$. The total mass of the new configuration is

$$M = 4\pi \int_0^{R'_*} \bar{\rho}(r')(r')^2 dr' = 4\pi \int_0^{R_*/\lambda} \bar{\rho}(r/\lambda)\frac{r^2}{\lambda^3} dr = 4\pi \int_0^{R_*/\lambda} \rho(\lambda r')\lambda^3 r'^2 dr'. \tag{5.3.7}$$

If new density profile is derived from the initial profile by

$$\bar{\rho} = \lambda^3 \rho(\lambda r'), \tag{5.3.8}$$

where $\rho(\lambda r') = \rho_c \theta(\xi = r'\lambda/a)^n$, then the mass is unaffected by the homologous transformation.

We compute models with parameter range $\lambda = [0.9, 0.95, 0.98, 0.995, 1.005, 1.02]$. For these models we plot the normalized central density versus time and the change in total energy relative to the control simulation $\lambda = 0$ in the top two panels of Figure 5.14. In the bottom panel of Figure 5.14, we find that the normalized change in central density versus normalized change in λ is consistent with the initial density profile (5.3.8) such that $\delta\rho/\rho \sim 3\delta\lambda/\lambda$. We compare the change in total energy between radial pulsation and equilibrum models, $\Delta E_{\text{tot}}^{\lambda} - \Delta E_{\text{tot}}^{\lambda=0}$, with the difference in the amount

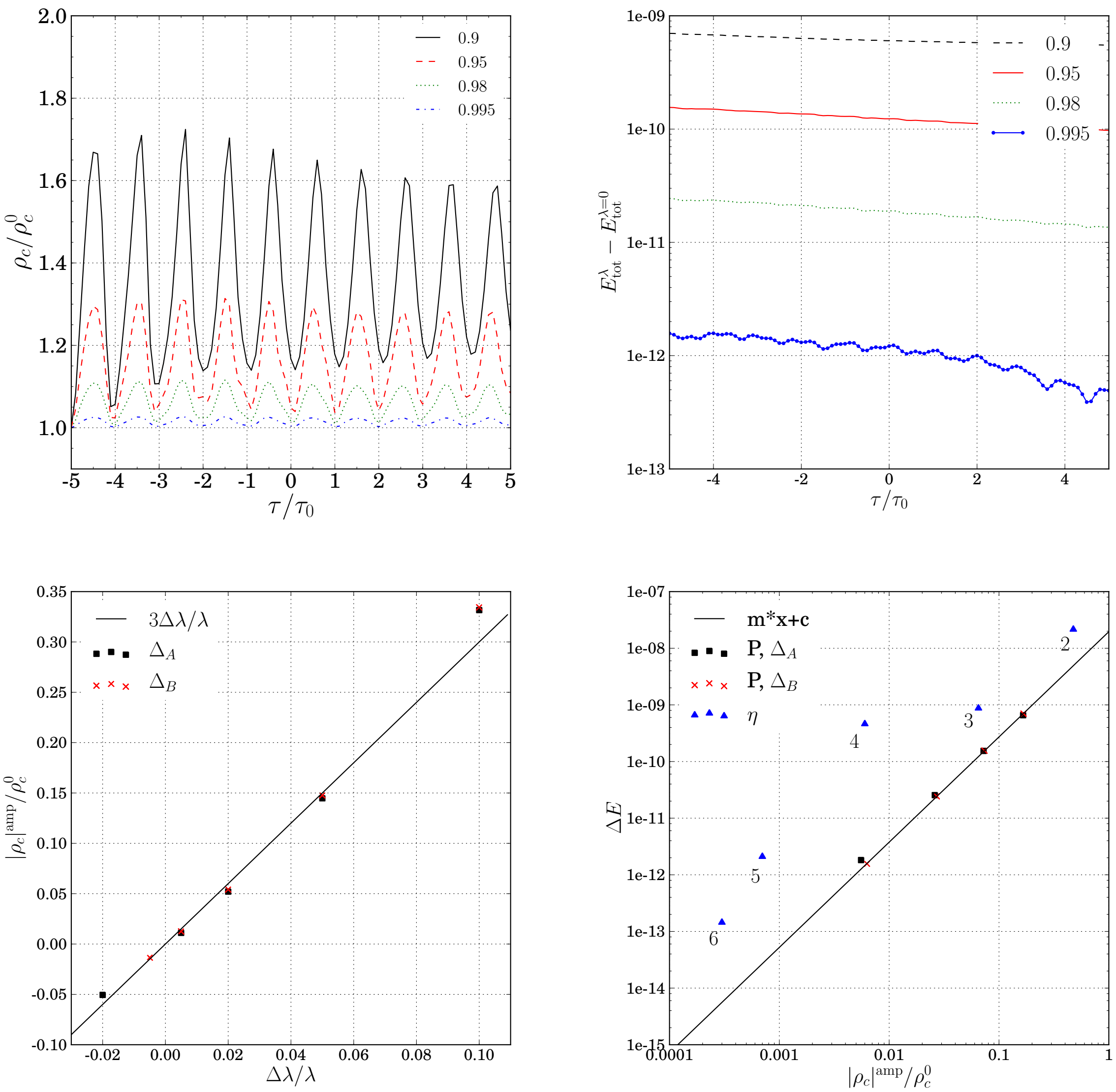

Figure 5.14: Radial pulsation models: the normalized central density and change in total energy from equilibrium model; normalized change in central density versus normalized change in λ; change in total energy between radial pulsation and equilibrum model, $\Delta E_{\rm tot}^{\lambda} - \Delta E_{\rm tot}^{\lambda=0}$ and amount of total energy deposited onto star during tidal encounter ΔE subtracted by the predicted amount by linear theory $\Delta E_{l=2,3}^{\rm linear}$ versus the amplitude of the normalized change in central density. In the top two panels, the normalized central density and change in total energy is given for radial pulsation models $\lambda = [0.9, 0.95, 0.98, 0.995]$ with resolution Δ_B. In the bottom left panel we show the relation between the central density and parameter λ consistent with the initial conditions for mode such that $\delta\rho/\rho \sim 3\delta\lambda/\lambda$. We compare these models with those of tidal encounters $\eta = 2-6$ in the bottom right panel. The fit parameters are $m = 1.86$ and $c = -7.71$. The observed energy excess in tidal encounters is in general an order of magnitude or two higher than can be explained by excitation of the fundamental radial mode.

of total energy deposited onto star during tidal encounter ΔE and the prediction by linear theory $\Delta E_{l=2,3}^{\text{linear}}$ in the bottom right panel of Figure 5.14. These values are functions of the amplitude of oscillation of the normalized central density. For the tidal encounters, we extract the amplitude by subtracting from unity the average value of the normalized central density after the encounter. The fit parameters are $m = 1.86$ and $c = -7.71$. Note that the points from right to left are encounters $\eta = 2 - 6$. The right two points ($\eta = 2, 3$) are partially disruptive encounters and we expect a behavior different from the other three points. We conclude that the amount of energy associated with the excitation of the fundamental radial mode is small compared to the excess energy we see deposited onto the star in our simulations and to the predictions of linear theory. Excitation of radial oscillations appears to be a minor contributor to the tidal energy deposition for $\eta = 4 - 6$. It can be of order $14\% - 22\%$ for $\eta = 2$ and 3. See Table 5.9.

5.3.6 Energy deposited by to shock heating

η	ΔE	$\Delta E^{\text{radial}}/\Delta E$	$\Delta E^{\text{shock}}/\Delta E$
2	2.1581e-8	0.2277	0.5388
3	8.7489e-10	0.1395	1.5234
4	4.6235e-10	0.0031	0.2607

Table 5.9: Energy excess due to radial oscillations and shock heating. The energy excess between the total energy deposited onto the star during the simulation and that predicted by linear theory is given by $\Delta E = \Delta E_{\text{tot}} - \Delta E_{l=2,3}^{\text{linear}}$. We consider the contributions to this excess due to the energy deposited into radial oscillations and shock heating for encounters $\eta = 2 - 4$ and mass ratio $\mu = 1.28 \times 10^{-3}$.

We next consider the change in total energy of the star due to shock heating during the encounter. After passing by the black hole, the star is observed to expand and we can relate the change in density to a change in the energy of the configuration. We apply this assumption to non-disruptive encounters and partially-disruptive encounters, focusing on the expansion of the remaining core. We can do this approximately by assuming that the new configuration, with lowered central density, is another polytropic model with the same polytropic index n and with the original mass, M_*. Then, given M_* (unchanged) and ρ_c, we can determine a new value of κ using (2.2.33)

$$M_* = -4\pi \left[\frac{(n+1)\kappa}{4\pi G}\right]^{3/2} \rho_c^{(3-n)/2n} \left(-\xi^2 \frac{d\theta_n}{d\xi}\right)_{\xi=\xi_1}, \tag{5.3.9}$$

for an $n = 1.5$ polytrope. Indeed, this can be solved for κ in terms of the central density, ρ_c,

$$\kappa(\rho_c) = \frac{2\; 2^{2/3}}{5} G M^{2/3} \pi^{1/3} \left(-\xi^2 \frac{d\theta_n}{d\xi}\right)_{\xi=\xi_1}^{-2/3} \rho_c^{-1/3}. \tag{5.3.10}$$

Then, the radius can be derived from κ and ρ_c by

$$R(\kappa, \rho_c) = \sqrt{\frac{5}{8\pi}\kappa}\ \xi_1 \rho_c^{-1/6}. \tag{5.3.11}$$

Finally, we can estimate the change in total energy by calculating the total energy of the polytrope using the new radius (2.2.25),

$$E_{\rm tot}^{'}(R) = -\left(\frac{3\gamma - 4}{5\gamma - 6}\right)\frac{GM_*^2}{R}, \tag{5.3.12}$$

where $\gamma = 5/3$. Using the time evolution of central density (Figures 5.3 and 5.8) which shows the post-encounter new average density for encounters $\eta = 2 - 6$, the above analysis leads to estimated amounts of energy deposited via shock heating. These are compared in Table 5.9 with the amount of energy observed to be deposited in the simulations in excess of the predictions of linear theory. While not a perfect match, the effects of shock heating are order of magnitude correct. We conclude that shock heating of the outer layers of the post-encounter star is the most likely repository of the excess deposited energy.

5.4 Estimates of return orbit after first encounter

	$< \Delta E >$ (erg)				
η	$\mu = 1.28 \times 10^{-3}$	R_p (cm)	R_a (cm)	$1 - e$	T (s)
2	2.629e+49	1.260e+10	3.202e+12	7.840e-03	4.970e+04
3	1.556e+48	1.651e+10	5.430e+13	6.080e-04	3.452e+06
4	1.135e+47	2.000e+10	7.442e+14	5.376e-05	1.750e+08
5	8.046e+45	2.321e+10	1.050e+16	4.421e-06	9.279e+09
6	6.258e+44	2.621e+10	1.350e+17	3.883e-07	4.278e+11
η	$\mu = 4.21 \times 10^{-4}$	R_p (cm)	R_a (cm)	$1 - e$	T (s)
2	2.676e+49	1.825e+10	9.576e+12	3.805e-03	1.470e+05
3	1.535e+48	2.391e+10	1.673e+14	2.859e-04	1.070e+07
4	1.114e+47	2.897e+10	2.305e+15	2.514e-05	5.475e+08
5	7.877e+45	3.362e+10	3.259e+16	2.063e-06	2.910e+10
6	5.161e+44	3.796e+10	4.974e+17	1.526e-07	1.735e+12
η	$\mu = 3.77 \times 10^{-5}$	R_p (cm)	R_a (cm)	$1 - e$	T (s)
2	3.219e+49	4.081e+10	8.912e+13	9.154e-04	1.246e+06
3	1.476e+48	5.348e+10	1.945e+15	5.500e-05	1.269e+08
4	9.415e+46	6.478e+10	3.049e+16	4.250e-06	7.876e+09
5	6.013e+45	7.517e+10	4.773e+17	3.150e-07	4.879e+11
6	4.252e+44	8.489e+10	6.751e+18	2.515e-08	2.595e+13

Table 5.10: The change in orbit due to the loss of orbital energy during the encounter. We give the amount of energy deposited onto the star (taken from the orbit) and the periastron R_p of the initial parabolic orbit. We give the apastron R_a, eccentricity e, and period of return T of the new elliptical orbit. Results are given for encounters $\eta = 2 - 6$ and mass ratios $\mu = 1.28 \times 10^{-3}$, 4.21×10^{-4}, and 3.77×10^{-5}.

We calculate the amount of energy taken from the orbit and deposited onto the star in the simulations. The star is assumed to be initially on a marginally bound (parabolic) orbit and, after the encounter, it will be on a highly elliptical orbit. We estimate the amount of energy taken from the orbit and deposited onto the star with Newtonian considerations. Initially, the star is on a parabolic orbit with orbital energy $E = 0$ and eccentricity $e = 1$. Orbital energy decreases when energy is deposited onto the star and the result is an elliptical orbit with $E < 0$ and $e < 1$, where

$$\epsilon = \frac{1}{2}\dot{r}^2 + \frac{l^2}{2mr^2} - \frac{GM}{r} < 0, \tag{5.4.1}$$

in terms of specific orbital energy ϵ and angular momentum l, and

$$r_1 = a(1-e), \qquad r_2 = a(1+e), \qquad a = \frac{r_1 + r_2}{2}, \tag{5.4.2}$$

where r_1 is periastron, r_2 is apastron, and a is the semi-major axis. At periastron and apastron, we write the specific energy equation in terms of the amount deposited onto the star, $\Delta\epsilon = \Delta E_{\rm tot}/M_* < 0$, and taken from the orbit as

$$\Delta\epsilon = \frac{l^2}{2mr^2} - \frac{GM}{r}, \tag{5.4.3}$$

and solve for r to obtain

$$r = \frac{1}{2}\left[-\frac{GM}{\Delta\epsilon} \pm \sqrt{(\frac{GM}{\Delta\epsilon})^2 - 4\left(-\frac{l^2}{2\Delta\epsilon}\right)^2}\right]. \tag{5.4.4}$$

The semi-major axis is then,

$$a = -\frac{GM}{2\Delta\epsilon}. \tag{5.4.5}$$

From Kepler's third law we write the return period as

$$\tau = 2\pi(GM)^{-1/2}a^{3/2}. \tag{5.4.6}$$

We take periastron of the elliptical orbit $r_1 = R_p$ to be the same as that of the initial parabolic orbit. The new eccentricity is then

$$e = 1 - R_p/a. \tag{5.4.7}$$

We give results for encounters $\eta = 2-6$ and mass ratios $\mu = 1.28\times10^{-3}, 4.21\times10^{-4}$, and 3.77×10^{-5}

in Table 5.10.

In this chapter, we have given results of applying the numerical method to tidal interactions between a white dwarf and an intermediate mass black hole. We compare our tidal encounters against stellar equilibrium simulations of the same star. We compare our results to semi-analytical calculations from linear theory and the affine model in the regime of weak tidal interactions. In our simulations, we show a relativistic suppression in the amount of energy deposited onto the star. We speculate on source of the observed energy excess in the tidal encounter simulations from linear theory and find that the energy deposited into radial oscillations is negligible and that the shock heating in the outer layers of the post-encounter star contributes a significant amount. Using the amount of energy deposited onto the star, we estimate parameters of the post-encounter orbit.

Chapter 6

Conclusions

In this thesis we have presented a new numerical method to simulate the tidal disruption of a star by a massive black hole. We have applied this method to white dwarf encounters with an intermediate mass Schwarzschild black hole. The formalism for calculating the tidal interaction in Fermi normal coordinates (FNC) allows the addition of an arbitrary number of terms in the tidal interaction. By assuming Newtonian stellar self-gravity and hydrodynamics, the number of terms is limited and we justify the use of these terms in this thesis.

We have given an analysis of the tidal disruption of a star by a black hole in the Newtonian limit. We present our assumptions for the Newtonian star that is used in our calculations and discuss the consequences of an interaction with a Newtonian tidal field. This analysis is applied to the results of simulations of the relativistic tidal interaction. We show in detail the formalism we use for the relativistic treatment in Fermi normal coordinates, where we may expand the metric for a general spacetime. We give the fluid equations of motion of the white dwarf and in the tidal field of a Schwarzschild black hole and give the number of significant terms we may use in the tidal expansion, derived from this formalism. The Newtonian hydrodynamic equations are solved using the piecewise parabolic method with Lagrangian remap (PPMLR) and we use a pseudo-spectral method for Poisson's equation for theNewtonian gravitational field of the star. We present a routine to calculate the relativistic tidal interaction between the white dwarf and the black hole in the FNC frame along a geodesic. The new results from this method include a comparison of the amount of spin-angular momentum and total energy deposited onto the star with the linear theory and the affine model, the inclusion of the octupole tidal term which drives the center of mass of the star off of the FNC origin and produces asymmetrical tidal lobes on the star, and measuring the relativistic correction for the dimensionless parameter associated with energy deposition, T_2.

This work is the first to include the Ishii et al. formalism for the relativistic tidal field in FNC. It is the first to compute the $l = 3$ tidal term and its affect in driving the CM of the star off of the initial trajectory. As far as we know, it is the first to see a relativistic suppression of the tidal heating. We note an excess in the amount of energy deposited onto the star from the prediction of linear theory in our simulations. Using radial pulsation models, we find that the energy deposited into radial oscillations is neglible. We estimate that the shock heating in the outer layers of the post-encounter star contributes a significant amount to this excess. We would like to see the effects of the gravitomagnetic and $l = 4$ terms in the tidal expansion and will address this in the future with higher resolution studies.

An extension of this work would be determining the orbital parameters of the debris from the disrupted star. This could be calculated by considering the outflow of gas from the computational domain during the encounter. We would like to understand the prompt hydrodynamic effects of the disruption phase and compute the mass distribution in phase space of captured debris. This understanding will allow an estimate of the accretion flare that occurs as the debris returns to the hole.

The method may be applied to a variety of stars such as main sequence stars and red giants. By including post-Newtonian corrections to the hydrodynamics and self-gravity, more compact objects, such as a neutron star, may be considered. A similar formalism to the work in this thesis may be to Kerr black holes. We would like to include a Kerr metric derivation of the FNC frame and Kerr orbital motion. We would then be able to compute the effects of black hole spin on the disruption of the star.

[1] M. J. Rees. Tidal disruption of stars by black holes of 10^6 to 10^8 solar masses in nearby galaxies. *Nature*, 333:523–528, June 1988.

[2] S. Komossa, J. Halpern, N. Schartel, G. Hasinger, M. Santos-Lleo, and P. Predehl. A Huge Drop in the X-Ray Luminosity of the Nonactive Galaxy RX J1242.6-1119A, and the First Postflare Spectrum: Testing the Tidal Disruption Scenario. *ApJL*, 603:L17–L20, March 2004.

[3] J. Magorrian and S. Tremaine. Rates of tidal disruption of stars by massive central black holes. *MNRAS*, 309:447–460, October 1999.

[4] J. Wang and D. Merritt. Revised Rates of Stellar Disruption in Galactic Nuclei. *ApJ*, 600:149–161, January 2004.

[5] M. Kesden. Tidal-disruption rate of stars by spinning supermassive black holes. *Physical Review D*, 85(2):024037, January 2012.

[6] J. P. Halpern, S. Gezari, and S. Komossa. Follow-Up Chandra Observations of Three Candidate Tidal Disruption Events. *ApJ*, 604:572–578, April 2004.

[7] P. Esquej, R. D. Saxton, M. J. Freyberg, A. M. Read, B. Altieri, M. Sanchez-Portal, and G. Hasinger. Candidate tidal disruption events from the XMM-Newton slew survey. *A&A*, 462:L49–L52, February 2007.

[8] S. Gezari, S. Basa, D. C. Martin, G. Bazin, K. Forster, B. Milliard, J. P. Halpern, P. G. Friedman, P. Morrissey, S. G. Neff, D. Schiminovich, M. Seibert, T. Small, and T. K. Wyder. UV/Optical Detections of Candidate Tidal Disruption Events by GALEX and CFHTLS. *ApJ*, 676:944–969, April 2008.

[9] N. Cappelluti, M. Ajello, P. Rebusco, S. Komossa, A. Bongiorno, C. Clemens, M. Salvato, P. Esquej, T. Aldcroft, J. Greiner, and H. Quintana. A candidate tidal disruption event in the Galaxy cluster Abell 3571. *A&A*, 495:L9–L12, February 2009.

[10] S. Komossa, H. Zhou, A. Rau, M. Dopita, A. Gal-Yam, J. Greiner, J. Zuther, M. Salvato, D. Xu, H. Lu, R. Saxton, and M. Ajello. NTT, Spitzer, and Chandra Spectroscopy of SDSSJ095209.56+214313.3: The Most Luminous Coronal-line Supernova Ever Observed, or a Stellar Tidal Disruption Event? *ApJ*, 701:105–121, August 2009.

[11] L. E. Strubbe and E. Quataert. Optical flares from the tidal disruption of stars by massive black holes. *MNRAS*, 400:2070–2084, December 2009.

[12] W. P. Maksym, M. P. Ulmer, and M. Eracleous. A Tidal Disruption Flare in A1689 from an Archival X-ray Survey of Galaxy Clusters. *ApJ*, 722:1035–1050, October 2010.

[13] J. S. Bloom, D. Giannios, B. D. Metzger, S. B. Cenko, D. A. Perley, N. R. Butler, N. R. Tanvir, A. J. Levan, P. T. O'Brien, L. E. Strubbe, F. De Colle, E. Ramirez-Ruiz, W. H. Lee, S. Nayakshin, E. Quataert, A. R. King, A. Cucchiara, J. Guillochon, G. C. Bower, A. S. Fruchter, A. N. Morgan, and A. J. van der Horst. A Possible Relativistic Jetted Outburst from a Massive Black Hole Fed by a Tidally Disrupted Star. *Science*, 333:203–, July 2011.

[14] D. N. Burrows, J. A. Kennea, G. Ghisellini, V. Mangano, B. Zhang, K. L. Page, M. Eracleous, P. Romano, T. Sakamoto, A. D. Falcone, J. P. Osborne, S. Campana, A. P. Beardmore, A. A. Breeveld, M. M. Chester, R. Corbet, S. Covino, J. R. Cummings, P. D'Avanzo, V. D'Elia, P. Esposito, P. A. Evans, D. Fugazza, J. M. Gelbord, K. Hiroi, S. T. Holland, K. Y. Huang, M. Im, G. Israel, Y. Jeon, Y.-B. Jeon, H. D. Jun, N. Kawai, J. H. Kim, H. A. Krimm, F. E.

Marshall, P. Mészáros, H. Negoro, N. Omodei, W.-K. Park, J. S. Perkins, M. Sugizaki, H.-I. Sung, G. Tagliaferri, E. Troja, Y. Ueda, Y. Urata, R. Usui, L. A. Antonelli, S. D. Barthelmy, G. Cusumano, P. Giommi, A. Melandri, M. Perri, J. L. Racusin, B. Sbarufatti, M. H. Siegel, and N. Gehrels. Relativistic jet activity from the tidal disruption of a star by a massive black hole. *Nature*, 476:421–424, August 2011.

[15] A. J. Levan, N. R. Tanvir, S. B. Cenko, D. A. Perley, K. Wiersema, J. S. Bloom, A. S. Fruchter, A. d. U. Postigo, P. T. O'Brien, N. Butler, A. J. van der Horst, G. Leloudas, A. N. Morgan, K. Misra, G. C. Bower, J. Farihi, R. L. Tunnicliffe, M. Modjaz, J. M. Silverman, J. Hjorth, C. Thöne, A. Cucchiara, J. M. C. Cerón, A. J. Castro-Tirado, J. A. Arnold, M. Bremer, J. P. Brodie, T. Carroll, M. C. Cooper, P. A. Curran, R. M. Cutri, J. Ehle, D. Forbes, J. Fynbo, J. Gorosabel, J. Graham, D. I. Hoffman, S. Guziy, P. Jakobsson, A. Kamble, T. Kerr, M. M. Kasliwal, C. Kouveliotou, D. Kocevski, N. M. Law, P. E. Nugent, E. O. Ofek, D. Poznanski, R. M. Quimby, E. Rol, A. J. Romanowsky, R. Sánchez-Ramírez, S. Schulze, N. Singh, L. van Spaandonk, R. L. C. Starling, R. G. Strom, J. C. Tello, O. Vaduvescu, P. J. Wheatley, R. A. M. J. Wijers, J. M. Winters, and D. Xu. An Extremely Luminous Panchromatic Outburst from the Nucleus of a Distant Galaxy. *Science*, 333:199–, July 2011.

[16] A. Khokhlov and F. Melia. Powerful Ejection of Matter from Tidally Disrupted Stars near Massive Black Holes and a Possible Application to Sagittarius A East. *ApJL*, 457:L61+, February 1996.

[17] D. Kasen and E. Ramirez-Ruiz. Optical Transients from the Unbound Debris of Tidal Disruption. *ApJ*, 714:155–162, May 2010.

[18] S. Kobayashi, P. Laguna, E. S. Phinney, and P. Mészáros. Gravitational Waves and X-Ray Signals from Stellar Disruption by a Massive Black Hole. *ApJ*, 615:855–865, November 2004.

[19] B. Carter and J. P. Luminet. Pancake detonation of stars by black holes in galactic nuclei. *Nature*, 296:211–214, March 1982.

[20] Y. Rathore, R. D. Blandford, and A. E. Broderick. Resonant excitation of white dwarf oscillations in compact object binaries - I. The no back reaction approximation. *MNRAS*, 357:834–846, March 2005.

[21] S. Rosswog, E. Ramirez-Ruiz, and W. R. Hix. Tidal Disruption and Ignition of White Dwarfs by Moderately Massive Black Holes. *ApJ*, 695:404–419, April 2009.

[22] J. H. Krolik and T. Piran. Swift J1644+57: A White Dwarf Tidally Disrupted by a 10^4 $M_\odot$ Black Hole? *ApJ*, 743:134, December 2011.

[23] Y. Rathore. *Resonant excitation of white dwarf oscillations in compact object binaries*. PhD thesis, California Institute of Technology, 2005.

[24] P. J. Young, G. A. Shields, and J. C. Wheeler. The black tide model of QSOs. *ApJ*, 212:367–382, March 1977.

[25] A. C. Fabian, J. E. Pringle, and M. J. Rees. Tidal capture formation of binary systems and X-ray sources in globular clusters. *MNRAS*, 172:15P, August 1975.

[26] W. H. Press and S. A. Teukolsky. On formation of close binaries by two-body tidal capture. *ApJ*, 213:183–192, 1977.

[27] H. M. Lee and J. P. Ostriker. Cross sections for tidal capture binary formation and stellar merger. *ApJ*, 310:176–188, November 1986.

[28] C. S. Kochanek. The dynamical evolution of tidal capture binaries. *ApJ*, 385:604–620, February 1992.

[29] B. Carter and J. P. Luminet. Mechanics of the affine star model. *MNRAS*, 212:23–55, January 1985.

[30] R. A. Gingold and J. J. Monaghan. Smoothed particle hydrodynamics - Theory and application to non-spherical stars. *MNRAS*, 181:375–389, November 1977.

[31] R. A. Nolthenius and J. I. Katz. The infall of a star into a massive black hole. *ApJ*, 269:297–302, June 1983.

[32] C. R. Evans and C. S. Kochanek. The tidal disruption of a star by a massive black hole. *ApJL*, 346:L13–L16, November 1989.

[33] P. Laguna, W. A. Miller, W. H. Zurek, and M. B. Davies. Tidal disruptions by supermassive black holes - Hydrodynamic evolution of stars on a Schwarzschild background. *ApJL*, 410:L83–L86, June 1993.

[34] S. Ayal, M. Livio, and T. Piran. Tidal Disruption of a Solar-Type Star by a Supermassive Black Hole. *ApJ*, 545:772–780, December 2000.

[35] G. Lodato, A. R. King, and J. E. Pringle. Stellar disruption by a supermassive black hole: is the light curve really proportional to $t^{-5/3}$? *MNRAS*, 392:332–340, January 2009.

[36] M. S. Fulbright. *The Tidal Disruption of Stars by a Massive Black Hole at the Center of a Galaxy.* PhD thesis, THE UNIVERSITY OF ARIZONA., January 1995.

[37] M. Brassart and J.-P. Luminet. Relativistic tidal compressions of a star by a massive black hole. *A&A*, 511:A80+, February 2010.

[38] A. Khokhlov, I. D. Novikov, and C. J. Pethick. Weak Tidal Encounters of a Star with a Massive Black Hole. *ApJ*, 418:163, November 1993.

[39] A. Khokhlov, I. D. Novikov, and C. J. Pethick. Strong Effects during Close Encounters of a Star with a Massive Black Hole. *ApJ*, 418:181, November 1993.

[40] J. A. Marck, A. Lioure, and S. Bonazzola. Numerical study of the tidal interaction of a star and a massive black hole. *A&A*, 306:666, February 1996.

[41] J. Guillochon, E. Ramirez-Ruiz, S. Rosswog, and D. Kasen. Three-dimensional Simulations of Tidally Disrupted Solar-type Stars and the Observational Signatures of Shock Breakout. *ApJ*, 705:844–853, November 2009.

[42] V. P. Frolov, A. M. Khokhlov, I. D. Novikov, and C. J. Pethick. Relativistic tidal interaction of a white dwarf with a massive black hole. *ApJ*, 432:680–689, September 1994.

[43] P. Diener, V. P. Frolov, A. M. Khokhlov, I. D. Novikov, and C. J. Pethick. Relativistic Tidal Interaction of Stars with a Rotating Black Hole. *ApJ*, 479:164, April 1997.

[44] R. Haas, R. V. Shcherbakov, T. Bode, and P. Laguna. Tidal Disruptions of White Dwarfs from Ultra-close Encounters with Intermediate-mass Spinning Black Holes. *ApJ*, 749:117, April 2012.

[45] Z. B. Etienne, J. A. Faber, Y. T. Liu, S. L. Shapiro, K. Taniguchi, and T. W. Baumgarte. Fully general relativistic simulations of black hole-neutron star mergers. *Physical Review D*, 77(8):084002, April 2008.

[46] S. Chandrasekhar. *An Introduction To the Study Of Stellar Structure.* Dover Publications, Inc., New York, 1939.

[47] S. L. Shapiro and S. A. Teukolsky. *Black holes, white dwarfs, and neutron stars: The physics of compact objects.* Wiley-Interscience, New York, 1983.

[48] Y. B. Zel'Dovich and Y. P. Raizer. *Physics of shock waves and high-temperature hydrodynamic phenomena.* Dover, Mineola, New York, 1967.

[49] J. P. Cox and R. T. Giuli. *Principles of stellar structure.* Gordon and Breach, New York, 1968.

[50] G. P. Horedt, editor. *Polytropes - Applications in Astrophysics and Related Fields*, volume 306 of *Astrophysics and Space Science Library*, Wessling, Germany, July 2004. Kluwer Academic Publishers.

[51] S. Chandrasekhar. *Ellipsoidal figures of equilibrium.* Dover Publications, Inc., New York, 1973.

[52] J. P. Cox. *Theory of stellar pulsation.* Princeton University Press, Princeton, NJ, 1980.

[53] S. F. Portegies Zwart and A. T. Meinen. Quick method for calculating energy dissipation in tidal interaction. *A&A*, 280:174–176, December 1993.

[54] J. H. Lacy, C. H. Townes, and D. J. Hollenbach. The nature of the central parsec of the Galaxy. *ApJ*, 262:120–134, November 1982.

[55] E. Poisson. *A relativist's toolkit : the mathematics of black-hole mechanics.* Cambridge University Press, Cambridge, 2004.

[56] C. W. Misner, K. S. Thorne, and J. A. Wheeler. *Gravitation.* W.H. Freeman and Co., San Francisco, 1973.

[57] F. K. Manasse and C. W. Misner. Fermi Normal Coordinates and Some Basic Concepts in Differential Geometry. *Journal of Mathematical Physics*, 4:735–445, June 1963.

[58] M. Ishii, M. Shibata, and Y. Mino. Black hole tidal problem in the Fermi normal coordinates. *Physical Review D*, 71(4):044017, February 2005.

[59] L. D. Landau and E. M. Lifshitz. *The classical theory of fields.* Pergamon Press, Oxford, 1975.

[60] J.-A. Marck. Solution to the Equations of Parallel Transport in Kerr Geometry; Tidal Tensor. *Royal Society of London Proceedings Series A*, 385:431–438, February 1983.

[61] C. Darwin. The Gravity Field of a Particle. *Royal Society of London Proceedings Series A*, 249:180–194, January 1959.

[62] C. Cutler, D. Kennefick, and E. Poisson. Gravitational radiation reaction for bound motion around a Schwarzschild black hole. *Physical Review D*, 50:3816–3835, September 1994.

[63] L. Barack, A. Ori, and N. Sago. Frequency-domain calculation of the self-force: The high-frequency problem and its resolution. *Physical Review D*, 78(8):084021, October 2008.

[64] S. Chandrasekhar. The Post-Newtonian Equations of Hydrodynamics in General Relativity. *ApJ*, 142:1488, November 1965.

[65] K. S. Thorne and J. B. Hartle. Laws of motion and precession for black holes and other bodies. *Physical Review D*, 31:1815–1837, April 1985.

[66] R. J. LeVeque. *Finite-Volume Methods for Hyperbolic Problems.* Cambridge University Press, Port Chester, NY, 2002.

[67] J. Blondin, J. Hawley, G. Lindahl, and E. Lufkin. Virginia Hydrodynamics 1 (VH-1), http://astro.physics.ncsu.edu/ blondin/research/John_Site/VH-1.html, 2012.

[68] P. Colella and P. R. Woodward. The Piecewise Parabolic Method (PPM) for Gas-Dynamical Simulations. *Journal of Computational Physics*, 54:174–201, September 1984.

[69] R. Courant and K. O. Friedrichs. *Supersonic flow and shock waves.* Interscience, New York, 1948.

[70] G. A. Sod. A survey of several finite difference methods for systems of nonlinear hyperbolic conservation laws. *Journal of Computational Physics*, 27:1–31, April 1978.

[71] C. Laney. *Computational Gasdynamics.* Cambridge University Press, New York, 1998.

[72] P. Woodward and P. Colella. The numerical simulation of two-dimensional fluid flow with strong shocks. *Journal of Computational Physics*, 54:115–173, April 1984.

[73] J. Stone. Athena3D, http://www.astro.virginia.edu/VITA/ATHENA/dmr.html, 2012.

[74] A. E. Broderick and Y. Rathore. A multidimensional, adiabatic hydrodynamics code for studying tidal excitation. *MNRAS*, 372:923–932, October 2006.

[75] M. Frigo and S. G. Johnson. Fastest Fourier Transform in the West (FFTW), http://www.fftw.org/, 2012.

[76] J P Boyd. *Chebyshev and Fourier Spectral Methods.* Dover Publications, Inc., Mineola, New York, 2001.